SANDIA REPORT
SAND2000-3008
Unlimited Release
Printed December 2000

Physical Models for Predicting the Effect of Atmospheric Corrosion on Microelectronic Reliability

Neil Robert Sorenson, Jeffrey W. Braithwaite, Samuel J. Lucero, Joseph R. Michael, James N. Sweet, David W. Peterson, David G. Robinson, Kenneth L. Erickson, and Corbett C. Battaile

Prepared by
Sandia National Laboratories
Albuquerque, New Mexico 87185 and Livermore, California 94550

Sandia is a multiprogram laboratory operated by Sandia Corporation, a Lockheed Martin Company, for the United States Department of Energy under Contract DE-AC04-94AL85000.

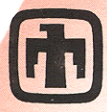

Sandia National Laboratories

Issued by Sandia National Laboratories, operated for the United States Department of Energy by Sandia Corporation.

Available to DOE and DOE contractors from
U.S. Department of Energy
Office of Scientific and Technical Information
P.O. Box 62
Oak Ridge, TN 37831

Telephone: (865)576-8401
Facsimile: (865)576-5728
E-Mail: reports@adonis.osti.gov
Online ordering: http://www.doe.gov/bridge

Available to the public from
U.S. Department of Commerce
National Technical Information Service
5285 Port Royal Rd
Springfield, VA 22161

Telephone: (800)553-6847
Facsimile: (703)605-6900
E-Mail: orders@ntis.fedworld.gov
Online order: http://www.ntis.gov/ordering.htm

SAND2000-3008
Unlimited Release
Printed December 2000

Physical Models for Predicting the Effect of Atmospheric Corrosion on Microelectronic Reliability

N. Robert Sorensen, Jeffrey W. Braithwaite and Samuel J. Lucero
Corrosion Science & Technology Department

Joseph R. Michael
Materials Characterization Department

James N. Sweet
BEOL Advanced Packaging Department

David W. Peterson
Integrated Microsystems Department

David G. Robinson
Risk & Reliability Analysis Department

Kenneth L. Erickson
Thermal/Fluid Experimental Sciences Department

Corbett C. Battaile
Materials & Process Modeling Department

Sandia National Laboratories
P.O. Box 5800
Albuquerque, NM 87185-0888

(Abstract follows on next page)

Abstract

Atmospheric corrosion is a stockpile age-related degradation mode that has a high likelihood of occurrence and the potential for significant consequence. As such, our science-based stockpile stewardship mission requires that we develop and use an analytical capability to predict any effect corrosion can have on weapon reliability. Presently, the stockpile contains numerous microelectronic devices contained in ceramic hermetic packages (CHP). However, the unavailability of CHP devices is already driving the insertion of plastic-encapsulated microelectronic (PEM) devices into stockpile electrical components. A significant concern with the use of PEM devices is the uncharacterized effect corrosion can have on device reliability during the long-term dormant storage conditions associated with our systems. Effective assessments of microelectronic corrosion damage must be based on a physical understanding of the moisture-related phenomena relevant to metallization failure. The main objective of this project was to provide this needed foundation specifically for the corrosion of aluminum, the prime vulnerability. A phased approach was followed throughout this project that has culminated in a predictive toolset that includes a constitutive model for the controlling corrosion processes combined with advanced computational techniques that allow process and environmental uncertainties to be explicitly addressed.

Although the complexity of the corrosion process (e.g., influence of intermetallic compounds) that was identified during this work inhibited some of our desired advancements, the final product clearly has satisfied the basic intent of this work. We have completed a preliminary quantitative assessment of the validity of the PEM storage concern, performed analyses of several field-related occurrences, and demonstrated the effectiveness of using computational reliability to model materials-degradation processes within the context of system-level performance.

1.0 INTRODUCTION

1.1 Background

Atmospheric corrosion is a leading age-related materials degradation mode that is observed in many high-consequence military and industrial systems. Although one of the system design criteria is to ensure that all materials are compatible with the expected environment, corrosion typically still occurs because the local environment is not or does not remain as expected (e.g., results from a bad seal, internal material outgassing) or intended designs/configurations are not properly manufactured (e.g., wrong material, contamination). The traditional approach has been to assess the severity and potential consequences of corrosion problems that arise and then, if needed, change materials or the environment. The basis for the assessment is normally engineering judgment that utilizes historical evidence, failure analyses, accelerated aging, and sometimes limited empirical correlations. Our high standards for surety now require the development and use of sophisticated analytical toolsets that can predict the effect of corrosion on system performance and reliability.

Although corrosion of structural and mechanical components occurs, it is the corrosion of electronic components that is the primary concern because of the direct consequence to function and therefore reliability. In general, the electronic features that

are susceptible to corrosion degradation contain copper and silver (sulfidation) or aluminum (localized pitting). Of particular interest is corrosion-induced failure of microelectronic devices. In the past, mil-spec microelectronic devices were available in hermetically sealed ceramic packages. However, the adoption of the Perry Initiative by the DoD requires that commercial off-the-shelf (COTS) hardware be used when possible, including microelectronics that are encapsulated with plastic molding materials. The widespread adoption of these plastic encapsulated microelectronics (PEM) in uniquely military applications is already eliminating the availability of the classical ceramic hermetic packages (CHP). As such, the insertion of PEM devices is now being considered for future DOE systems and upgrades. The plastic formulations used in PEMs have a finite permeability to moisture and cracks are often present between the plastic and metal feed-through features. As such, the devices, with micron and sub-micron sized metallization features, have a related susceptibility to environmental degradation.

Over the past 20 years, the microelectronics industry has expended considerable effort to assess and improve the reliability of devices that are being routinely used (*operational reliability*). In these assessments, a number of accelerated aging techniques have been developed and employed in conjunction with simple empirical statistical analyses.[1] The result is a relatively effective screening procedure for production lot acceptability. Stress factors include humidity, temperature, and importantly the application of a periodic bias voltage. To demonstrate the simplicity of this approach, the generally accepted form of the empirical equation used to relate the acceleration factor (AF) to environmental factors is the following:

$$AF = \exp\left[\frac{E_a}{k_b}\left|\frac{1}{T_o} - \frac{1}{T}\right|\right]\left(\frac{RH}{RH_o}\right)^n\left(\frac{a + bV}{a + bV_o}\right) \quad (1)$$

where T = temperature, RH = relative humidity, V= voltage, and E_a, n, a, and b are experimentally determined constants. Post-test analysis of aged devices has often been limited to simply confirming a failure, not determining root cause. As such, the ability to correlate the results with true service life (and actual environmental conditions) or to identify actual failure mechanisms has not been developed to any significant extent. A number of studies have been completed that suggest the operational reliability of PEM devices may not be an issue (PEM operational reliability approaches that for hermetic packaged devices in many environments and actually exceed hermetic devices in some special environments, such as high shock).[2]

Because most consumer and industrial electronic devices are continuously or at least periodically electrically active, industrial motivation to assess reliability under the long-term dormant storage conditions typically associated with military systems has not existed. As such, the extent and impact of corrosion during these periods is virtually unknown. Besides dormancy (extended time periods of electrical inactivity - sustained bias voltage), a dynamic and changing chemical and thermal environment often exists. For the case of corrosion, bias voltage is important because the intrinsic ohmic heating that occurs during operation usually dries the device, but also can cause enhanced electrolytic dissolution. Given these factors, the statistical information and type of

empirical treatment associated with the operational phase are not applicable. In particular, the elimination of any ohmic heating raises serious concerns about the effect of corrosion (moisture-induced degradation of metallization) on the *storage* reliability of PEM devices used in military hardware. Historically during accelerated aging, two types of moisture-related phenomena have been observed: Au wire/Al bondpad interfacial degradation and distributed Al track corrosion. The track corrosion is believed to be related to moisture penetration through defects in the protective SiN passivation layer and the presence of contamination. Importantly, modern best commercial practice (BCP) has effectively eliminated track corrosion as a significant failure mechanism. Bondpads have no passivation treatment and are susceptible to intermetallic voiding and accelerated attack due to moisture-related galvanic effects.

1.2 Objectives

To properly assess the effect of corrosion on electrical devices during long-term dormant storage, a set of mathematical models must be developed and validated that (a) have a physical / phenomenological basis, (b) treat a variable and changing environment, (c) account for the stochastic nature of corrosion, and (d) integrate seamlessly with age-aware electrical models of component performance. These comprehensive developments represent a formidable undertaking that is currently being pursued as an integrated program at Sandia (Sandia Corrosion Initiative). The work that is described in this report represents a portion of this program in which a solid foundation for evaluating the corrosion of microelectronics has been provided. Two specific objectives were established: (1) formulate a physical-based model that describes moisture-related metallization failure phenomena in PEM devices with a focus on corrosion of aluminum bondpads, and (2) demonstrate that computational reliability represents an efficient, globally applicable framework for developing the required materials-degradation analytical capabilities.

1.3 Approach

Because of the inherent complexity of the PEM corrosion process, this study adopted a phased “inside-out” approach. The initial phase involved understanding and formulating a mathematical description of the intrinsic degradation kinetics associated with bondpad corrosion (potentially involving initiation and propagation). This activity involved answering the question: “what are the corrosion mechanisms that occur without any plastic encapsulant present and what phenomenological-level processes need to be mathematically described?” The goal was to identify physical degradation mechanisms using controlled experimentation and then formulate corresponding deterministic mathematical expressions. Several types of parameters must be accounted for including, some that are physical (e.g., Au/Al interface and crevice geometry, intermetallic phase distribution) and some that are environmental (temperature, humidity, contamination, P_{O2}). The work constituted exposing unencapsulated Sandia-developed microelectronic test devices with various wire and bondpad configurations to slightly accelerated atmospheric corrosion conditions under strictly controlled humidity, temperature and atmospheric contaminant conditions. In addition, various levels of possible solid

contaminants were applied to the exposed surface of the die. Resultant degradation was characterized as a function of time by resistance measurement and by physical and chemical changes at the bondpad surface (measured with a combination of optical and electron microscopy).

In the second phase, the intrinsic bondpad corrosion model was to be enhanced by including the transport of environmental parameters associated with the molded plastic layer – be able to calculate how the presence of the plastic modifies the local bondpad environment (e.g., local temperature and humidity). This work included mathematical analyses and selected experimental aging studies using both encapsulated Sandia test devices as well as selected commercial PEMs. In the third and final phase, to permit uncertainty to be addressed, the comprehensive bondpad degradation model was merged into Sandia's new computational reliability framework. Using projected storage environments, the resultant code was exercised to assess the potential impact of prolonged dormant storage on PEM reliability. The resulting information provided the first quantitative measure of the validity of the PEM storage reliability concern. The organization of this report generally follows the selected approach: mechanistic understanding, corrosion model development (deterministic model, integrated model), and specific device and system-level modeling simulations.

2.0 Characterization of Bondpad Corrosion

A wide range of experiments were performed during this study to properly characterize three important aspects of bondpad corrosion: reaction kinetics, general behavior, and mechanisms. Our findings are divided into three corresponding subsections that follow. The kinetics section presents results describing the effect of environmental and physical variables on the rate of bondpad degradation. The corrosion behavior section focuses on the physical aspects of bondpad corrosion that were determined using advanced surface-analytical techniques. This information provides a picture of the corrosion process, suggesting where and why the attack occurs. The mechanisms section summarizes our conclusions relative to the phenomenology of bondpad corrosion. For reference, Appendix A contains more detailed information relative to the experiments that were performed on a four specific topics: (A1) configuration of experimental matrix, (A2) environmental exposure system and data acquisition, (A3) corrosion-test device, and (A4) several new analytical techniques that were developed and used.

2.1 Corrosion Kinetics

To follow the corrosion process and measure reaction kinetics, new measurement techniques were required. Visual observation provides qualitative data only, and is thus not useable in quantifying reaction rates. As described in Appendix A3, a corrosion-test chip, developed at Sandia and termed ATC 2.6, allowed measurement of bondpad corrosion. Two resistance values are obtained from the ATC device; wirebond resistance and sheet resistance. The wirebond resistance represents the true resistance that is seen by the electronic circuitry on the die, but it is not a sensitive measure of corrosion. In addition to the bondpad resistance, it includes the bondwire resistance. As listed in

Appendix A1, a wide range of experiments were performed with the prime parameters being assessed including T, RH, contaminant (gas and solid), amount of intermetallic, and presence of encapsulant. Because atmospheric corrosion in microelectronic devices normally requires significant exposure times, all of our experiments were performed under highly accelerated conditions relative to contamination levels (e.g. ppb to ppm levels).

Figure 2-1 shows resistance curves for an ATC 2.6 device exposed to moist, chlorine containing air. The plot shown in (a) is for the wirebond, and includes the wire resistance, while the plot shown in (b) is for the bondpad sheet resistance. The wirebond resistance is much higher than the sheet resistance. In addition, there is essentially no change in resistance with exposure time until complete wirebond failure is observed (open circuit). In contrast, the sheet resistance exhibits a continuous increase during exposure, making it much more suitable for monitoring corrosion. A correlation between the two resistance measurements probably exists, but our device structure and measurement technique are not adequately sensitive to permit the relationship to be identified.

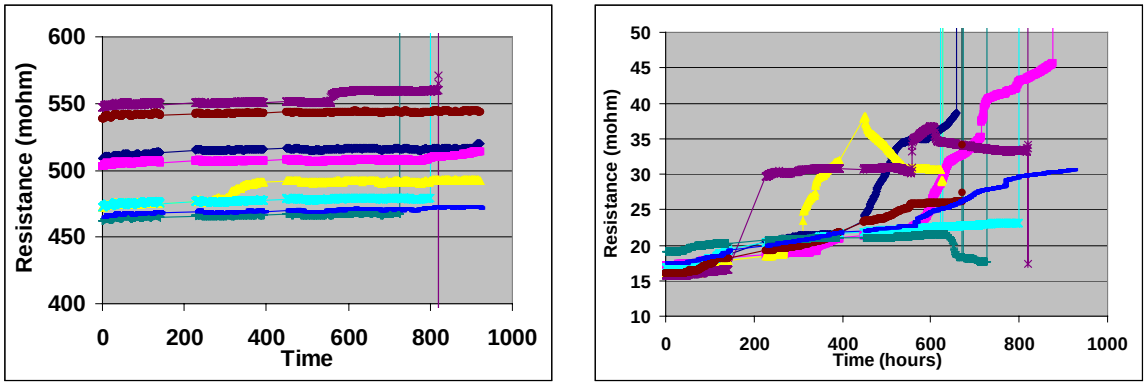

(a) (b)

Figure 2-1. Plots of wirebond resistance (a) and bondpad sheet resistance (b) for an ATC 2.6 device exposed to chlorine containing moist air. Note the lack of response of the wirebond resistance to corrosion.

Because the sheet resistance is a function of the amount of intermetallic present in the wirebond, a direct comparison between tests was difficult. Changing the heat treatment conditions changed the amount of intermetallic, and thus, the bondpad resistance. Additionally, even under identical heat-treat conditions, considerable variability was seen in the quantity of intermetallic present. Thus, to normalize the data and allow valid comparisons, the raw resistance data were converted to resistance change values by dividing the resistance, R, by the initial resistance, R_o.

To measure the kinetics of bondpad corrosion, the sheet resistance of the ATC was monitored. Figure A7 (in Appendix A3) shows the electrical structure used to monitor sheet resistance. As the Al of the bondpad corrodes, the sheet resistance increases. The change in resistance ($\Delta R/R_o$) is then calculated ($\Delta R/R_o$ provides a more accurate metric

of bondpad corrosion than the actual resistance, and allows normalization of the data for comparison between experiments). A typical plot of $\Delta R/R_o$ *vs*. Time for one ATC device is shown in Figure 2-2. All of the bondpads behave similarly, with some scatter in the data. The resistance curves contain three general characteristics:

1. Areas of continuous increase in resistance
2. Steps that indicate very rapid increases in resistance
3. A final large stepped increase in resistance that correlates with wirebond failure due to open circuit.

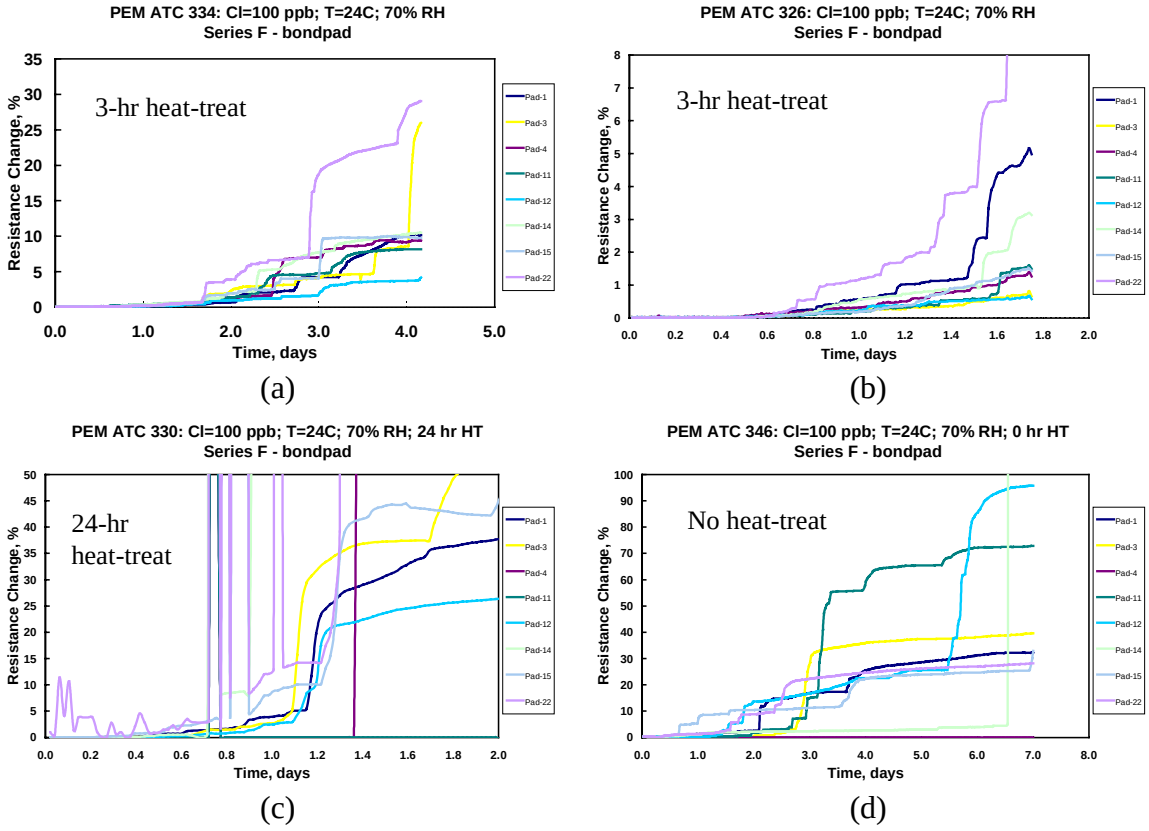

Figure 2-2 The effect of heat-treatment time on the bondpad resistance rise: (a) and (b) are results from the baseline exposure condition (100 ppb [Cl_2], 70% RH, 24°C, and 3 hour heat treatment at 175°C) and are replicates indicating experimental reproducibility; (c) is for an over heat treated conditions (24 hr at 175°C and (d) is for no heat treatment.

Plastic packaged microelectronics are typically cured at an elevated temperature that results in the formation of Au/Al intermetallic compounds in the wirebond. To simulate that process, ATC devices were heated treated for various times at 175°C, resulting in the formation of Au/Al intermetallic compounds at the interface. Figure 2-2 shows the effect of heat treatment on the corrosion process. The plots in (a) and (b) are from baseline exposure conditions for samples receiving the standard 3-hour heat treatment. They are duplicate samples and provide information relative to the

reproducibility of the exposure experiments. The agreement is quite good between the two samples. Both show the scatter typical of the ATC devices. The plot in (c) is from a sample heat treated for 24 hours (representing an over-aged sample). The plot in (d) is from a device receiving no heat treatment. In this device, the only intermetallic present is that which formed during the thermisonic bonding process. A comparison of (a) and (c) shows that the overaged sample is considerably more prone to corrosion. After 2 days of exposure, half of the wirebonds had failed. The remainder of the bondpads exhibited resistance increase values of 30-40%. In comparison, the sample in (a) exhibited less than 5% increase in resistance for all eight wirebonds. The un-heat treated sample also exhibited increased susceptibility relative to the 3-hr. sample. A comparison of (a) and (d) shows that the un-aged sample exhibits a resistance increase of 20-30% after 4 days, while the baseline sample increased only 5-10% in the same time period.

The effects of chlorine concentration and relative humidity on wirebond corrosion are shown in Figure 2-3. The plots in (a) and (b) represent lower chlorine concentrations relative to the baseline conditions of Figure 2-2 (a) and (b). It is clear from these plots that decreasing the chlorine concentration results in a lower corrosion rate. Decreasing the $[Cl_2]$ to 50 ppb (Figure 2-3(a) resulted in a resistance increase of about 1% after 4 days while exposure to 100 ppb caused an increase of 5-10% in the same time period. And, as shown in Figure 2-3(b), decreasing the $[Cl_2]$ to 10 ppb resulted in less than 1% change in resistance after 10 days of exposure.

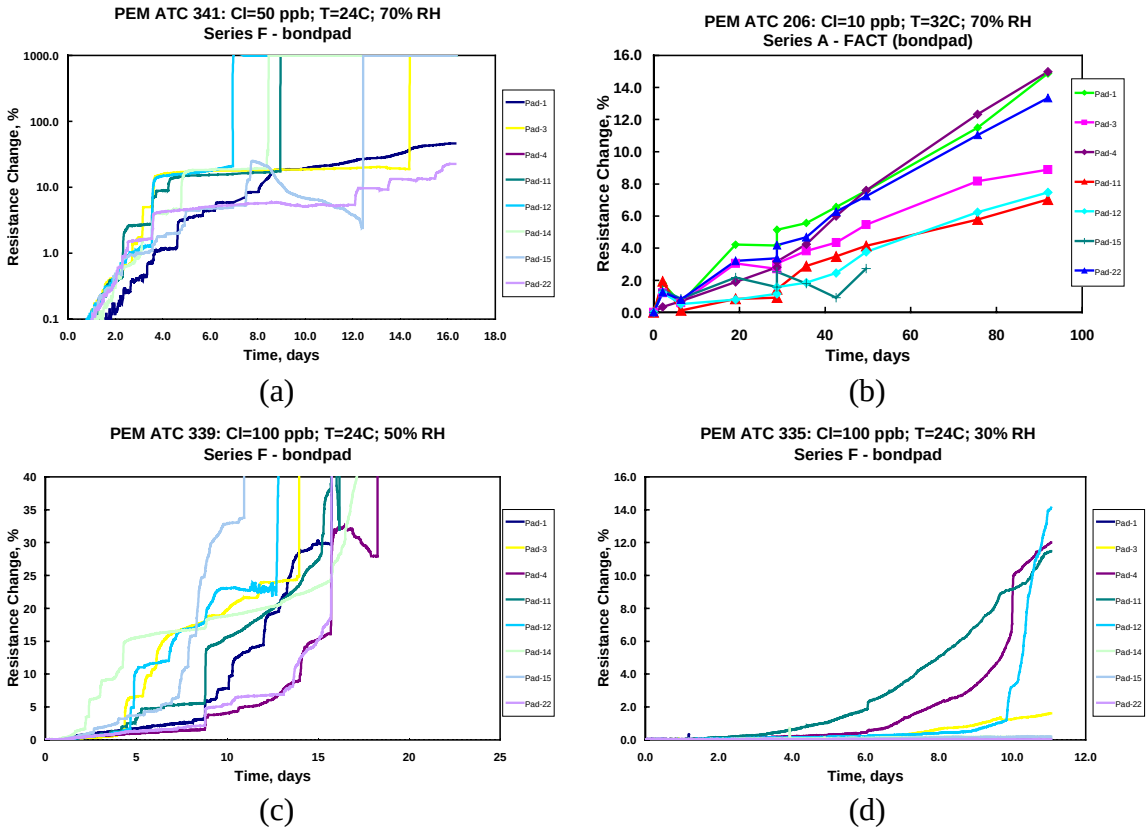

Figure 2-3. The effect of chlorine concentration and relative humidity on the bondpad resistance rise that should be compared with the results from the baseline conditions shown in Figure 2-2a-b: (a) and (b) lower [Cl_2]; (c) and (d) lower relative humidity levels.

The effect of humidity on the corrosion rate can be seen by comparing the plots in Figure 2-3(c) and (d) with those from the baseline exposure (Figure 2-2(a), (b)). Decreasing the humidity from 70% to 50% RH resulted in a resistance change of roughly 10% after 10 days compared with 10% change after 4 days at 70% RH. As shown in Figure 2-3(d), exposure to 30% RH causes a 5% change in resistance after 10 days of exposure. From these data, it is clear that decreasing the humidity decreases the corrosion rate.

The effect of other contaminant gasses on bondpad corrosion is shown in Figure 2-4. Two additional gasses were tested, bromine and chlorotoluene. The bromine was used to simulate contaminant species possible from the manufacturing processes, and chlorotoluene represents an organic halide the may be present as a true atmospheric contaminant. Bromine appears to behave similarly to chlorine during atmospheric corrosion of wirebonds. The shape of the curves for the gasses is similar. However the corrosion rate for devices exposed to Br_2 is significantly higher. At identical halogen levels, Br_2 exposure results in a 10% resistance increase after only half a day, while the

Cl_2 exposure required 10 days to reach the same resistance level. Even when the Br_2 concentration was reduced to 3 ppb (<10% of the Cl_2 level), the corrosion rate is higher for bromine exposure (compare Figure 2-4, a and c). Thus, as a pollutant, bromine is considerably more active in promoting corrosion than chlorine. These results are consistent with thermodynamic calculations that show that Br dissolves more readily in water than does chlorine, and results in a higher concentration in solution. Finally, Figure 2-4(d) shows the results of exposure to chlorotoluene. It is clear that this species does not provide a source of free Cl^-, as no resistance change was observed, even after 25 days of exposure.

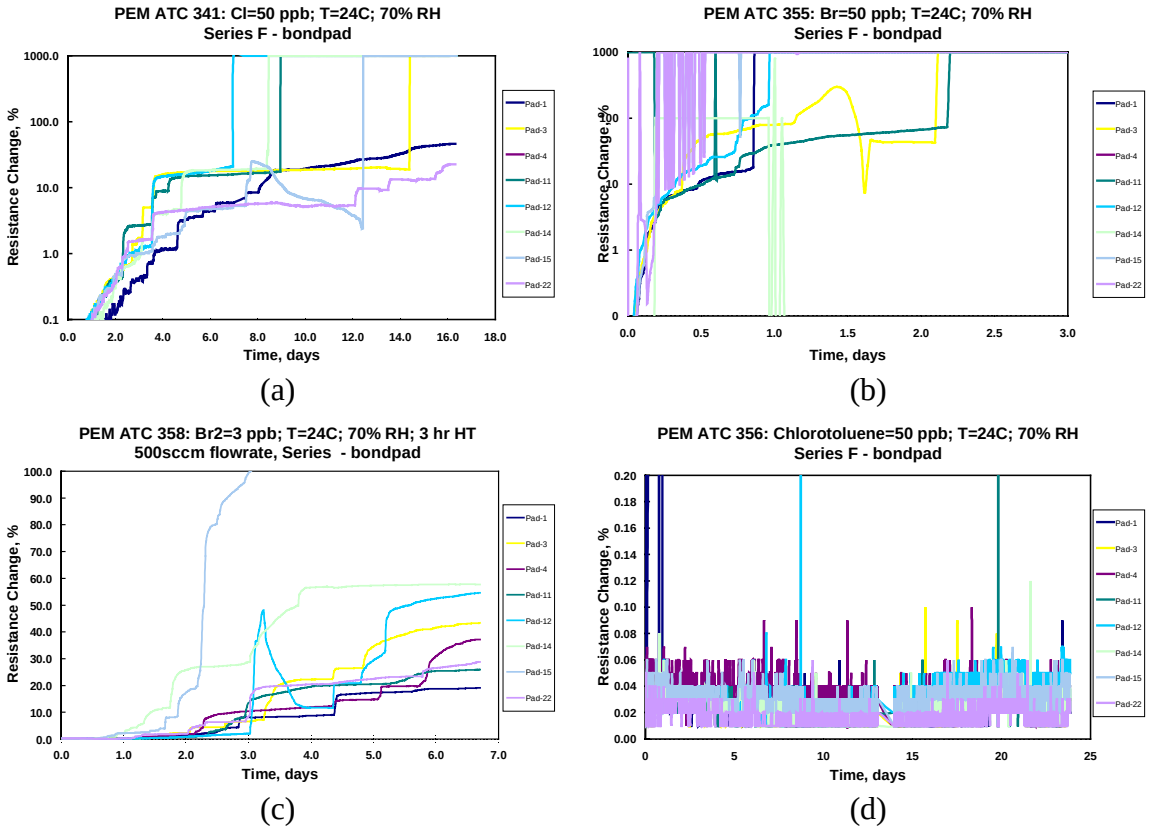

Figure 2-4. The effect of other contaminant gases on the bondpad resistance rise: (a) chlorine, (b) bromine at same level as (a), (c) bromine at lower level, and (d) chlorotoluene.

The effect of the presence of a plastic encapsulant on bondpad corrosion is shown in Figure 2-5. The plastic encapsulant is not a moisture barrier (the permeability of plastic to moisture is well documented), so it must be assumed that the plastic acts as a barrier to the chlorine gas, preventing access to the die surface. As can be seen from the figure, no change in resistance was observed for these devices, demonstrating the lack of corrosion. This does not preclude corrosion of real PEM devices that may be contaminated prior to plastic encapsulation, or have molding defects (cracks, delaminations), but it does suggest that the migration of contaminants through plastic is not an issue.

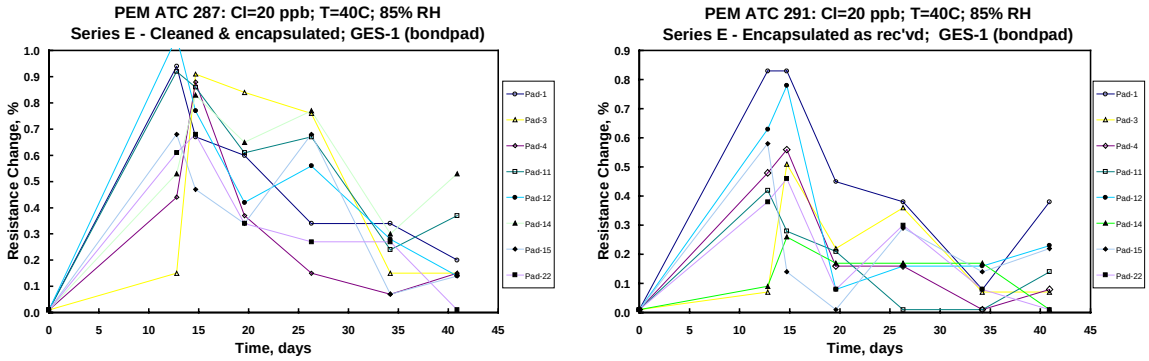

(a) (b)

Figure 2-5. The effect of the presence of a plastic encapsulant material in the well of the ATC corrosion test device on the bondpad resistance rise: (a) surface plasma cleaning prior to encapsulation, and (b) surface encapsulated as the test device was received.

The most likely source of chloride on the wirebond surface is from contamination during the fabrication process. It is well known that dust particles containing contaminants such as chlorides can settle on the surface and induce corrosion.[3] In addition, other sources of contamination (spittle, cleaning residues, etc.) tend to leave solid deposits on the surface. To study the effect of solid contaminants on bondpad corrosion, two solid contamination processes were used. In the first process, devices were contaminated by airbrushing the surface with an alcohol solution containing dissolved NaCl. In the second process, samples were contaminated by depositing synthetic dust on the die surface. Both types of samples were then exposed to elevated levels of humidity. Typical results from these tests are shown in Figure 2-6. For the NaCl contaminated samples, there is an initial rapid rise in resistance, followed by a period where no change is seen. This indicates that the solid contaminant is available initially, but becomes depleted with time. For the samples contaminated with the synthetic dust (c-d), the shape of the resistance curve more closely resembles gas-phase contamination curves, but the gradual increase in resistance is much less evident. Interestingly, a significant effect of humidity was found. As shown in (c), essentially no corrosion was observed at 50% RH. This level appears to be below the critical humidity for the dust-covered surface. Increasing the humidity to 70% RH (d), allows the initiation of bondpad corrosion. It is interesting to note that the quantity of dust on the surface had little effect on corrosion rate. Samples contaminated with a light dusting of particles corroded at the same rate as those receiving a heavy dusting. This indicates that the particle density was sufficient in both instances to initiate corrosion, requiring only the critical humidity for the bondpad to corrode.

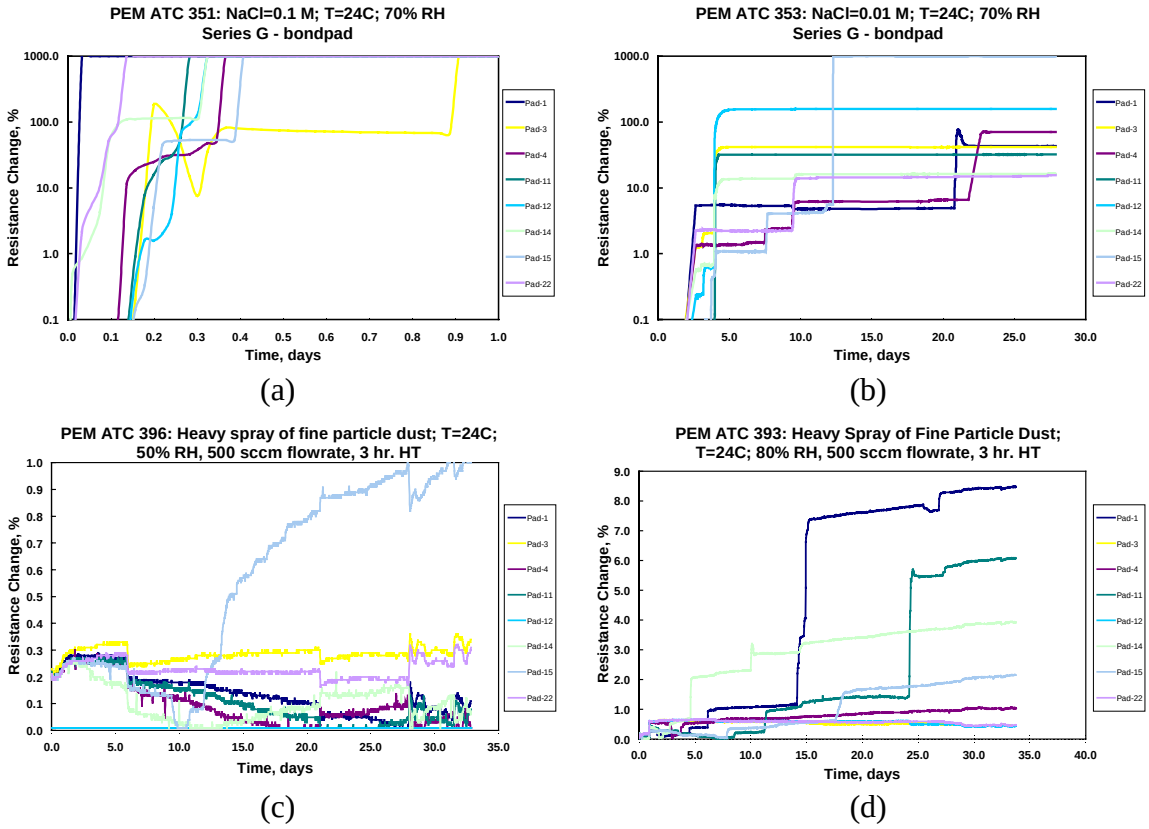

Figure 2-6. The effect of the presence of two levels of solid NaCl contaminant on the bondpad resistance rise. Sample depicted in (a) and (b) were contaminated by air-brushing the surface with an ethanol/NaCl solution. Samples shown in (c) and (d) were contaminated with synthetic dust containing NaCl.

There is good correlation between the resistance plots and the visible extent of corrosion. Figure 2-7 presents results for individual wirebonds on a single ATC. The resistance curves show the expected general characteristic for wirebond corrosion. There is significant variability in corrosion rates between individual wirebonds, which is manifest by scatter in the resistance plots. At the conclusion of the test, $\Delta R/R_o$ values ranged from 5% to 30%. Included in Figure 2-7 are SEM images taken following back-thinning (see Appendix A4 for more information on the sample preparation procedure). The intermetallic is visible as bright areas and the Al of the bondpads appears as the intermediate gray areas. The darker areas next to the Au and Au-Al intermetallic represent voids where corrosion has removed the Al. There is good correlation between the extent of corrosion (as observed in the SEM) and the measured resistance change. Clearly, the bondpad exhibiting a 30% change in resistance (a) suffered more extensive attack than either of the other two wirebonds presented (b or c). It is also interesting to note that the corrosion is concentrated around the edge of the gold ball, and that the Al is not generally attacked elsewhere.

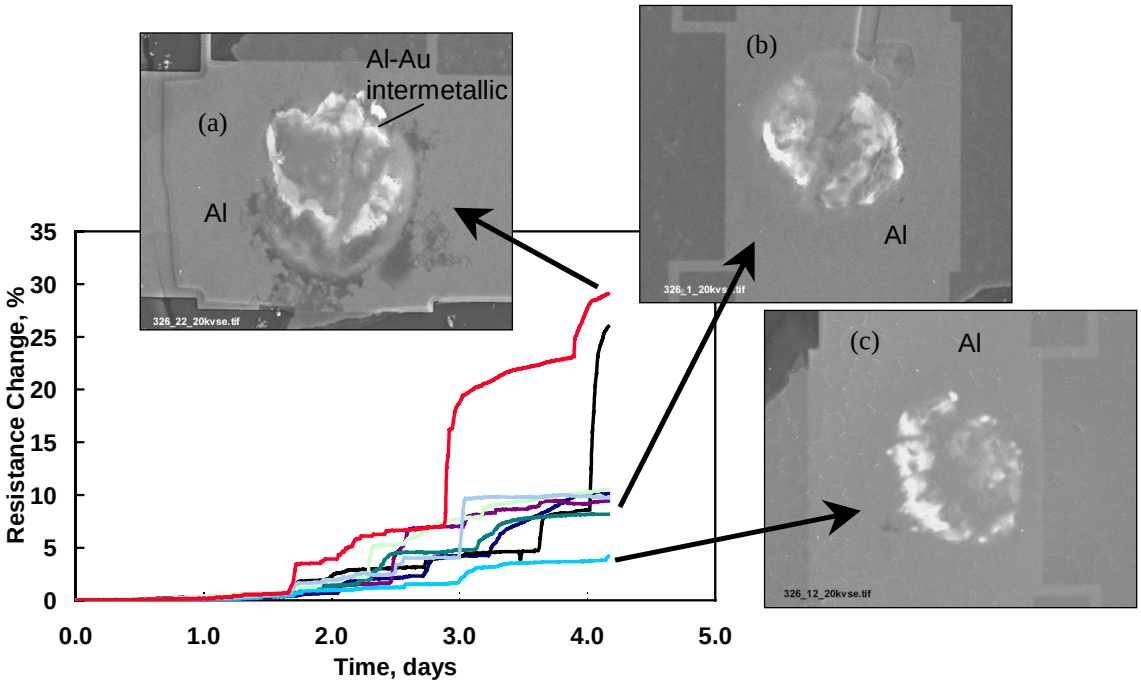

Figure 2-7. Resistance plot for ATC exposed to air containing chlorine and water vapor. The images inset are from back-thining process and show the extent of corrosion of the wirebond. Arrows associate curves with imaged bondpads

Similar results for a single wirebond are shown in Figure 2-8. During the test, the sample was removed from the exposure chamber and the bondpads were examined and photographed. It is clear that bondpad corrosion increases with increasing exposure time, with excellent correlation between the resistance data and the visual appearance of the bondpad. Consistent with other results, the corrosion initiates at the edge of the Au ball and propagates around the perimeter of the wirebond.

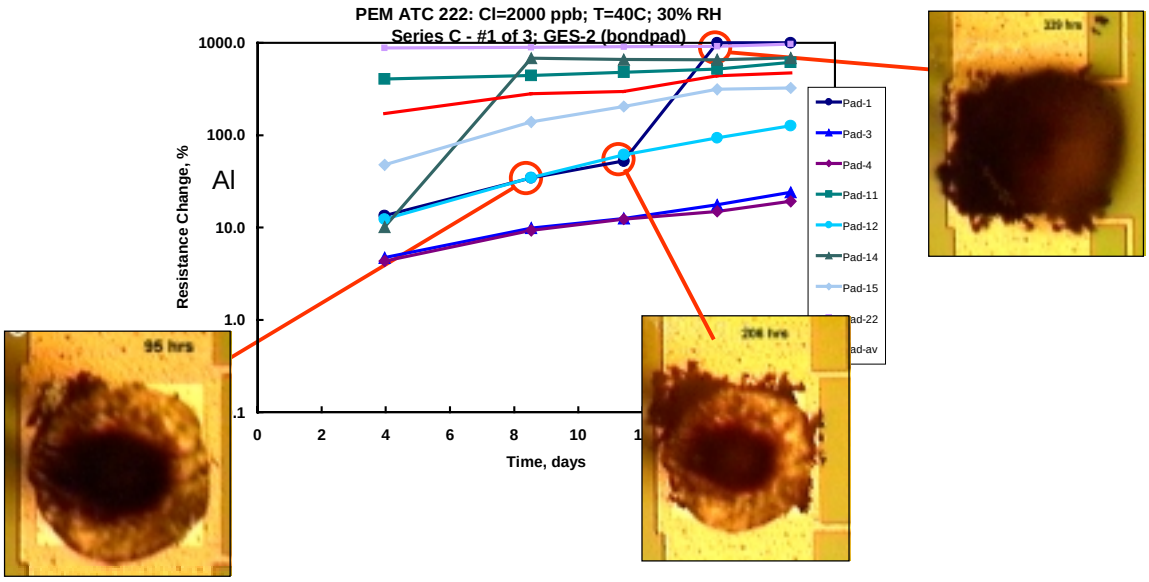

Figure 2-8. Resistance plot for ATC exposed to air containing chlorine and water vapor. The images inset are optical images and show the extent of corrosion of the bondpad.

2.2 Corrosion Behavior

Corrosion of Al bondpads has been seen on commercial products. Figure 2-9 shows an image of a corroded bondpad. The Al corrodes, producing corrosion products. It appears to initiate at the Au/Al interface, but can spread to the remainder of the Al bondpad. In order to understand and model this process, we must first be able to reproduce it in the laboratory under accelerated testing conditions.

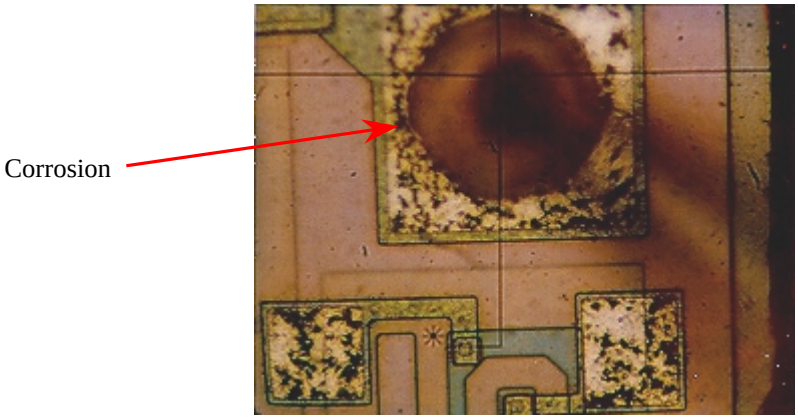

Figure 2-9 Image showing bondpad corrosion of commercial device.

2.2.1 General

Accelerated laboratory tests involving Au/Al wirebonds results in corrosion of the Al. The process requires the presence of a surface contaminant (e.g. chloride), elevated moisture levels, and is accelerated by the presence of the Au. In fact, as shown in Figure 2-10, the Au ball bond greatly facilitates or accelerates initiation of the corrosion process. The bondpad shown in (a) was heavily contaminated with NaCl. Large salt crystals can be seen on the surface. However, no corrosion of the Al pad is visible. In contrast, the image in (b) contains considerably less salt, but corrosion of the Al bondpad is clearly visible. In this case, the presence of the Au was required to initiate corrosion.

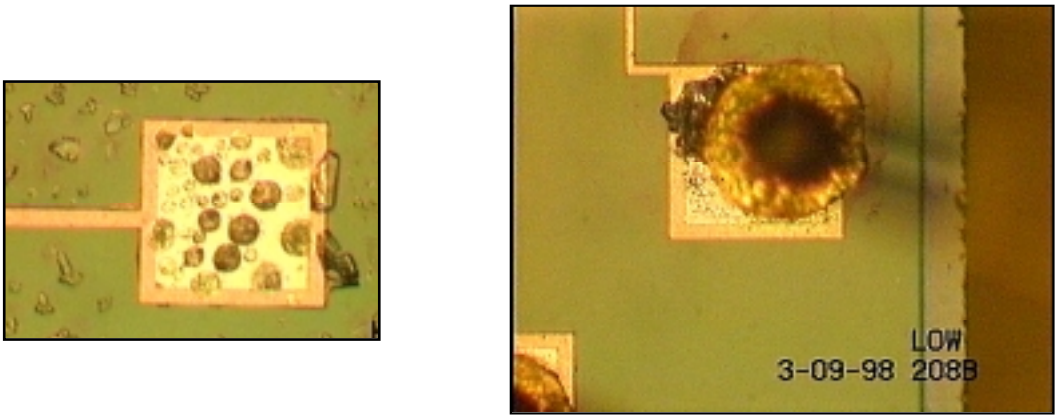

(a) (b)

Figure 2-10. Optical images of bondpads contaminated with NaCl and exposed to elevated humidity. Note the lack of corrosion in (a), due to the absence of a ball bond on the bondpad.

Figure 2-11 shows wirebond at various stages in the corrosion process. The SEM image in (a) is for a commercial device that failed in service. It was not part of the accelerated aging tests used in this program. Note that the Al bondpad has corroded to the extent that the Au ball bond is no longer in contact with the die surface. A similar image, for a device aged in our chamber is shown in (b). Again, corrosion resulted in complete failure of the wirebond with the Au ball no longer in contact with the Al on the die surface. The images in (c) and (d) show bondpads at earlier stages in the corrosion process. Attack of the Al can be seen to initiate near the Au ball and progress outward through the Al layer. There is also some indication that the corrosion continued under the passivation layer.

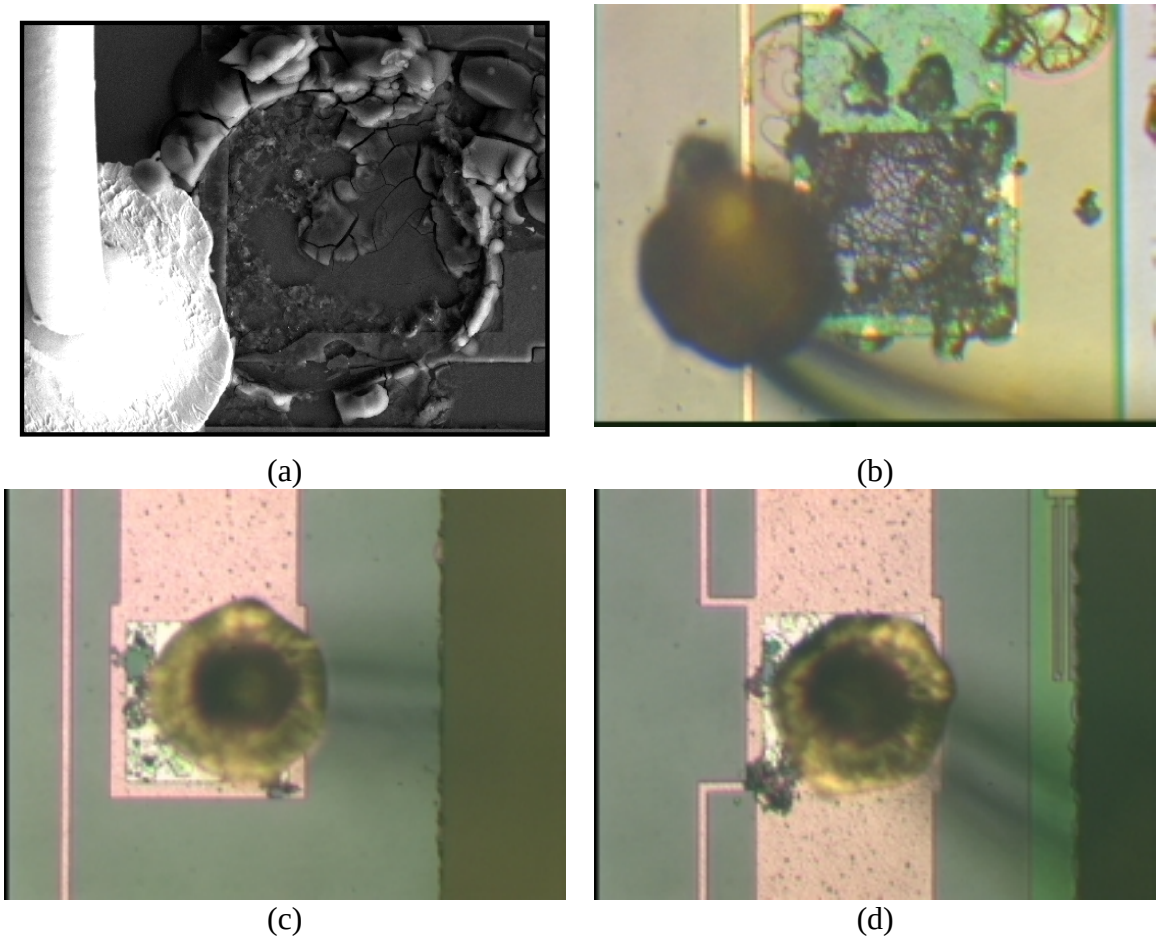

Figure 2-11. Micrographs of Au/Al wirebonds. Corrosion can be seen on the Al pads next to the Au ball bonds. When corrosion becomes extensive enough, the Au ball lifts off of the surface.

Figure 2-12 shows additional images from corroded ATC devices. It is clear that the presence of the Au ball on the bondpad accelerates the corrosion process. Although some attack can be seen on bare Al bondpads, they are relative free of corrosion. It is also clear that the rate of attack (extent of corrosion) varies from pad to pad. In some cases, the corrosion is extensive enough to cause delamination of the Au ball from the bondpad, leading to an open circuit condition.

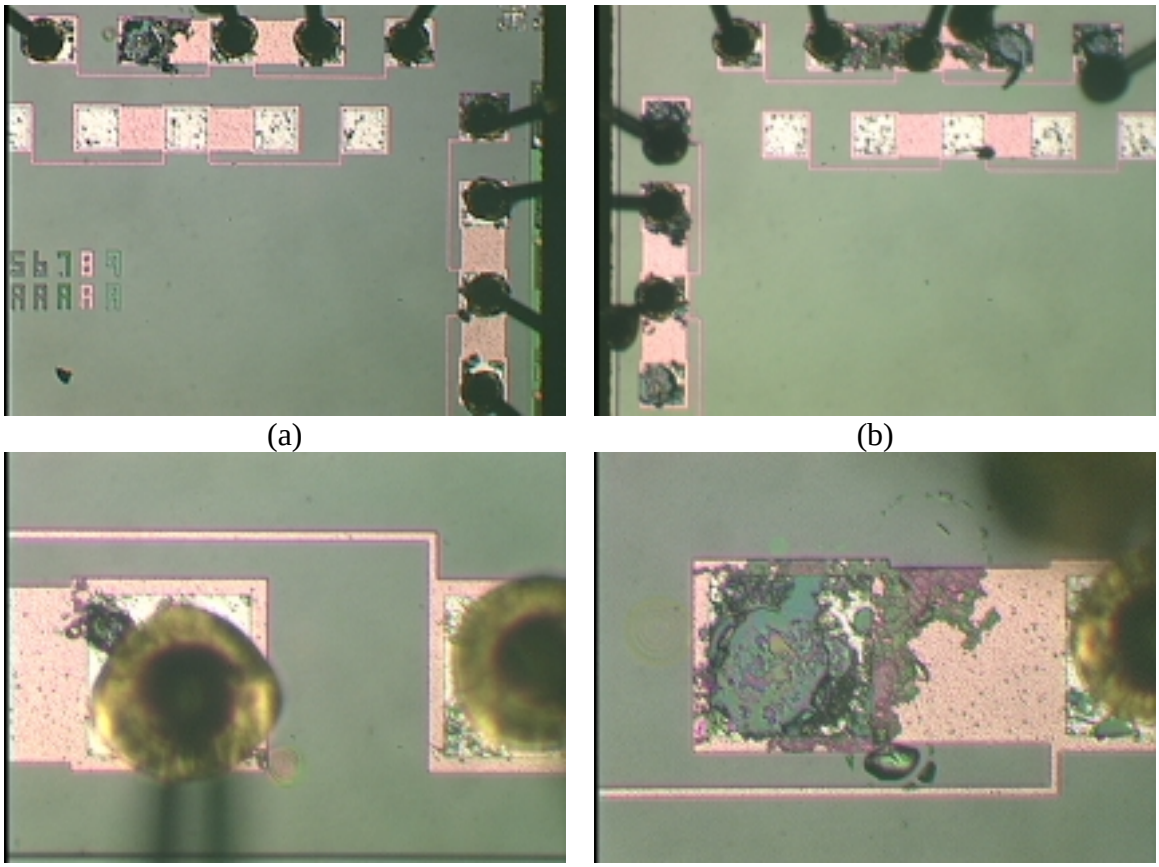

Figure 2-12. Optical micrographs of Au/Al wirebonds. Corrosion can be seen on the Al pads next to the Au ball bonds. When the corrosion becomes extensive enough, the Au ball lifts off of the die surface, creating an open circuit.

2.2.2 Corrosion Initiation

During wirebond corrosion, the Al below the Au ball is attacked. The Au ball itself obscures this area, making it impossible to observe the corrosion visually. In order to observe the corrosion process, two structures were built on either glass or quartz substrates. The first was a fairly simple structure, consisting of a series of Au spots on a thin film Al substrate (Figure 2-13(a)). Supporting the thin film is a glass slide. A photograph of the device is presented in Figure 2-13(b). Because the structure is on a glass slide, a light beam can be used to show perforation of the Al layer during the corrosion process. The sample was placed on a microscope stage and inundated with a dilute NaCl solution. The corrosion process was followed optically, by backlighting the sample. The field remained dark until corrosion of the Al resulted in perforation of the thin film. A series of images (c-e) show the evolution of corrosion with time. As corrosion proceeds, the number of perforations increases, as well as the size of individual perforations. It is important to note that the attack is confined to the region of the Au deposit, clearly illustrating the importance of galvanic coupling in the corrosion process. No perforations were seen in the Al away from the Au spot.

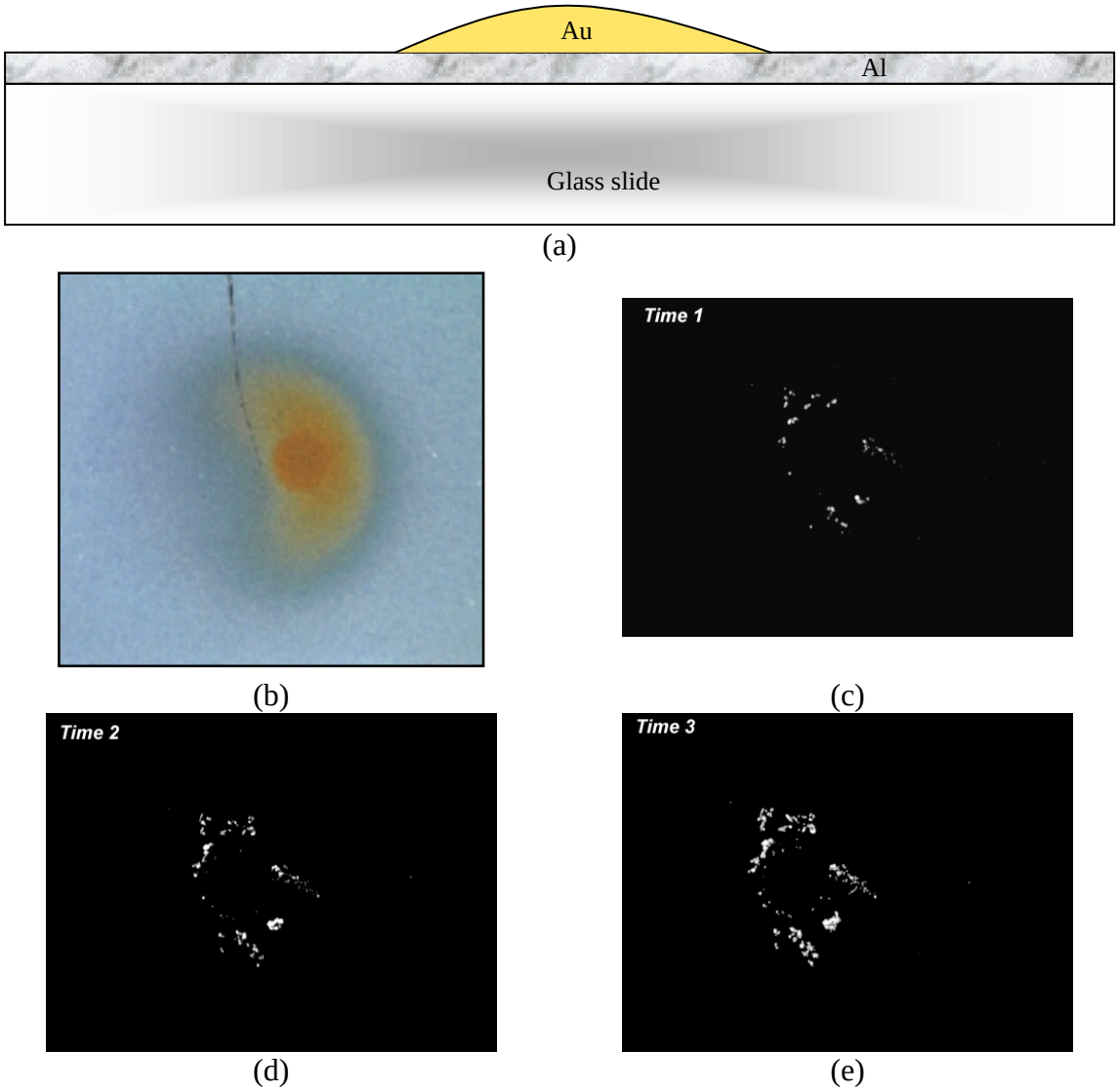

Figure 2-13. Deposited Au spot on Thin film Al on a glass slide. A schematic of the structure is shown in (a), with a photograph from the top (b), and a series of images during corrosion (c-e).

Image analysis techniques were applied to the images shown in Figure 2-13. The results of the image analysis are presented in Figure 2-14. Individual perforations in the Al thin film were counted and binned according to size (area). This distribution is shown in Figure 2-14(a). It is clear that the number of perforations increases with time, indicating that corrosion of the Al continues to initiate throughout the experiment. In addition, the size of the existing spots increases with time. Thus, corrosion of the thin film of Al can be characterized as a series of initiation events followed by consumption of the Al as the corrosion propagates. By summing the individual corrosion sites, an indication of corrosion rate can be determined Figure 2-14(b). As expected, the rate

increases with time as more sites become active. These experiments clearly show several important aspects of Al corrosion relative to Au/Al wirebonds:

1. Galvanic coupling to the Au is critical to the corrosion process. It causes the process to initiate at the Au/Al interface. It also accelerates both the initiation and propagation rates.
2. Not all sites are initiated simultaneously. New spots appear with exposure time, indicating additional initiation events.
3. Once initiated, the sites continue to corrode.

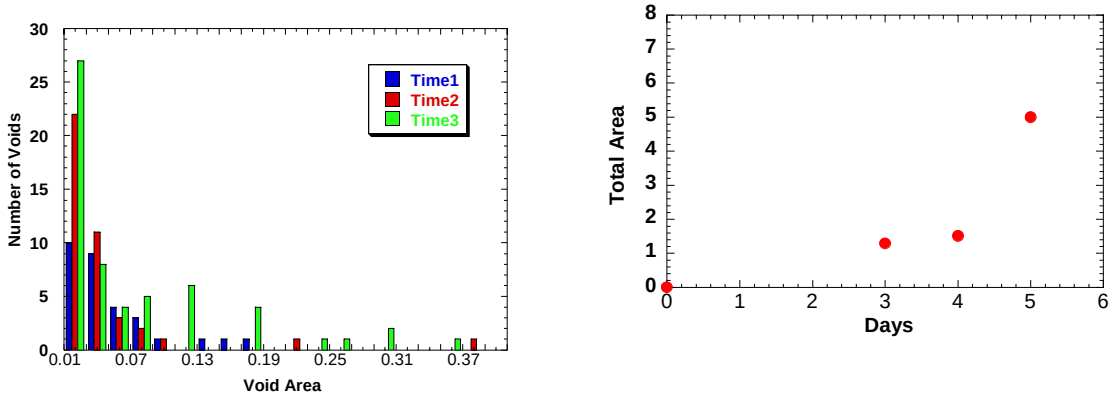

(a) (b)

Figure 2-14. Image analysis results from Al thin film corrosion experiment. The distribution of corrosion spots is shown in (a), with the cumulative amount of Al lost presented in (b).

The second structure built on an optically transparent substrate was essentially an ATC 2.6 structure on a quartz substrate. This structure is shown in Figure 2-15. It contains wirebonds and traces that mimic the features of the ATC chip. These devices were exposed to humidified air containing ppb levels of chlorine gas in our gas exposure system. At the conclusion of the test, the structures were examined optically by looking through the quartz at the Al bondpad.

Figure 2-16 shows images from the quartz device at the conclusion of the exposure. The Al pad can be seen with Al/Au intermetallic near the center of the pad. Corrosion of the Al has resulted in loss of metal. It appears that the corrosion process initiated at or near the interface, but certainly near the Au ball. There also appears to be an aspect of intergranular corrosion, with the corrosion following what may be grain boundaries in the Al. The results of this test are consistent with the glass slide experiment. Corrosion initiates at multiple locations with some distribution of induction times.

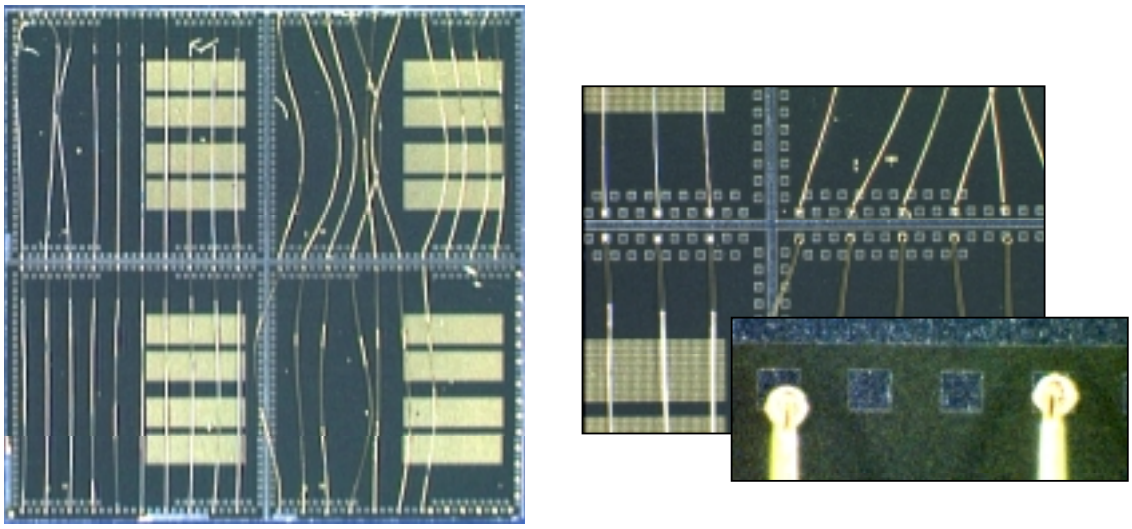

(a) (b)

Figure 2-15. Simulated wirebond structure on a quartz substrate. The device contains bondpads, traces, and other features found on the ATC.

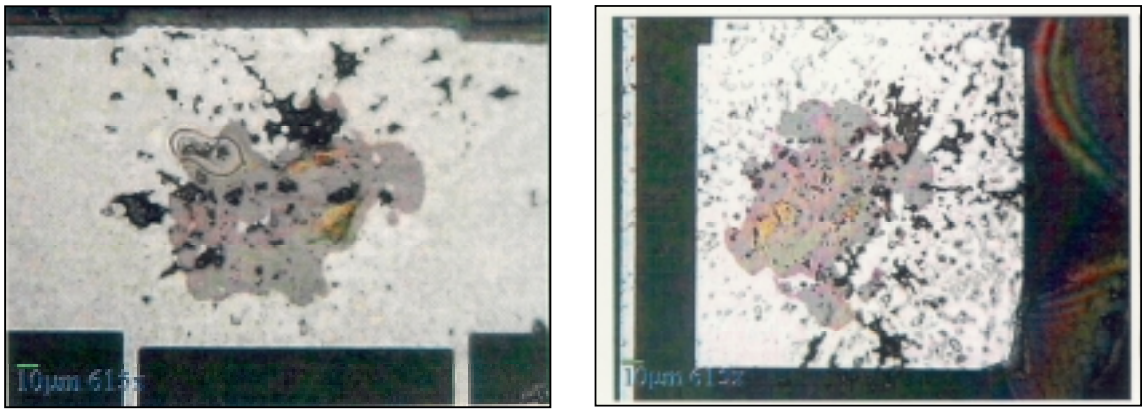

(a) (b)

Figure 2-16. Optical images of Al bondpad taken through the quartz substrate. Corrosion of the Al is visible around the Al/Au intermetallic.

2.2.3 Propagation

To improve our understanding of wirebond corrosion, it is interesting to examine virgin and corroded wirebonds in cross-section. Most studies of wire bonds have either prepared standard metallographic cross sections of the wire bonds or have pulled the bonds to failure and then inferred bond microstructure from the fracture surface. Both of these techniques suffer from severe disadvantages. It is very difficult to prepare metallographic cross sections of the wire bonds due to the small size and the rather soft pure metals used in the case of Au/Al bonds. The deformation that accompanies the pull test of the wire bond quite often either distorts or fully conceals the microstructural

features that existed in the undisturbed wire bond. Due to the initiation of corrosion directly under the wirebond it was necessary to employ novel techniques to directly observe the microstructural features of the wirebond and the results of corrosion. We have employed three techniques in this study: 1) a novel sample preparation technique was developed that exposed the underside of the Al bondpad, 2) the SEM was used to sample the microstructure of the bond as a function of depth and, 3) Focussed Ion Beam (FIB) milling of the exposed bondpads were used to directly image cross sections of selected bond pads. Detailed information on each of the specifics of these techniques are included in Appendix A4.

2.2.3.1 Microstructural Characterization of Au/Al Wirebonds

In the Au/Al binary system there are five intermetallic compounds that can form depending on the heat treatment temperature-time profile (Figure 2-17). The process of bonding a gold wire to an Al bond pad forms a diffusion couple between Au and Al. The intermetallic compounds that form can provide additional strength to the wire bond. In order to understand the corrosion of these Au/Al wire bonds it is important to fully characterize the microstructural features present in these bonds. Previous work has depended on the examination of fractured wire bonds. Some insight into the structure of the bonds could be gained from these examinations, but not a true picture of a wire bond. In this study we have examined wire bonds using an approach that permits the wire bond to be examined from the underside as was described in Appendix A4. Basically, we used a technique to remove the die from the back side, leaving the wirebond intact. This process allowed us to examine the wirebond from below, providing information about the structure of the bondpad. These samples were examined optically and with an SEM. In the SEM, the electron beam voltage could be varied. At low voltages, the electron beam penetrates to a very shallow depth, and the information obtained is confined to the surface of the sample. At higher voltages, the penetration depth increases, and the analysis is for a thicker layer. In this way, a sort of tomography can be achieved, providing depth information for the sample. Table 2-1 shows the relationship between beam voltage and penetration depth for Au and Al. The wire bonds were subjected to heat treatments of either 3 or 24 hours at 175°C.

Table 2-1 Calculated information depth for Au and Al as a function of electron beam voltage

	1kV	5kV	10kV	30kV
Au	0.002	0.0235	0.081	0.51
Al	0.008	0.12	0.4	2.5

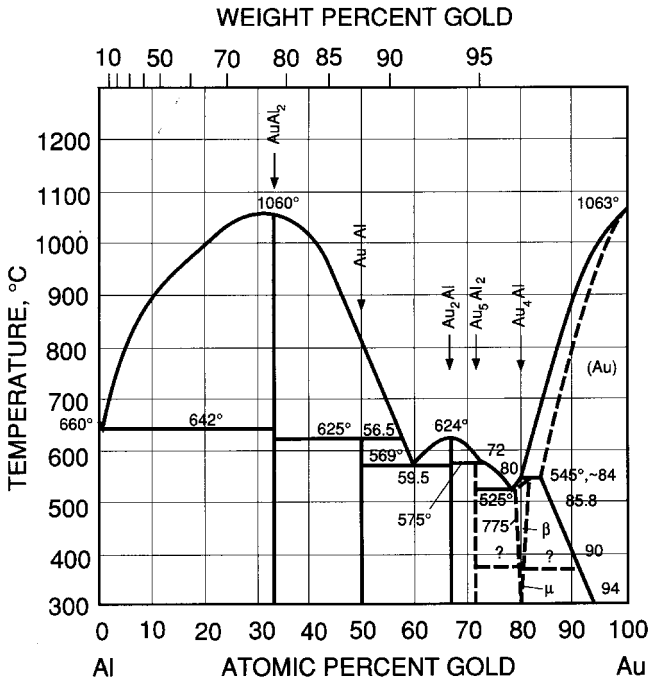

Figure 2-17. Phase diagram for the Al-Au system

Figure 2-18 shows the results of imaging a wire bond heat treated for 3 hours at 175°C from the backside at 1, 5, 10 and 30 kV. These voltages correspond to information depths of 0.008 μm, 0.12 μm, 0.4 μm and 2.5 μm in Al and 0.002 μm, 0.0235 μm, 0.081 μm and 0.51 μm in Au. Thus, at 30 kV, the information in the image comes from areas much deeper than the 1 μm thick Al metallization. The 1 kV image shows no indication of the Au /Al intermetallics. Al/Au intermetallics are clearly visible in the 5 kV image. This indicates that the intermetallics have not penetrated through the Al metallization. The image obtained at 10 kV shows slightly more amounts of intermetallic. At 30 kV the information depth is much greater than the thickness of the Al metallization so the entire projected image of the bond can be seen in the image. Also, it is important to note that the intermetallic compounds that form do not form evenly over the surface of the Au ball – Al metallization interface. It is also apparent that the intermetallic compounds form preferentially around the outside of the bond with little or no intermetallic compounds formed in the center of the bond.

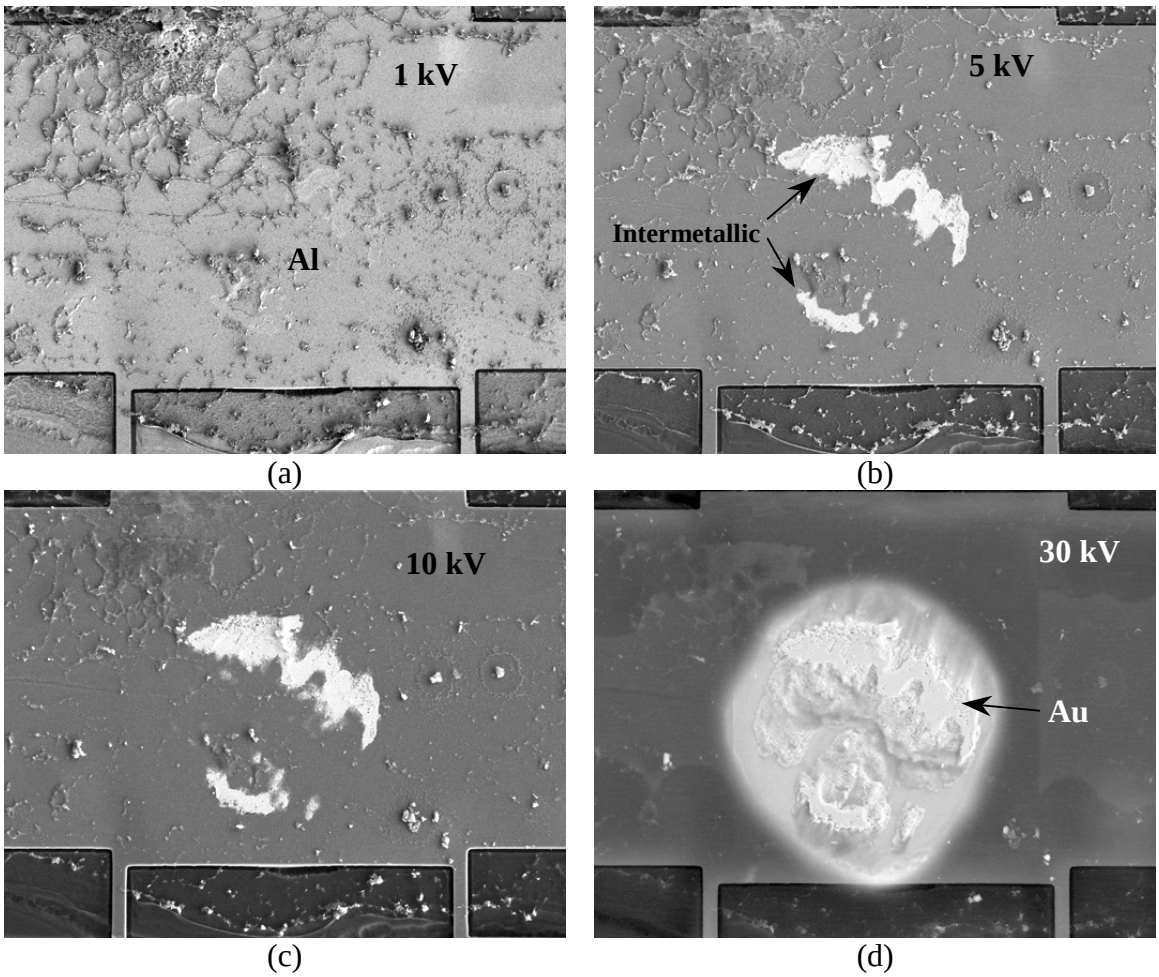

Figure 2-18. SEM images from back-thinned sample 322 – 3-hr heat treatment. Images were taken using different beam voltages, corresponding to different depth for the analysis. The analysis depth increases from (a) to (d).

Figure 2-19a shows a plan view of a wire bond at 10kV that demonstrates the typical appearance of the intermetallic around the outside of the bond with little or no intermetallic compounds at the center of the wirebond. A FIB cross section was cut in the center of the wire bond and is shown in Figure 2-19b. The FIB cross section extends across the entire width of the wire bond as shown in Figure 2-19b. Note the absence of intermetallic compound in the center of the bond pad. An image of the FIB cross section imaged with ions is shown in Figure 2-20a and b. Here the extent of intermetallic growth is visible. Figure 2-21 is a higher magnification image of the center of the bond pad and shows the grains in the Au ball, the small amount of intermetallic compound formed and the unreacted Al metallization.

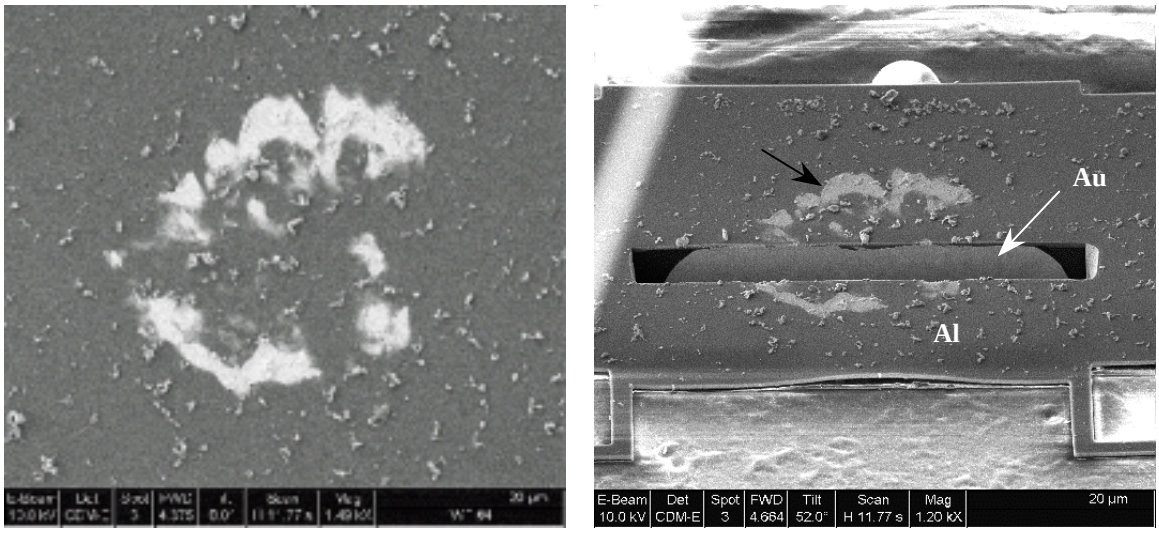

(a) (b)

Figure 2-19. SEM images from sample 323 (3 hr heat treatment). The image in (b) shows FIB techniques used to display cross-sectional information of the wirebond.

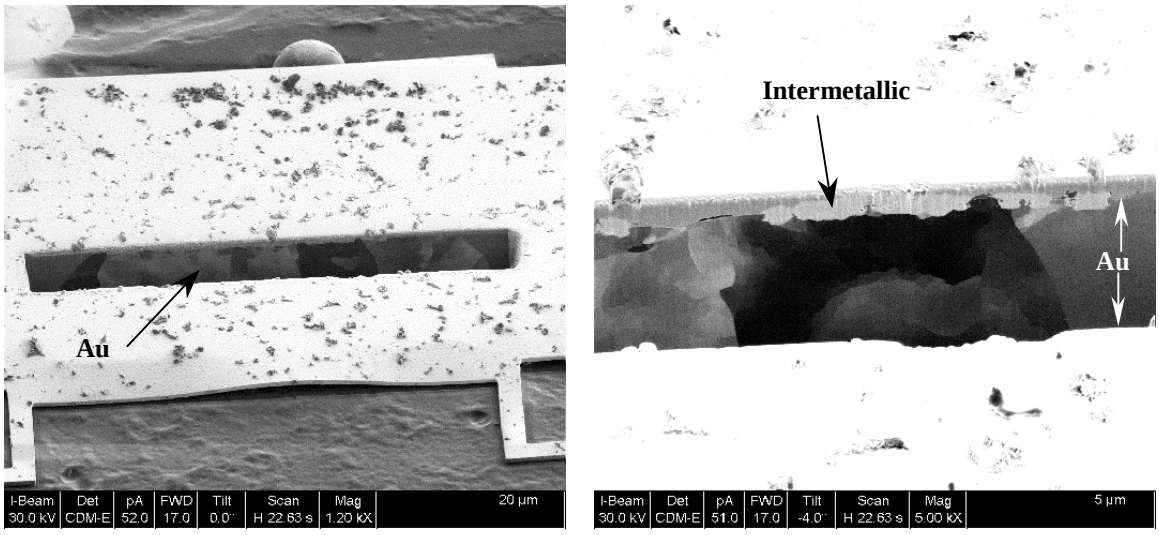

(a) (b)

Figure 2-20. Ion images from FIB sample 323 (3-hr heat treatment). The ion image differentiates compositional variations. Wirebond structure, including Al/Au intermetallic, can be seen in the cross-section images.

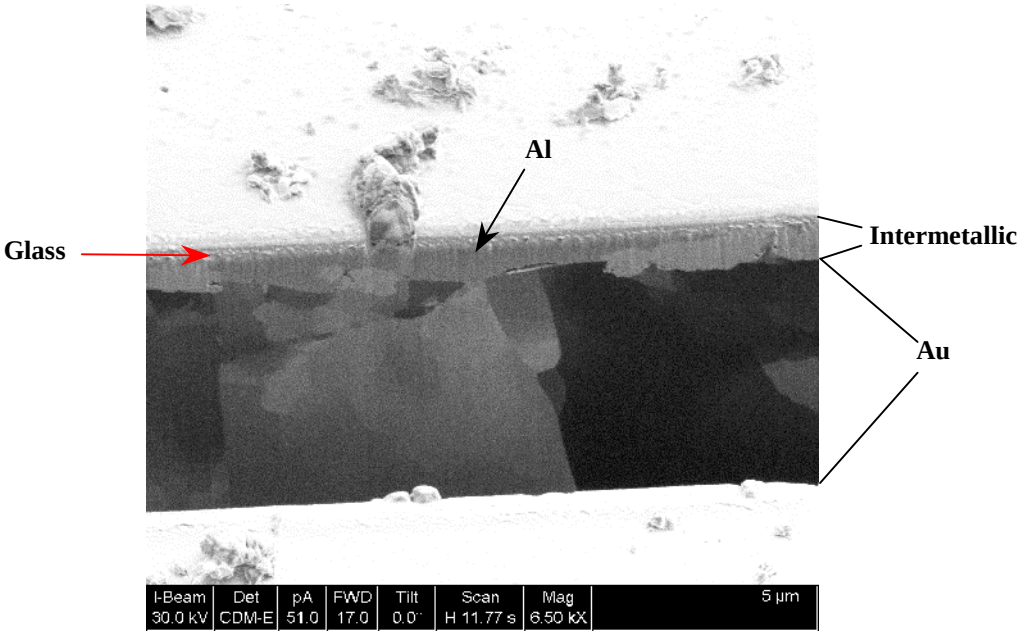

Figure 2-21. Higher magnifcation image of wirebond shown in Figure 2-20. Areas of Au, Al and Au/Al intermetallic can be seen.

Several devices were heat-treated for 24 hours at 175°C to produce an overaged structure. In reality, some commercial devices receive the equivalent of this heat treatment. Considerably more intermetallic is formed under these conditions. Several of these samples were examined using the same procedures described above. Figure 2-22 shows the SEM images obtained at 1kV, 5kV, 10kV and 30kV. Although there is some residual glass remaining on the bond pad, the same features that were visible in the 3-hour heat treatment sample are visible in the 24-hour heat treatment. Figure 2-23 is a 2 Kv image of a wire bond that was heat-treated for 24 hours. The extent of the intermetallic growth is much greater than that seen in the die heat-treated for 3 hours. Figure 2-23b is a FIB cross section through the wire bond shown in Figure 2-23a. The intermetallic compounds that have formed extend much farther into the wire bond than was seen for the 3-hour heat treatments. In Figure 2-24 higher magnification images of the 24-hour heat-treated wire bond are shown. At this longer time it is now possible to see Kirkendall voiding between the intermetallic compound and the Au wire. Note that in these regions the intermetallic compounds have fully consumed the Al metallization.

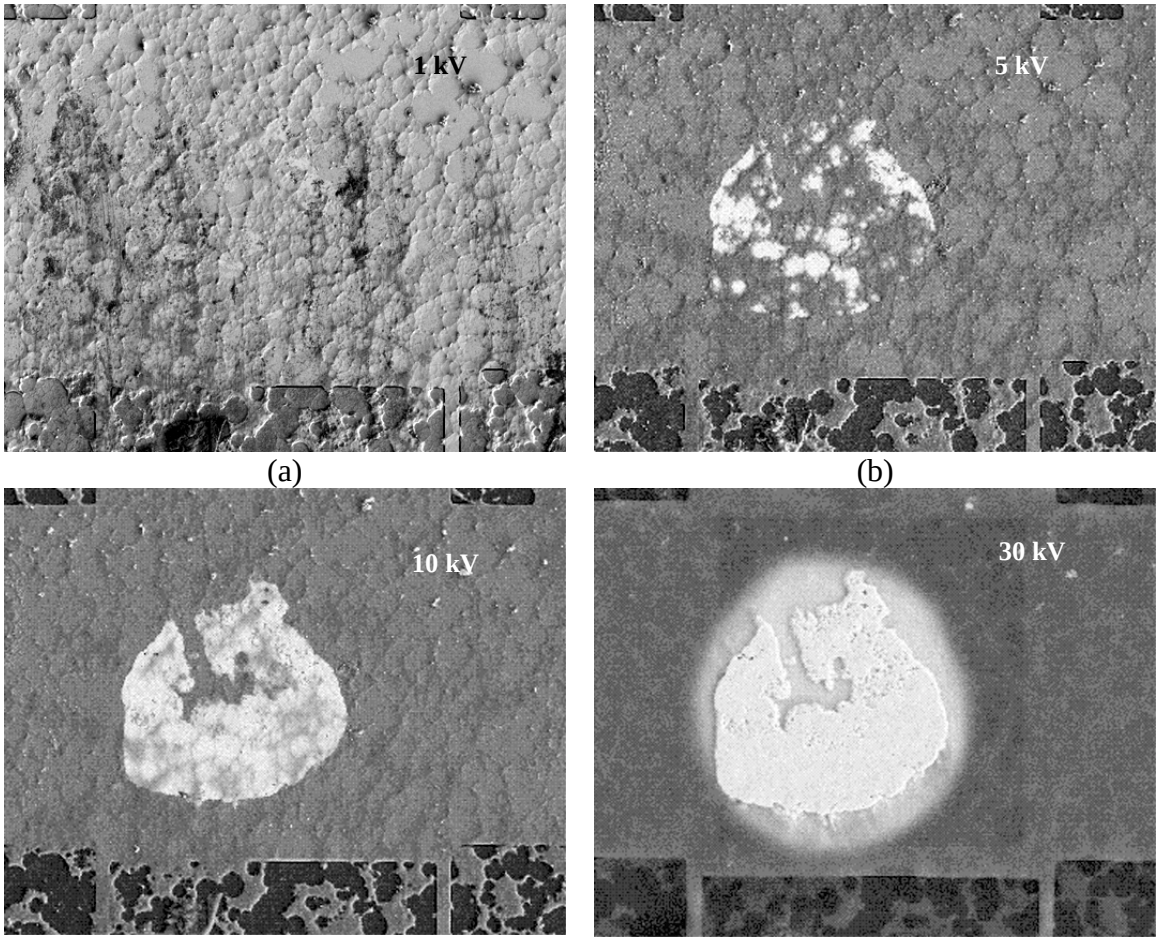

Figure 2-22. SEM images for sample 327 (24-hr heat treatment). Electron beam voltages are shown for each image. These voltages correspond to information depths of 0.008 μm, 0.12 μm, 0.4 μm and 2.5 μm in Al and 0.002 μm, 0.0235 μm, 0.081 μm and 0.51 μm in Au.

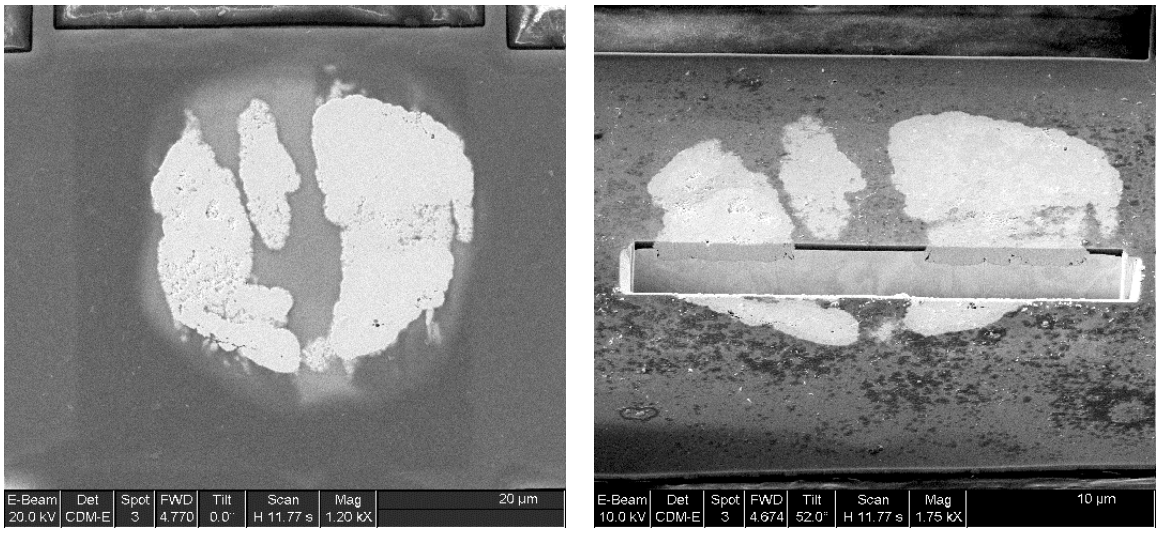

(a) (b)

Figure 2-23. Plan view and FIB SEM images for sample 328 (24 hr. heat treatment). Note the irregular distribution of intermetallic.

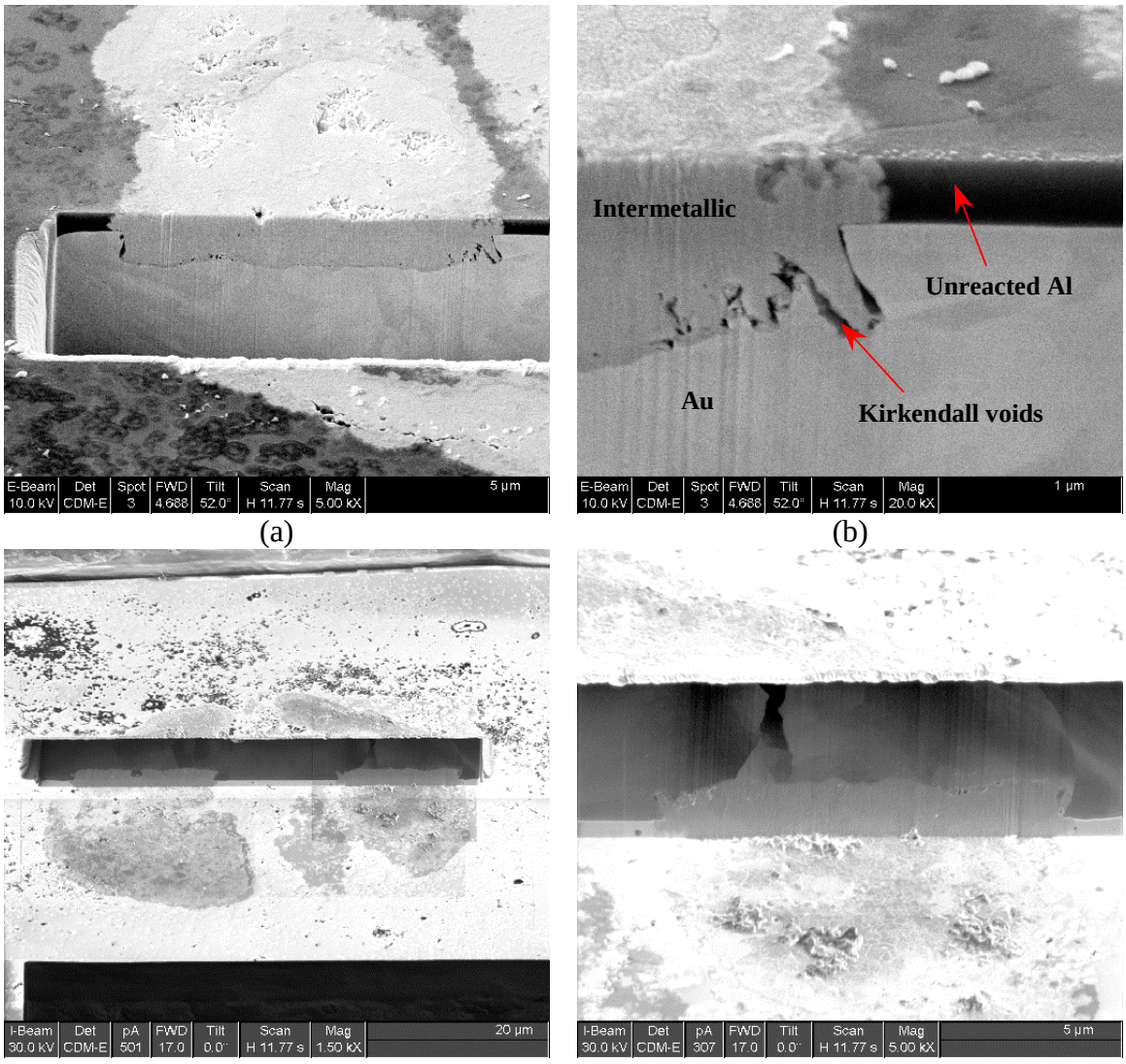

(a) (b)

(c) (d)

Figure 2-24. SEM images of FIB cuts for sample 328 (24 hr. heat treatment). Images are higher magnification of sample shown in Figure 2-23.

2.2.3.2 Identification of Au/Al Intermetallic Compounds in Wire Bonds

EBSD was used to help identify the intermetallic phases that form in a wire bond. A die that had been wire bonded followed by heat treatment at 175°C for 3 hours was back thinned and examined in a SEM equipped with an EBSD system for phase identification. A typical wire bond was selected. The EBSD patterns shown in Figure 2-25(c) and (d) were obtained from the area shown in Figure 2-25(a) and (b). This pattern allowed the phase to be identified as Au_2Al and is shown indexed in Figure 2-25. It can be inferred that the other phases that make up the bulk of the wire bond are Au_5Al_2 and Au_4Al as indicated in the figure. It should be noted that previous work has shown that

$Au_5Al_2$is the fastest growing Au/Al intermetallic and thus is expected to make up the bulk of the wirebond intermetallic.

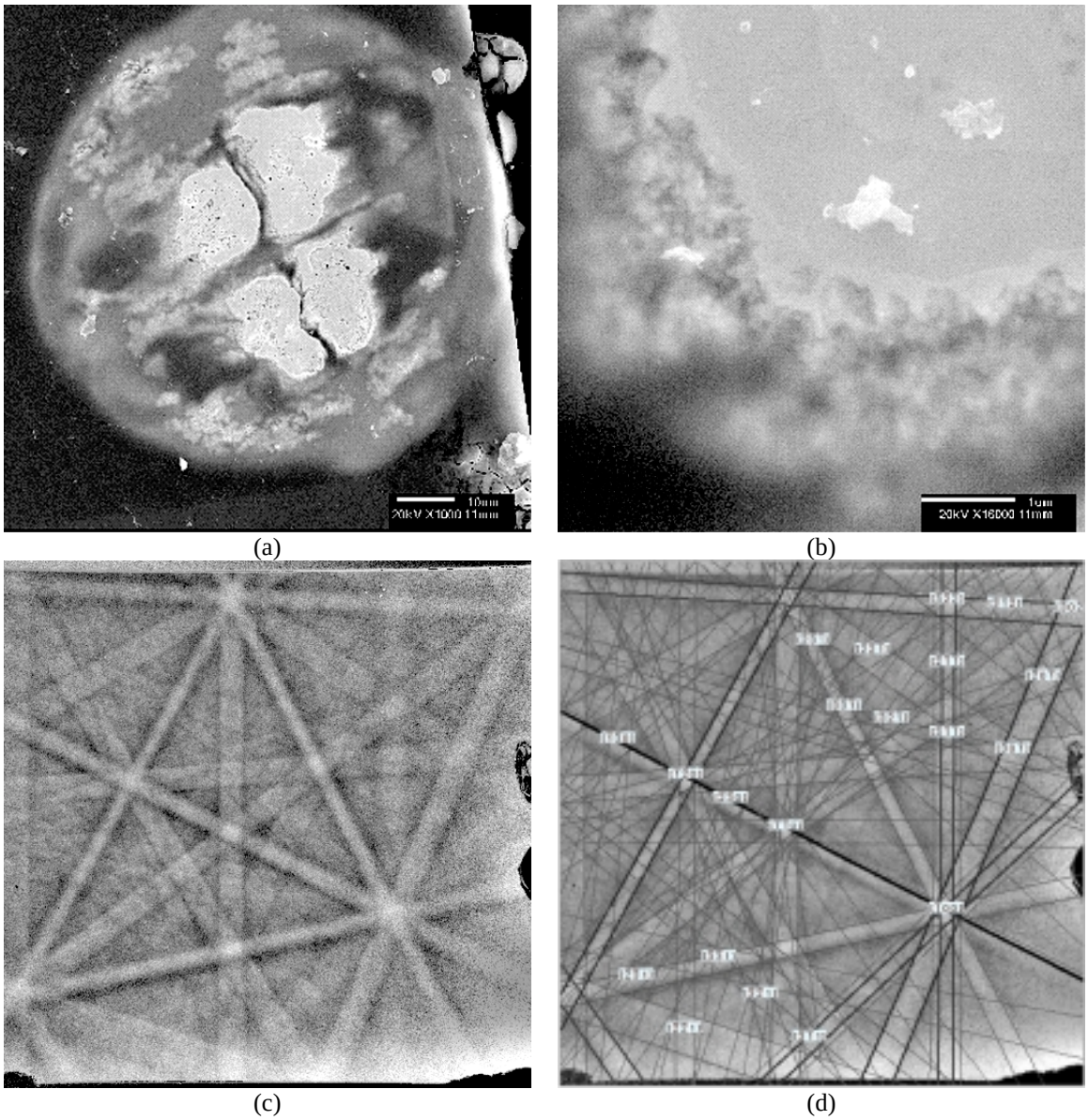

Figure 2-25. SEM and EBSD results from sample 275. EBSD patterns demonstrate that the intermetallic compound in contact with the Al is Au_2Al.

2.2.3.3 Microstructural Characterization of Corroded Wire bonds

Observations of wirebonds that were exposed to corrosive environments were limited to those devices that had received the standard 3-hour heat treatment at 175°C only. This heat treatment is felt to more accurately represent standard commercial processing conditions. The need to image the effects of the corrosion on the wire bonds required that the novel back thinning approach (described fully in Appendix A4) be utilized in conjunction with SEM and FIB analysis. In this portion of the study a large

number of devices were studied and the results presented here represent the typical wire bonds.

Figure 2-26 shows three bonds from a die (#326 3 hr HT) that had been exposed to an environment containing 100ppb Cl_2 and 70% RH (see Table A-1 in Appendix A1 for a list of all of the test conditions). The three images presented in Figure 2-26 represent wire bonds that had experienced different amounts of resistivity changes during the exposures. The wire bonds shown in Figure 2-26 represent resistivity changes of 14% in 10a (wirebond 22), 5% in 2-26(b) (wirebond 1) and less than 1 % in 2-26(c) (wirebond 12). It is clear from the images that the extent of corrosion scales with the resistivity changes. Figure 2-26(a) shows extensive corrosion of the Al bond pad, most of which is visible at the outer diameter of the Au ball. In comparison, it is not clear that there is any visible damage to the Al bond pad in Figure 2-26(c) where the resistivity change was less than 1%. The damage to the bondpad, shown in Figure 2-26(b), lies somewhere between these two extremes. In all cases the corrosion damage is limited to the Al bond pad and there is no apparent damage of the Au wire.

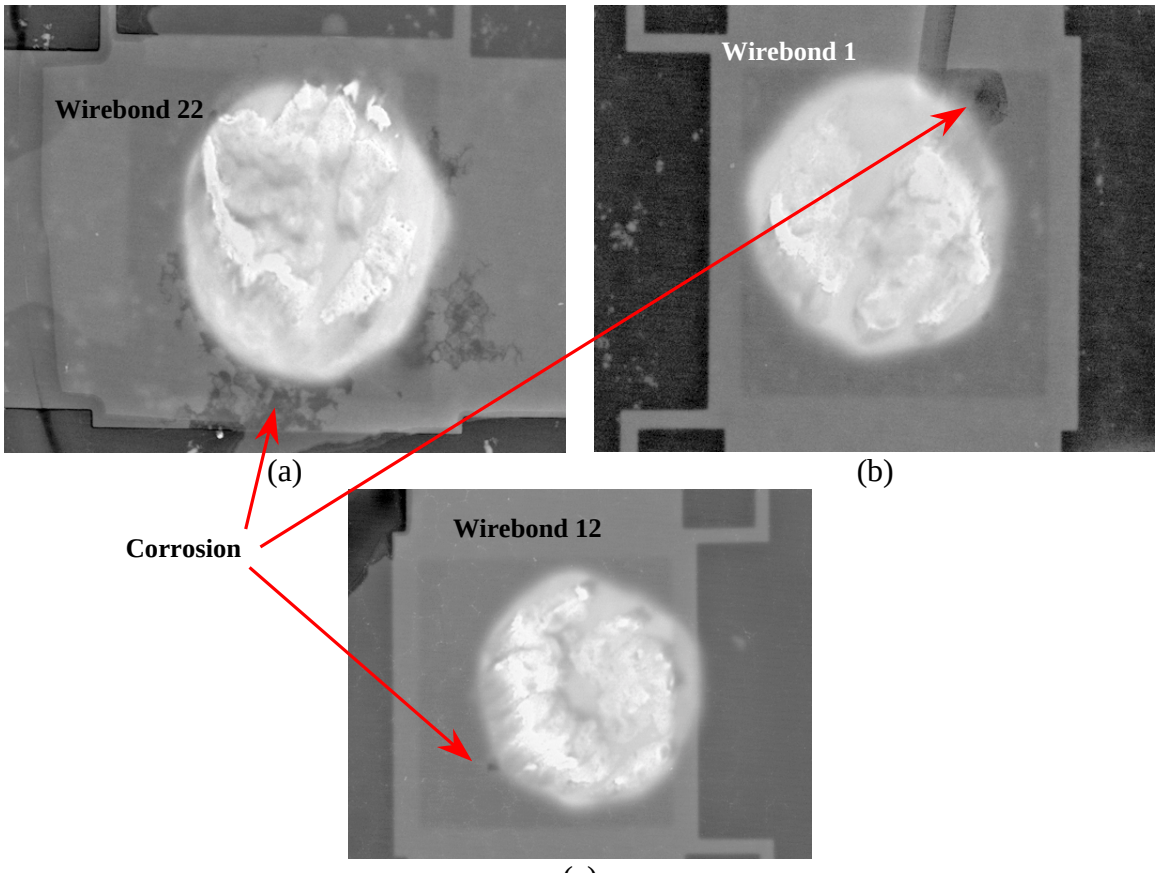

Figure 2-26. SEM images at 30 kV of wire bonds form sample 326. Image in (a) is for wirebond 22 (12% resistance change), (b) shows wirebond 1 (4 % resistance change), and (c) is for wirebond 12 (<1% resistance change)

Bond pad 12 was cross-sectioned using FIB. The results are shown in Figure 2-27 (a) and (b). The cross section shows that the intermetallic structure is typical of the three-hour heat treatment. In Figure 2-27(b) a small amount of corrosion may be seen in the Al metallization. There appears to be a small pocket of corrosion products in the Al metallization near the outer edge of the bond.

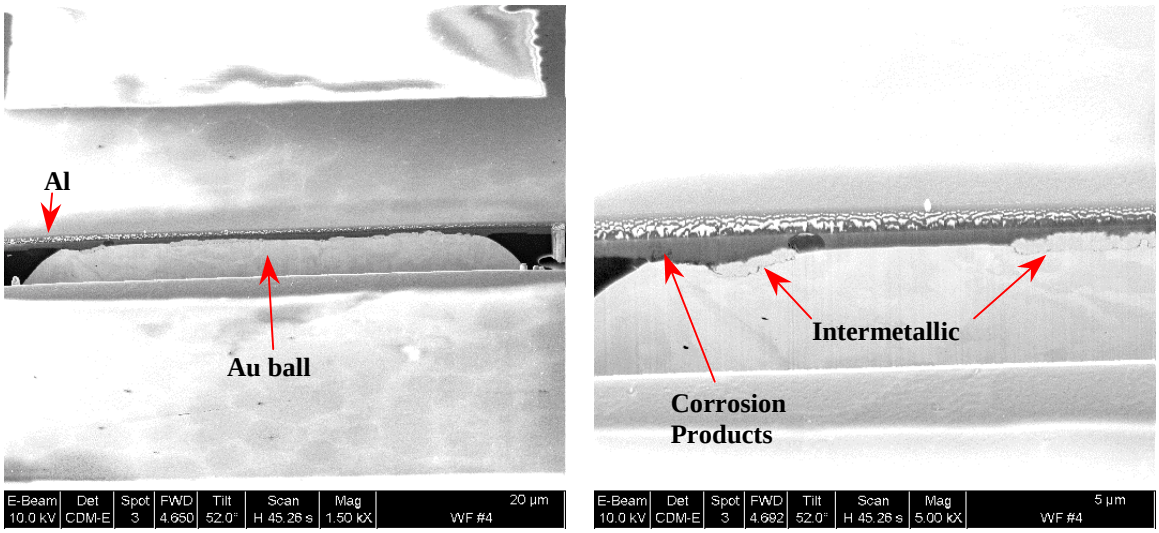

(a) (b)

Figure 2-27 SEM images for sample 326, wire bond #12 (see Figure 2-26(c). Note small amount of Al corrosion visible in (b).

A more detailed study of a heavily corroded bond pad was conducted. Figure 2-28 shows a wire bond that exhibited a resistivity change of 14% during a 10-day exposure. Figure 2-28(a) is a image of the bond at 1kV that shows the center of the wire bond to be covered with material that appears darker than the Al surrounding it. At a higher accelerating voltage (30kV, Figure 2-28(b)) the signal is coming from deeper within the sample and the intermetallic compounds are now visible below the dark material. In this image it appears as if there is no Al remaining in the center of the wire bond. In addition, corrosion damage to the bond pad around the wire bond can be seen. Figure 2-29(a) shows a low magnification image of a cross section of this bondpad. Note that the bond pad appears to be free of any remaining glass coating as can be seen from the exposed edge of the bondpad. Figure 2-29(b) is a higher magnification image that shows the details of the edge of the dark region. The Al metallization appears to be offset from the outside of the dark region with respect to the Al layer on the inside of the dark region. There also appears to be some corrosion product between the edge of the ball and the Al metallization. This offset of the Al metallization may have been a result of a build up of Al corrosion product under the wirebond. When the device was backthinned the pressure from the corrosion products may have resulted spalling or flaking of the remaining Al. Higher magnification views of the same wire bond are shown in Figure 2-30(a) and (b). Figure 2-30(a) is an electron beam image of the center of the bond pad. A small amount of Al metallization remains. It is separated from the Au wire by corrosion products. These corrosion products have caused the Al metallization to bow out from the

Au ball. Figure 2-30(b) is the same region imaged with the ion beam, which highlights the intermetallic compounds and the Al metallization.

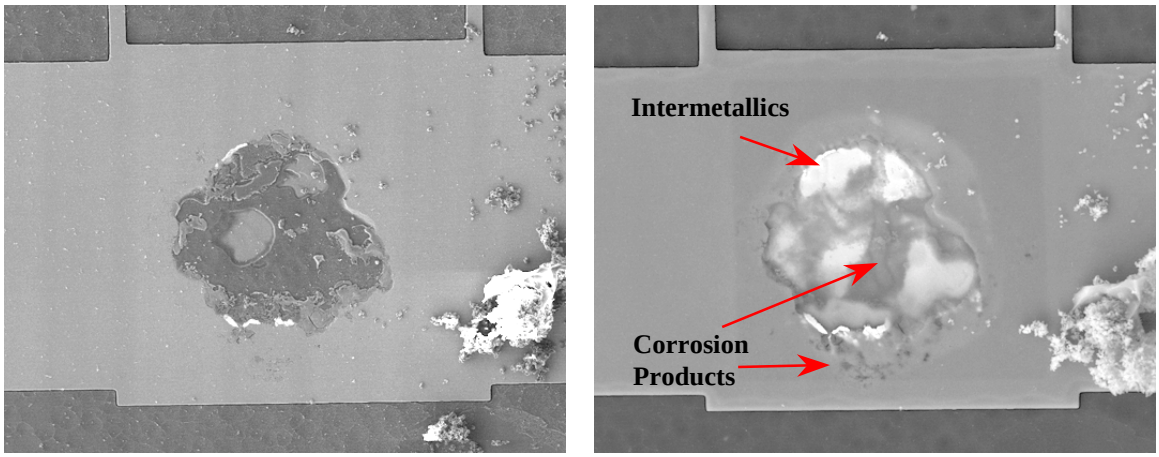

(a) (b)

Figure 2-28. SEM images from sample 335, bond pad 12, imaged at 1kV(a) and 30 kV(b). Note the corrosion product in the center of the bond area.

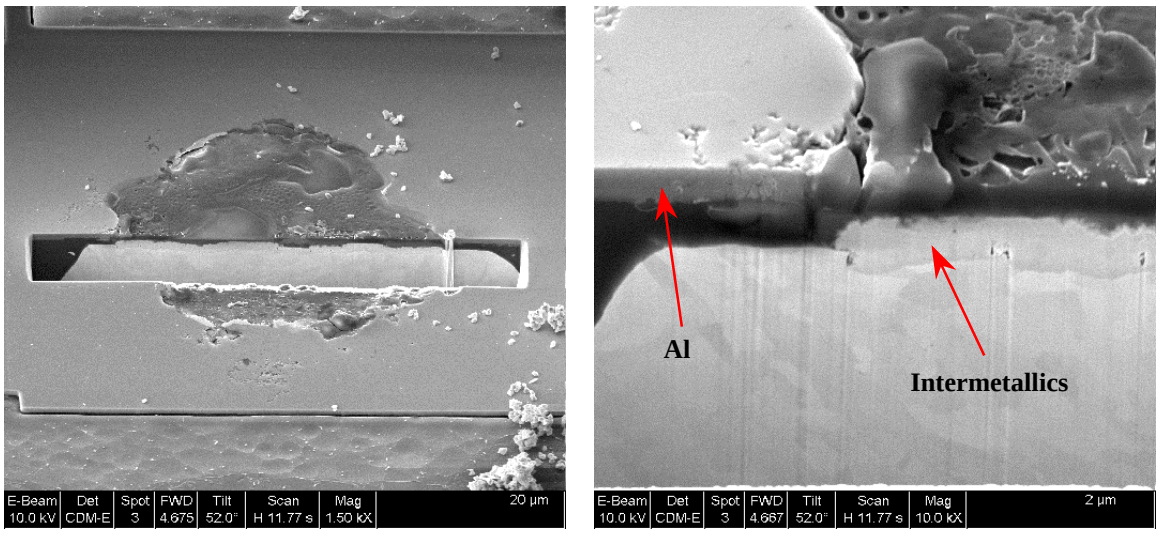

(a) (b)

Figure 2-29. Sample 335 bond 12 FIB cross section through bond pad. Image (a) shows general photo. Image (b) shows details at edge of bond. Note displacement of Al possibly due to corrosion between Al and Au.

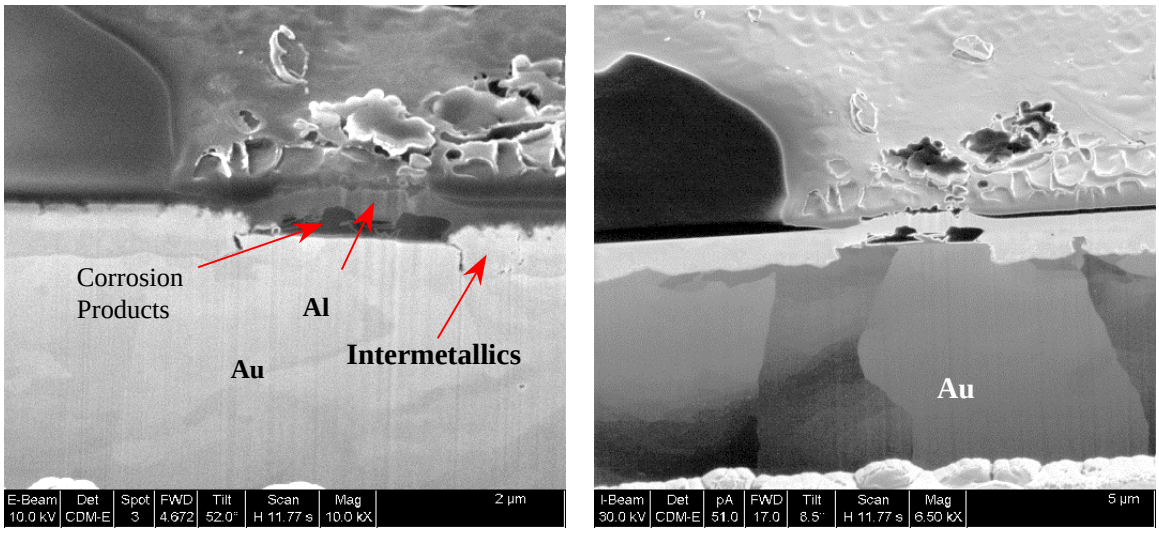

(a) (b)

Figure 2-30 Low magnification Electron (a) and Ion images (b) of bond center for cross section of bondpad 12, sample 335. Note the corrosion product between the Al (what little is left) and the Au intermetallic

In order to determine the nature of the Al corrosion a cross section was made through the corroded Al metallization at the very outside of the wire bond. This is shown in Figure 2-31(a). In this ion image, the Al grain structure of the bond pad is clearly visible at the top of the image. Also, the Al corrosion damage is visible as what appears to be a series of pits that occur on the grain boundaries present in the Al metallization. The penetration of the corrosion completely through the Al metallization is also apparent on the face of the cross section. Figure 2-31(b) is an ion-channeling image of the same cross section with the sample tilted so that the surface of the Al bond pad is normal to the ion beam. The crystallographic channeling of the ions in the primary beam results in different intensities within each grain that is dependent on the crystallographic orientation of the grain. Thus, these images are useful in correlating the location of the corrosion attack with the grains in the metallization. It is apparent that corrosion has progressed fastest at the Al grain boundaries. Also note that the area that imaged dark in SEM mode does not exhibit any channeling contrast. This confirms that the Al has been removed from this area either by corrosion or by a spalling of the remaining Al film by the corrosion products present between the intermetallic compounds and the Al metallization. The intergranular corrosion of the Al metallization is further confirmed in Figure 2-32. Figure 2B is an ion image of a cross section cut through the corroded Al metallization in the vicinity of the edge of the wire bond. The dark regions under the Al are filled with corrosion products. Note that the attack has mainly occurred along the grain boundaries.

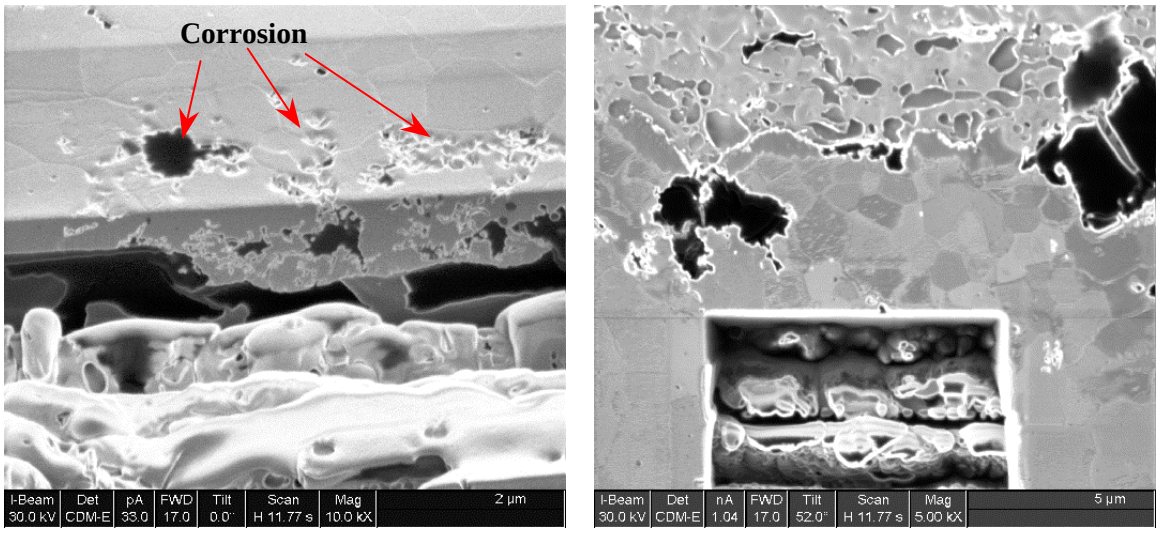

(a) (b)

Figure 2-31 SEM images of sample 335, bondpad 12. Photographs are ion images of cross-section through corroded Al. Image (a) shows a cross-section near the edge of the ball bond. The Al grains are clearly visible. Ion image (b) demonstrates there are Al grains outside of the corroded central area. There is some evidence for an corrosion attack at the grain boundaries in the AL

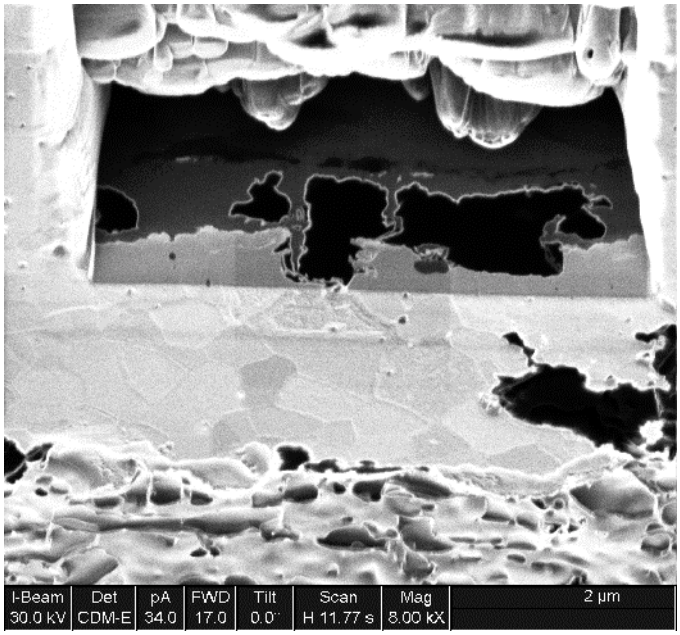

Figure 2-32. Ion image of cross-section of sample 335, bond 12 through corrosion pit in Al metallization.

2.2.3.4 Summary of Microsturctural Observations

As Heat-treated Wire bonds

1. The most striking feature in all of the wire bonds examined for his study is the uneven distribution of the intermetallic at the Al/Au interface. The distribution of intermetallics was confirmed by both SEM imaging using a range of accelerating voltages and FIB cross sectioning of bonds. This has been noticed in pull tested bonds previously and has been ascribed to either contamination of the Al bond pad, or a result of the heterogeneous deformation that the Au ball experiences during bonding.

2. The amount of intermetallic compound present increases with longer heat treatment times. Our results show that 3 hours at 175°C is representative of commercial practice.

Corroded bonds

1. The resistivity change scales well with the amount of corrosion damage observed in a wire bond.
2. The corrosion is observed to occur only in the Al metallization and is intergranular. The corrosion products are observed to form at the interface between the Al metallization and the Au/Al intermetallic compounds.

2.3 Mechanisms

Based on the bondpad resistance measurements and the microscopic examination of the corroded and as-received wirebonds, a description of the corrosion process can be generated. Clearly, the Al is more reactive than either the Au or the Au-Al intermetallics present at the Au/Al interface. Thus, any description of the corrosion process must include a treatment or explanation of the role of the intermetallics on bondpad corrosion.

2.3.1 Intermetallic Analysis

The shape of the resistance curves, as described above consists of regions of gradual increases and several abrupt steps. This is suggestive of a system containing parallel resistance paths. Figure 2-33 shows a schematic representation of this and how it correlates with the resistance data. Because the resistance is a function of the length of the path and the cross-sectional area, a general narrowing of any or all of the traces results in a gradual, continuous increase in resistance. When an entire path is removed, a step in resistance would be observed. This process is illustrated in Figure 2-33.

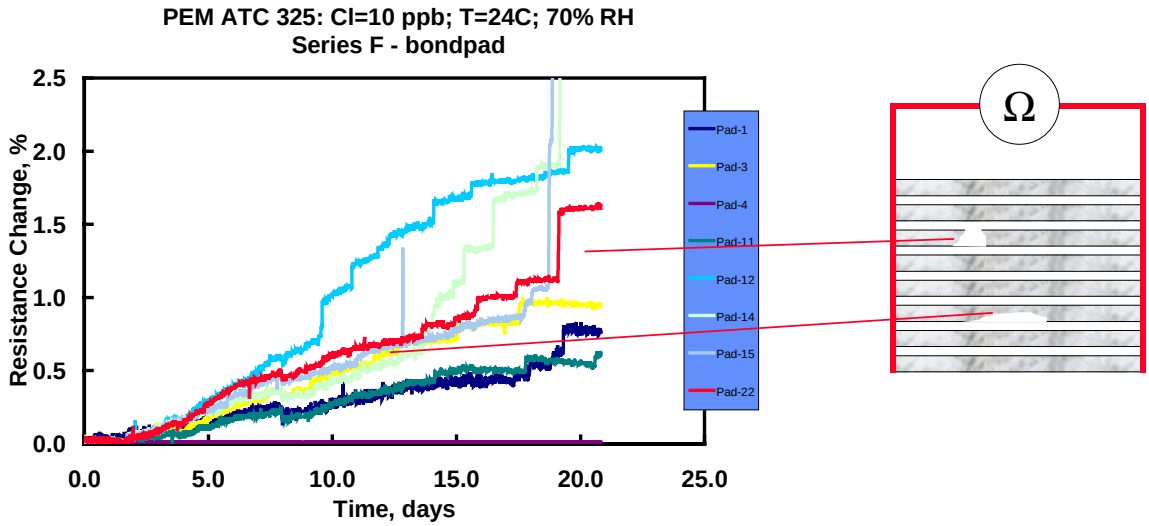

Figure 2-33. Resistance plot for ATC and schematic representation of Al lines. General attack along any or all of the lines leads to a gradual increase in resistance, while opening a line results in a stepped increase.

Physically, describing the wirebond as a group of parallel paths is not illogical. As was found with the back-thinned samples, the intermetallic that forms is not a uniform layer. Rather it is a complex mixture of Al, Au and intermetallic. The conductivity of the Au-Al intermetallic phases is significantly lower than for either gold or aluminum (see resistivity Table 2-2). Thus the intermetallic regions act essentially as barriers for current flow. When an area of Al separating the intermetallic islands is removed by corrosion, the current is forced to travel through the intermetallic, resulting in a step in resistance.

Table 2-2. Resistivities of Au/Al Intermetallics

	Al	$AuAl_2$	AuAl	Au_2Al	Au_5Al_2	Au_4Al	Au
Resistivity (μΩ-cm)	3.2	7.9	12.4	13.1	25.5	37.5	2.3

To confirm that the steps observed in the resistance curves are related to corrosion of Al areas, finite element modeling of the wirebond resistance was performed. A simplified wirebond structure consisting of columns of intermetallic was used. In addition, it was assumed that the intermetallic consisted entirely of Au_5Al_2, the fastest growing intermetallic compound.[4] An example of an intermetallic distribution input file is presented in Figure 2-34(a). The red in the figure represents Al and the blue represents the Au_5Al_2 intermetallic.

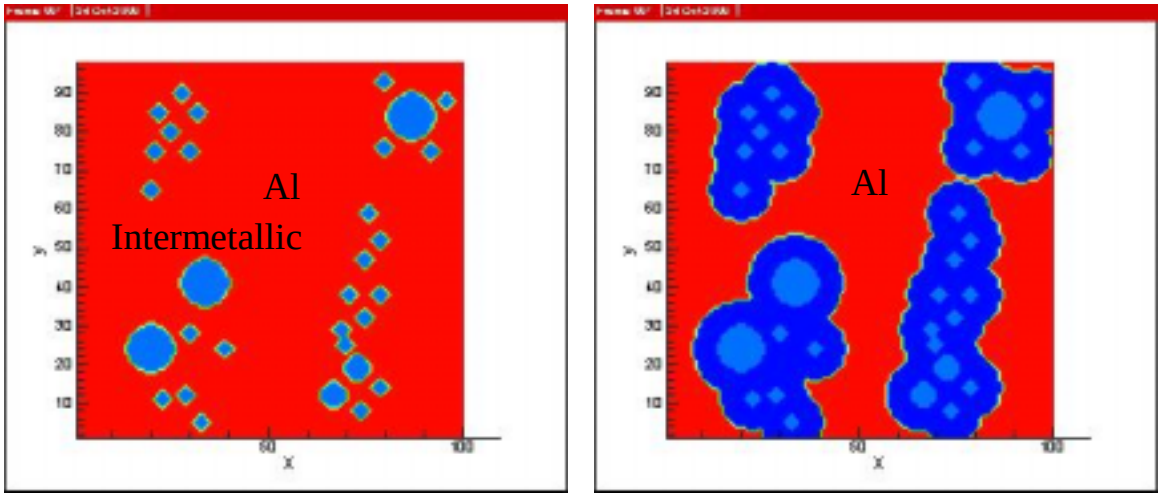

(a) (b)

Figure 2-34 Map of intermetallic columns used for finite element simulation (a) and after corrosion consumes some of the Al (b).

To provide input files to the finite element code, the bondpad was allowed to "corrode". The corrosion was assumed to initiate at the Al-intermetallic interface and allowed to progress radially outward at a constant outward rate, consuming Al and leaving corrosion products. An output file was written after each step, which became an input file for the finite element simulation. The resulting map is shown in Figure 2-34(b), which represents the same bondpad after corrosion has consumed some of the Al. The corroded area is shown as the darker blue around the intermetallic columns.

The files produced by the corrosion simulation were used as input files to the finite element simulation. Current entered the sheet along one edge and left through the opposite edge.

The distribution of electrical potential, ϕ, in a medium that is conducting current at steady state (in this case, the bondpad), is governed by the Laplace equation, $\nabla\bullet(\kappa\phi) = 0$, where κ is the conductivity of the medium. To analyze the distribution of potential in a finite body, the space of interest is discretized into a uniform grid, and appropriate (known) current fluxes are applied as boundary conditions to the external surfaces. The Laplace equation is solved at each grid point using an iterative biconjugate gradient technique.[5] In one dimension, this entails solving the partial differential equation,

$$\frac{\kappa_{i-1}+\kappa_i}{2\delta^2}\phi_{i-1} - \frac{\kappa_{i-1}+2\kappa_i+\kappa_{i+1}}{2\delta^2}\phi_i + \frac{\kappa_i+\kappa_{i+1}}{2\delta^2}\phi_{i+1} = 0, \qquad [?]$$

where i denotes the grid point of interest, i-1 and i+1 are the adjacent grid points, and δ is the grid spacing. At an external boundary (e.g., where the grid point at i-1 is absent), the equation becomes

$$\frac{\kappa_i+\kappa_{i+1}}{\delta^2}\phi_i + \frac{\kappa_i+\kappa_{i+1}}{\delta^2}\phi_{i+1} = \frac{2I}{\delta}, \qquad [?]$$

where I is the prescribed current density at the boundary. The extension to three dimensions is straightforward.

To compute the temporal evolution of the resistance in a PEM, an idealized representation of the region around a Au bondpad is constructed. This consists of a cylinder of Au with 45μm radius and 25μm height, attached to a volume of Al measuring 100μm x 100μm x 1.5μm. The remaining volume is vacuum. The Al contains regions of intermetallic and corroded material that evolve with time to produce variations in the resistance of the composite system. The resistivity of the Au, Al, and intermetallic materials is 2.3, 3.2, and 20 μΩ-cm, respectively. The corroded material is insulating. The conjugate gradient calculations are preformed on a 100x100x31 grid with increments measuring 1μm x 1μm x 0.25μm, with 10mA total current applied across the Al. The total resistance is computed using the 10mA total current and the difference in average potential between the two boundaries where the current is applied.

An example of the simulation results is presented in Figure 2-35. An intermediate time view of the bondpad is presented in (a) and the calculated resistance curves is shown in (b). The resistance curve (b) exhibits regions of gradual increase combined with stepped increases. The steps correlate with the joining of corroded areas in (a), and are the result of a current path (Al) being eliminated. These results are certainly consistent with our understanding of the wirebond structure. For the 3-hour heat treatment, the intermetallic does not cover the entire bondpad, and individual Al islands can be seen (Figure 2-28(b)). As the islands corrode, steps are observed in the resistance response. In contrast, for the 24-hour heat treatment, the intermetallic exists essentially as a single large island (Figure 2-22(d)). Because there are no individual Al areas to be removed, the resistance curve is basically a continuous increase, with little evidence of steps (Figure 2-2(c)).

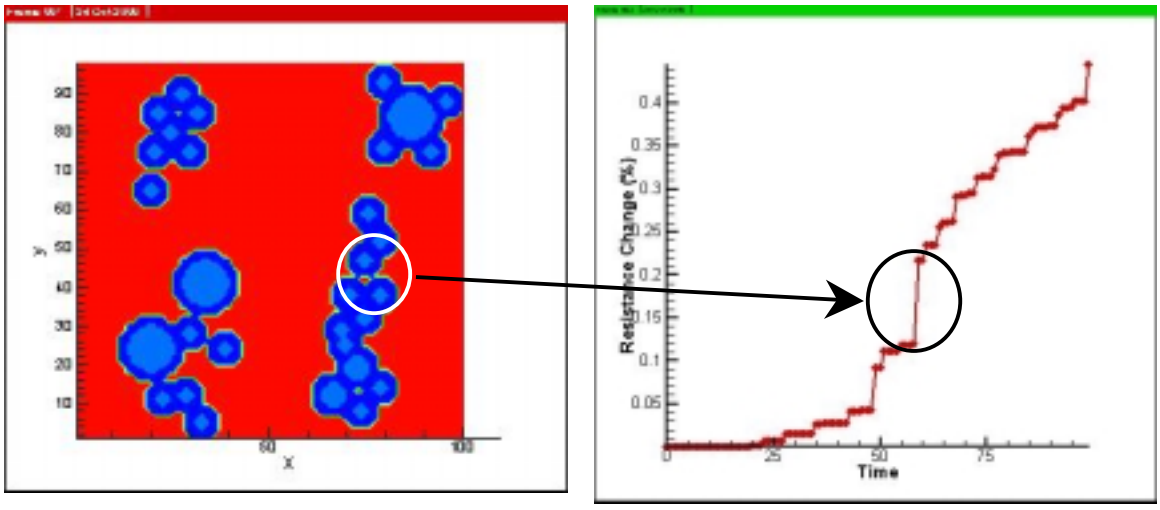

(a) (b)

Figure 2-35 Map of intermetallic columns used for finite element simulation (a) calculated resistance change resulting from corrosion simulation.

Based on the kinetic measurements and the structural investigation, a description of bondpad corrosion can be developed. It includes the following features:

- Al bondpads undergo general corrosion (not pitting) with some evidence of intergranular attack.
- Bondpad corrosion is galvanically driven. Galvanic coupling to the Au decreases the initiation induction time and accelerates the corrosion rate
- Increasing humidity, temperature, and chlorine concentration increases the corrosion rate
- Corrosion initiates at the Au/Al interface and propagates around the ball bond and across the bondpad.
- The amount of intermetallic formed at the Al/Au interface affects the corrosion rate

3.0 Model Development

Although not all aspects of the bondpad corrosion mechanism have been identified and characterized, an initial mathematical model of the degradation in performance due to bondpad corrosion has been formulated and exercised. This concurrent modeling exercise has provided a number of benefits, including (1) demonstrating the usefulness of our integrated approach and implementation strategy, (2) improving the efficiency of the experimental portions of the project, (3) providing adequate time for identifying and addressing unique numerical needs (e.g., incorporating time-variant environmental data), and (4) establishing an active interface with the end user (electrical system performance).

As described in the previous sections, our approach first concentrated on characterizing the corrosion characteristics of bare, unpassivated Al bondpads ("intrinsic" behavior). A significant effort was performed to address the effect of heat-treatment and assess the cause of the variability in the measured kinetic response. Once a physical-based understanding of the corrosion process was obtained, our intent was to develop a phenomenological model that describes the kinetics of bondpad corrosion without any plastic encapsulant present. The next step involved including water and contaminant transport processes within the encapsulant to determine how the local "die-level" environment is modified. This resulting continuum-level deterministic model, in turn, can be directly coupled with uncertainty analysis and age-aware electrical models to assess the effect of device corrosion on the performance or reliability of an electrical system. The resulting first-generation integrated model is described in this section.

3.1 Intrinsic (Deterministic) Corrosion Model

Bondpad degradation was measured as a function of three prime environmental parameters: temperature (T), relative humidity (RH), and gaseous contaminant concentration ($[Cl_2]$). Our objective in this part of the study was to formulate a simple mathematical relationship linking these parameters to the corrosion rate (CR) of the bondpad. For example,

$$CR_{bondpad} = f([Cl_2]) \bullet g(T) \bullet h(RH)$$

For bondpad corrosion, we showed in Section 2 that the change in sheet resistance is an effective metric for the extent of corrosion. We should note here that corrosion affects the electrical function of a device by causing an increase in resistance of the wirebond itself. Of importance and as shown previously in Figure 2-1, the sheet resistance change that we use in this study is not a direct measure of this change in wirebond resistance.

Consideration of the kinetic data presented in Section 2.1 led to the several observations concerning the change in sheet resistance (refer to Figure 3-1). First, if the same rate data shown in (a) are plotted on a linear scale (b), the response is generally linear with time up until the time of rapid bondpad failure (open circuit). Thus, under constant environmental conditions used in these experiments

$$\frac{d(\Delta R / R_o)}{dt} = k$$

The dramatic effect of chlorine concentration ($[Cl_2]$) is evident by comparing (b) with (c) and (d). Also, at the slower corrosion rates, an induction period is obvious that is probably related to initiation of corrosion (initial breakdown of the passive oxide on the Al). Usually the linear response occurs for ΔR values less than 10%. Such a linear rate would be consistent with control by a transport process (e.g., oxidizing reactant) and a small change in the interfacial area at which the heterogeneous reaction is occurring. This latter factor could be easily satisfied given that the resistance change is limited to 10%. Based on the observations documented in Section 2, we believe that the considerable scatter that exists in these rate data between the individual bondpads is due to differences in the distributions of the intermetallic phases. Other factors could be unaccounted forgeometric effects (e.g., bond location, water condensation, galvanic interactions) or possibly even the stochastic nature of the Al corrosion process itself.

All of the resistance data were then compiled and resistance changes of $> 10\%$ were discarded. A linear regression on the resulting data for each bondpad was performed to determine the rate constant (k). Multi-variable analyses using all rate constants were conducted to determine the effect of chlorine concentration, temperature and relative humidity on the corrosion process.

Another example compilation of the kinetics obtained using similar conditions except with a varying chlorine concentration is shown in Figure 3-2(a). Again, it is clear that increasing the chlorine concentration increases the corrosion rate. However, there is a limiting value of $[Cl_2]$ above which the rate no longer increases (Figure 3-2(b)). For reference, data exist above 150 ppb but are not shown. Up to this limit, there appears to be a linear relationship between chlorine concentration and the corrosion rate. This linear behavior is consistent with a first-order surface reaction or possible mass transport control. The 150 ppb limit may be due to a saturation effect (adsorbed water layer or surface) or a change in mechanism. For example, the corrosion rate could be controlled

by the supply of the oxidizing chlorine to the surface at lower concentrations. Then, at higher levels, anodically driven chemical precipitation processes could be needed to maintain continuity between corroding regions and the external environment. As a reminder, the levels of chlorine used in this study should be considered as highly accelerating. In most urban and industrial environments, actual levels are much lower than these.

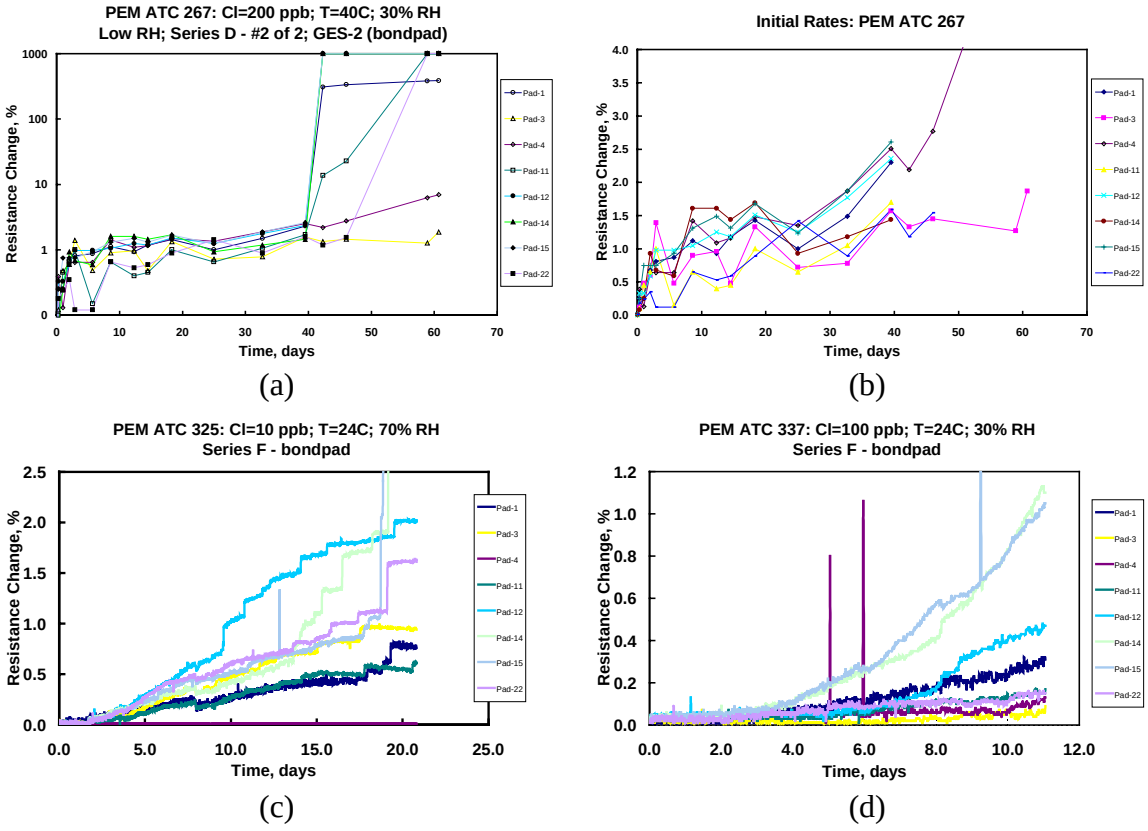

Figure 3-1. Kinetic data showing the relatively linear response prior to bondpad failure: (a) data plotted on a logarithmic scale (sudden failure above ~10% change, (b) same data in (a) plotted on linear scale; (c) and (d) censored data for conditions with lower [Cl_2]. Note the differences between individual bondpads on each single ATC device.

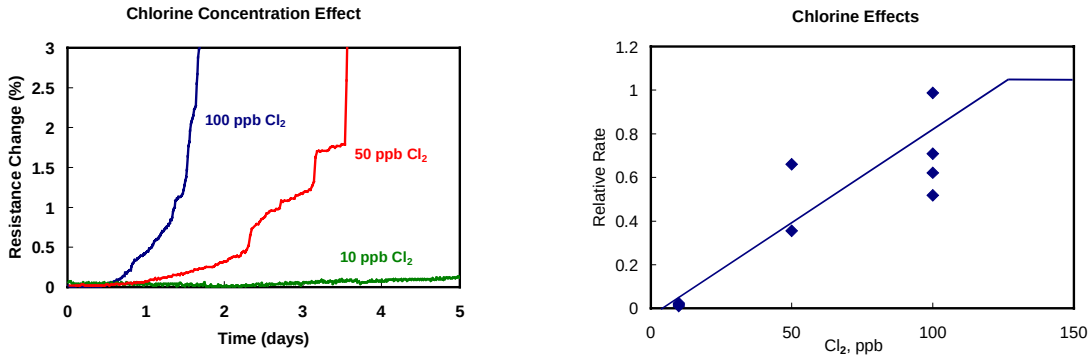

(a) (b)

Figure 3-2. The effect of chlorine concentration on wirebond corrosion: (a) typical raw data and (b) resulting relationship.

Similarly, the effect of relative humidity is shown in Figure 3-3. Based on most atmospheric corrosion situations, the expected positive correlation between the relative humidity and corrosion rate was observed. The data (e.g., those shown in (a)) were fitted to a sigmoidal curve that is also typically observed. Based on this response, the critical humidity for Au/Al wirebond corrosion is around 20% RH.

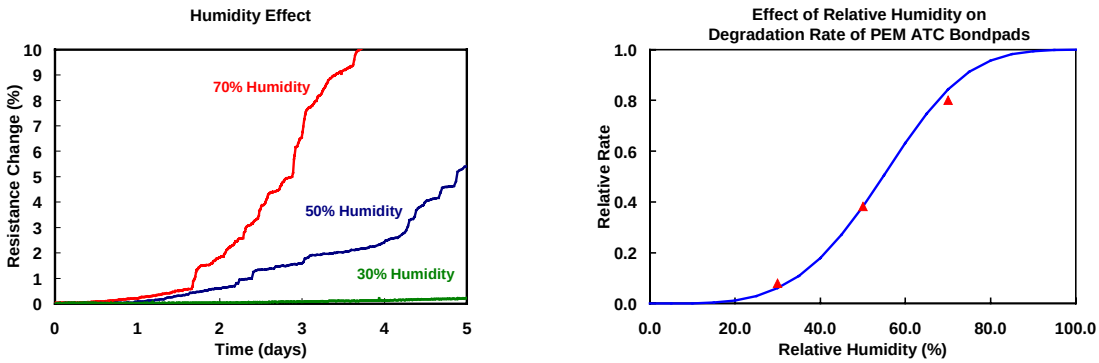

(a) (b)

Figure 3-3. Effect of relative humidity on wirebond corrosion: (a) typical raw data and (b) resulting relationship.

A multi-variable analysis was performed on all the kinetic resistance-change data that resulted in the following deterministic equation:

$$\frac{d(\Delta R/R_o)}{dt} = k_o P_{Cl_2} \left\{ 1 - \exp\left[-\left(\frac{H}{\eta} \right)^{\beta} \right] \right\} \exp\left[-\frac{E_a}{RT} \right]$$

where $\Delta R/R_o$ is the change in wirebond resistance, k_o is the surface reaction rate constant, P_{Cl_2} is the concentration of gaseous chlorine, H is the relative humidity, E_a is the activation energy, and T is the temperature. Values for each of the specific parameters were also calculated (β=2.5, η=55, E_a = 0.8 eV or 17.5 kcal/mole). Note that the activation energy is completely consistent with other investigators measurements of this parameter.[1] The values for k_o will be discussed in Section 3.3.

3.2 Effect of the Plastic Encapsulant

3.2.1 General considerations

The plastic encapsulant that covers the wirebond surface in actual PEM devices has two direct effects on corrosion behavior: (1) it can modify the local environment relative to the external conditions (i.e. temperature, humidity, and contaminant), and (2) if the plastic properly wets the wire and the wirebond, it can function as an effective "mastic" or barrier material. That is, the plastic can prevent corrosion because it can physically prevent the existence of an adequate adsorbed layer or puddle of water. Therefore, to advance the capabilities of the intrinsic corrosion model to include the presence of the plastic encapsulant, two efforts were initially pursued: a mathematical analysis of the governing transport processes using relevant physical configurations, and a related experimental activity to provide validation data. The decision was made to just study best-commercial-practice technology because only new PEM devices will be used in our systems. During the pursuit of the device-level validation information a very significant discovery was made: BCP parts are very robust and are practically impossible to fail using reasonable accelerated aging conditions that include external contamination and elevated humidity (= mastic function #2). Typical kinetic results from long-term accelerated aging that support this conclusion were shown previously in Figure 2-4.

In addition, some ancillary work was performed with commercial hex inverters, which showed that physical defects in the plastic are probably necessary to provide a permeation path for externally available contamination. Such defects are typically produced during manufacturing or caused by subsequent thermal testing. In a related study at CALCE, investigators recently found that the permeability of the most common detrimental contaminant (aqueous Cl^-) through a typical plastic epoxy material is practically zero. Because the plastic is very permeable to water, the real role of the defects is the introduction of corrosion accelerating contamination. Thus, those defects that run from the surface to the interior of the die (e.g., along lead-frame metallization) are especially important. Figure 3-4 demonstrates the detrimental effect of having significant defects present on the failure of these hex inverters.

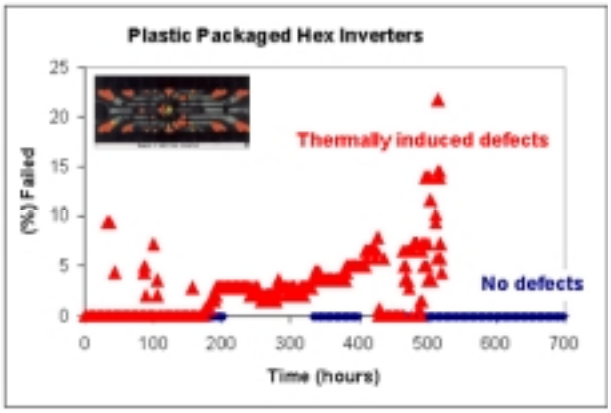

Figure 3-4. Failure data for commercial HEX inverters showing the effect of defects in the plastic. The inset shows the presence of thermally induced defects (taken with a scanning acoustic microscope).

3.2.2 Effect of periodic humidity and thermal transients

Given that transport of moisture through the bulk plastic does not apparently affect the corrosion behavior, the focus of the mathematical analysis of moisture and heat transport was directed at determining the potential influence of periodic daily and annual environmental transients. The concern is that in real use, the external environment is not constant and that these transients could lead to quite different conditions at the die (within defects) than are produced during the constant conditions associated with the experimental exposures. The general finding from these analyses is that for the physical configuration of actual devices and normally expected conditions, heat and mass transport processes should not significantly affect moisture levels at the die. However, it should be noted that for some unusual configurations and environments, these transport processes could yield a more aggressive transient internal environment.

The remainder of this subsection contains a summary of the analysis of the relationship of heat and mass transfer to the moisture exposure of a die covered by a thin layer of molding compound that is exposed to periodic variations in the ambient temperature T_{amb} and relative humidity H_{amb}. The detailed mathematical treatment is contained in Appendix B. For purposes of illustration, the periodic variations in relative humidity are assumed such that the moisture concentration in the molding compound at the free surface varies sinusoidally. The analyses follow the approach of previous authors who have treated moisture transport in plastic packaged devices as one-dimensional diffusion.[6,7] Heat transfer in the molding compound is considered first, then moisture transport is examined.

Heat transfer in the molding compound is very rapid relative to the temperature cycle times of interest. For example, the characteristic thermal diffusion time $t_\alpha = l^2/\alpha$ is very small (on the order of 5×10^{-5} day or less) relative to a cycle time of one day or one year. Therefore, the temperature of the molding compound should be essentially uniform and equal to the ambient temperature.

Mass transfer is relatively much slower than heat transfer. The characteristic diffusion time $t_D = l'^2/D$ for water transport is very large (varying from ~20 to ~10^4 days as the temperature varies from 40 to –40° C) relative to a cycle time of 1 day. Therefore, the concentration at positions near the interface with the die is relatively unaffected by the fluctuations at the surface. Instead, the response near the die reflects the effect of the average of the periodic variations in the water concentration at the surface of the molding compound.

For a cycle time of 365 days, the characteristic diffusion time t_D is now similar in magnitude to the yearly cycle time. The periodic variations in water concentration that occur at the surface of the molding compound cause phase-shifted periodic variations in the water concentration at the interface with the die. The amplitude of the variation and the phase shift ϕ will depend on the thickness of the molding compound, temperature history, and corresponding average diffusion coefficient. For typical parameter values and temperature histories of interest, the amplitude of the periodic variation at the die will be the same as or less than the amplitude at the surface of the molding compound, and a phase shift of between 0 and 2π radians is reasonable for some scenarios. The number of possible scenarios is large. Therefore, only some limiting cases are considered briefly to illustrate the range of the effects that can result from a phase shift ϕ in the periodic variation in water concentration.

First, consider the case in which the yearly variations in temperature and humidity are in phase; the maximum temperature and maximum humidity occur at the same time. At the interface with the die, let the amplitude $A = 1$. If the phase shift $\phi = 0$ or $\pm 2m\pi$ radians, where m is an integer, then the temperature and relative humidity variations occurring at the interface with the die are also in phase and are the same as those occurring at the surface of the molding compound. The maximum temperature and maximum humidity occur at the same time. However, if the phase shift $\phi = (2m-1)\pi$, where m is an integer, then the temperature and relative humidity variations occurring at the interface with the die are a odd multiple of π radians out of phase with those occurring at the surface of the molding compound. The minimum humidity will occur at the maximum temperature, and conversely, which is exactly opposite to the conditions at the surface of the molding compound.

Next, consider the case in which the yearly variations in temperature and humidity are out of phase; the minimum humidity occurs at the maximum temperature, and conversely. Again, at the interface with the die, let the amplitude $A = 1$. If the phase shift $\phi = 0$ or $\pm 2m\pi$ radians, where m is an integer, then the temperature and relative humidity variations occurring at the interface with the die are also out of phase and are the same as those occurring at the surface of the molding compound. The minimum humidity and maximum temperature occur at the same time. However, if the phase shift $\phi = (2m-1)\pi$, where m is an integer, then the temperature and relative humidity variations occurring at the interface with the die are a odd multiple of π radians out of phase with those occurring at the surface of the molding compound. The maximum

humidity will occur at the maximum temperature, and conversely, which is exactly opposite the conditions at the surface of the molding compound. This situation could be of concern if the maximum humidity was on the order of the critical humidity, which would then occur at the die at higher temperatures than at the surface of the molding compound.

Now, consider the effect on the die of daily variations about the yearly response. Over a period of a few daily cycles, the water concentration at the interface with the die will change very little. However, the temperature may vary by 10 to 20^{o} C. In principal, the relative humidity H_{die} corresponding to the water concentration at the interface with the die should vary with the temperature. However, the increase in H_{die} that would result from a decrease in the saturation vapor pressure due to a decrease in temperature is almost exactly compensated for by an opposite change in the sorption coefficient, which increases as the temperature decreases.

If a flaw exists between the molding compound and the die, water vapor could accumulate in the flaw. As the temperature changes, the relative humidity in the flaw also could change. However, unless the characteristic thickness of the flaw is a significant fraction of the thickness of the molding compound (not expected), the relaxation time for diffusion of excess water vapor into the molding compound will be small relative to a daily cycle time. Any increase in H_{die} that would result from a decrease in saturation vapor pressure due to a decrease in temperature will be rapidly compensated for by an opposite change in the sorption coefficient. Based on these results, the plastic is being treated as a barrier if it behaves as a mastic and is attached firmly to the bondpad.

3.3 Integrated Model

Although we refer to the intrinsic corrosion model as being deterministic (a single response for a given set of input parameters), corrosion is certainly not a deterministic process. As such, any effective system-level model must incorporate uncertainty. Relative to wirebond corrosion (and most other types of real processes), there are four major sources or categories of uncertainty:

1. External - Environmental factors such as humidity and temperature. These parameters must be treated as time-variant distributions.
2. Internal - Materials properties, including wirebond geometry and placement, amount of intermetallic formed, crevice dimensions, physical properties, impurity distribution, and grain size and structure.
3. Physical model - Because of the simplicity of the physical model used to assess reliability, the model itself is a source of uncertainty.
4. Observational - This includes systematic and random errors associated with making measurements.

As the characterization and physical understanding of the processes improves, the uncertainty associated with categories #2 and #3 will decrease. For example, the incorporation of intermetallic distribution information along with our understanding of its

effect should reduce the scatter in the calculated rate constants for each of the eight bondpads on a specific device.

Another needed modification to the deterministic model involves the plastic-encapsulant layer. As noted in the previous subsection, this layer has little effect on moisture or heat transport. However, when a good physical bond between the plastic and the bondpad exists, it can effectively prevent any environmental interaction. Therefore, by making the justified assumption that corrosion will only occur within physical defects in the plastic, a simple addition of a defect identity function (*I*) term can be included. The identity function takes on values of either 0 or 1 that are allocated based on an assigned probability. The governing equation describing the kinetics of bondpad corrosion now has the following form:

$$\frac{d(\Delta R / R_o)}{dt} = I(defects) k_o P_{Cl_2}(t) \left\{ 1 - \exp\left[-\left(\frac{H(t)}{\eta} \right)^{\beta} \right] \right\} \exp\left[-\frac{E_a}{RT(t)} \right]$$

This equation contains five distributed parameters: I, k_o, P_{Cl2}, T and H. As indicated, three of these variables (T, H, and P_{Cl2}) are, in general, also time dependent.

The output from the corrosion model permits device and component reliability as a function of time to be determined. To illustrate this statement, consider the simple case of a device containing a single bondpad (refer to Figure 3-5). At some level of resistance increase (a "critical" resistance), the device will no long be capable of satisfying its intended function and will thus fail. A straightforward deterministic calculation would yield a service life prediction indicated by the vertical line farthest out in time. However, if uncertainty is included, a distribution of predicted resistance values is calculated at each time. The tail of each distribution that is above the critical resistance, then, represents the probability of failure (or equivalently the decrease in reliability). In this case, by the time the deterministic service life is reached, the reliability will be lowered to 50%. In high-reliability systems, risk of failure may become unacceptable when the tail of the distribution exceeds the critical resistance as shown in Figure 3-5. Very importantly, the failure criteria for every bondpad in a device will, in general, be different for each particular application. Reliability assessments must therefore be completed within the context of the electrical system that contains the wirebonds. Therefore, in general, the output from the integrated corrosion model will consist of a time-based distribution of bondpad resistance values.

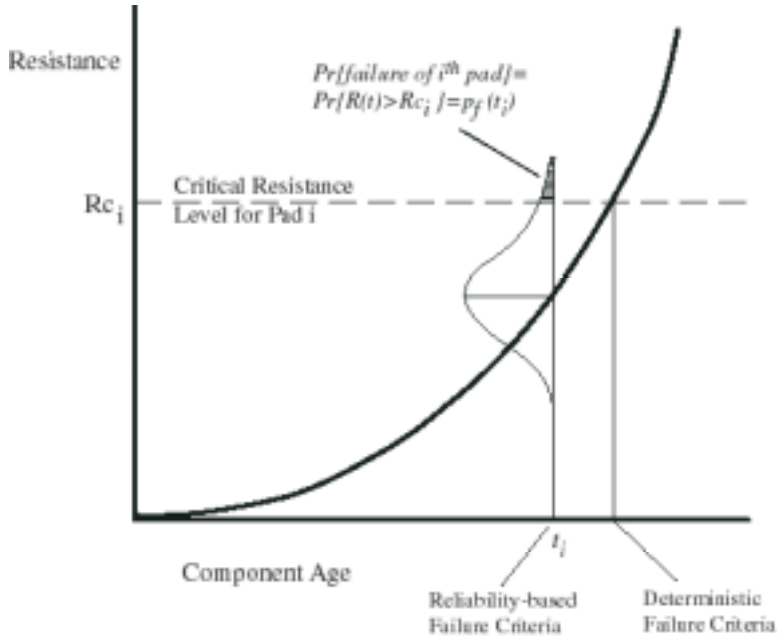

Figure 3-5. Plot of a hypothetical change in bondpad resistance to demonstrate how the existence of uncertainty permits the probability of device failure to be calculated (shaded area under the tail of the distribution).

For solving the kinetic differential equation while simultaneously addressing the variety of distributed parameters, a Sandia-developed software package called CRAX was used. The CRAX computational technique employs advanced computational reliability techniques (termed Cassandra) and directly incorporates or calls user-supplied physical models. In this study, the governing kinetic equation presented above was included. For more information on the basis and functioning of the CRAX/Cassandra package, see Appendix C and/or visit the internet site: http://reliability.sandia.gov/crax.

Performance of the actual simulations follows a relatively straightforward path. First, a value for each of the non time-based distributed parameters (e.g., rate constant) is sampled and fixed. Next, values for each of the time-based distributed parameters (temperature and humidity) are sampled for the first time step and the governing equation is numerically integrated to produce a deterministic estimate of the resistance. Then, new parametric values are sampled consistent with the time step, the equation solved, and the resistance due to corrosion accumulated with the previous time-step estimate. This process is repeated until a pre-specified length of aging has been achieved effectively yielding a simple time-based resistance response for a single device. This entire process is then repeated for a number of other devices with the actual number of simulations required being dependant on the uncertainty analysis technique being used (see Appendix C for more information). Compilation of all the responses at each time step produces the desired distribution.

4.0 Reliability Simulations

As noted above, the reason that we are studying bondpad corrosion is to enable predictions of its effect on the performance of circuit-level devices. Bondpad failure can only be defined within the context of larger electrical system. Therefore, to demonstrate the usefulness of the integrated corrosion model, two device-level simulations were performed. A description of these simulations along with the associated results is presented in the following two subsections respectively.

Both of these simulations used a common set of values for the random parameters. Also worth noting again is the use of the bondpad resistance change as a measure of the wirebond resistance change. This latter term represents the factor that actually produces the degradation in the performance of the subject device. As discussed in Section 2, a correlation between these two terms certainly exists, but the sensitivity of our test structure and measurement technique is not adequate to allow a relationship to be identified. For the distributed parameters that are not time based, the following values were used:

- At this point, all of the values derived for k_o were analyzed and found to follow an empirical log-normal distribution with mean and coefficient of variation = 1.77×10^{13} and 0.517 respectively. The mean value has the units of percent/ppb-year. As such, the units for each of the parameters in the governing equation are as follows: $[Cl_2]$ = ppb, RH = %, T=^{o}K and time=years. The integration of the equation will then output $\Delta R/R$ as a percent change.
- The chlorine concentration (P_{Cl2}) was fixed at low values that can be encountered in industrial environments (primarily motivated by lack of any applicable environmental data)
- Based on our examination of several commercial PEM devices using scanning acoustic microscopy, we estimated that the identity function (I) should have a probability that an effective defect exists over a bondpad of about 3%.

Because of the significant effect of temperature and humidity on corrosion, the simulations were performed in three dramatically different combinations of environments: nominally arctic (Fairbanks, AK), desert (Albuquerque, NM) and gulf coast (Houston, TX). Weather service data consisting of 65-year averages for the three locations were obtained (Figure 4-1). As can be seen in the figures, the data follow a very sinusoidal relationship.

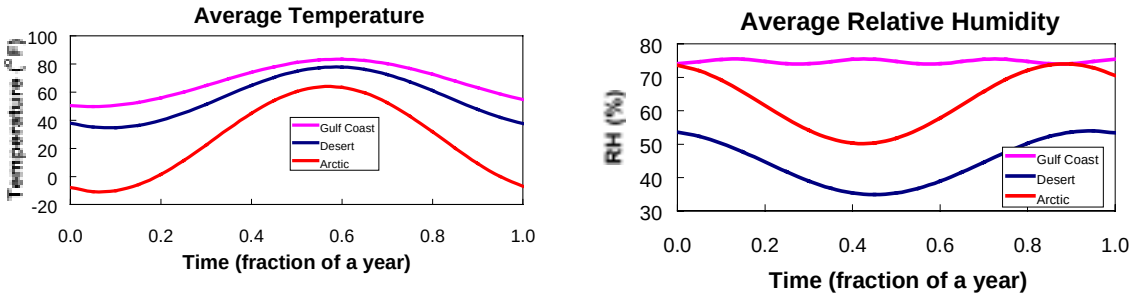

(a) (b)

Figure 4-1. Environmental data used for simulation. Data represent 65 year averages for three locations (Fairbanks, AK, Houston TX., and Albuquerque, NM.).

These data were fit to the following simple functions that contain an additional daily noise factor:

$$H(t) = \left[\mu_h + A_h \sin\left| \frac{2\pi t}{f_h} + \delta_h \right| \right] + \varepsilon_h$$

$$T(t) = \left[\mu_T + A_T \sin\left| \frac{2\pi t}{f_T} + \delta_T \right| \right] + \varepsilon_T$$

where μ_i, A_i, f_i and δ_i are deterministic parameters that describe the average monthly humidity at each specific location. The parameter ε_i is a Gaussian distributed random variable with zero mean and known coefficient of variation that captures the variability in the monthly temperature and humidity. Values for each of these parameters are shown in Tables 4-1 and 4-2.

Table 4-1. Parameters describing temperature distributions

Location	μ	A	f	δ	ε_ε
Fairbanks, AK	-3.06	20.78	1.01	4.31	12.0
Houston, TX	19.17	9.32	1.09	4.44	8.0
Albuquerque, NM	13.47	12.01	1.00	4.17	9.0

Table 4-2. Parameters describing humidity distributions

Location	μ	A	f	δ	ε_ε
Fairbanks, AK	62.10	11.92	0.92	1.83	3.0
Houston, TX	74.74	0.00	0.29	5.15	7.5
Albuquerque, NM	44.44	9.54	0.16	0.52	7.0

4.2 Single Bondpad Response

A simulation was first performed to calculate the resistance response of a single bondpad during exposure to the Albuquerque desert environment (Figure 4-1) if an industrial level of 0.01 ppb of [Cl_2] was present. The results are shown in Figure 4-2 as a cumulative distribution function. As previously stated, these data cannot be used to directly determine device-level reliability because the bondpad failure criteria are application dependent.

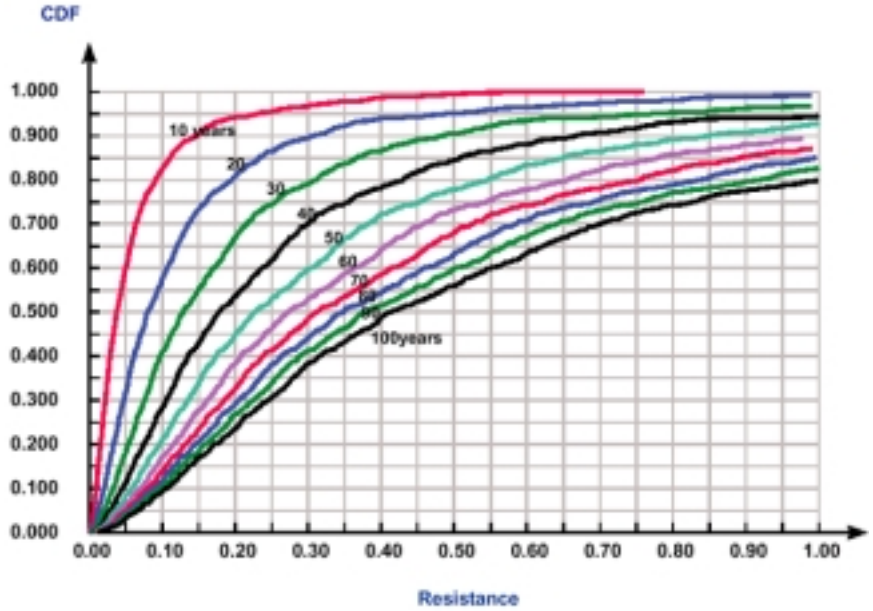

Figure 4-2. Cumulative distribution functions (CDF) of the bondpad resistance as a function of system age.

4.2 Voltage-Comparator Device

The model can also be applied to more complex electronic structures. For example, a simulation was run to model the effect of bondpad corrosion on the reliability of a voltage comparator. Figure 4-3 is a schematic diagram of the comparator, a simple electrical circuit that monitors the voltage differential between two outputs. Three transistors in the circuit are plastic parts with AuAl wirebonds. The system is required to maintain a tolerance level on the voltage difference over the operational period of the circuit, approximately 500 ms.

To permit the assessment of the impact of bondpad corrosion on the performance of the circuit, each bondpad was modeled as a resistor in series with the associated lead wire. As the comparator ages, the bondpad resistance increases according to relevant distributions of responses from the corrosion model (e.g., Figure 4-2). A model of the comparator circuit was constructed and its performance evaluated using the ChileSPICE software program being developed at Sandia. More information about this electrical-system model and its direct linkage with CRAX is contained in Appendix C (specifically Section C.4 and Figure C3). The linked ChileSPICE-CRAX/Cassandra uncertainty analysis software was then used to perform an age-aware system analysis. In this case, the single-bondpad data were generated during the simulation. Similar to the single

bondpad calculation, conditions for this simulation were as follows: [Cl_2] fixed at 0.01 ppb and temperature/humidity for the Albuquerque desert environment.

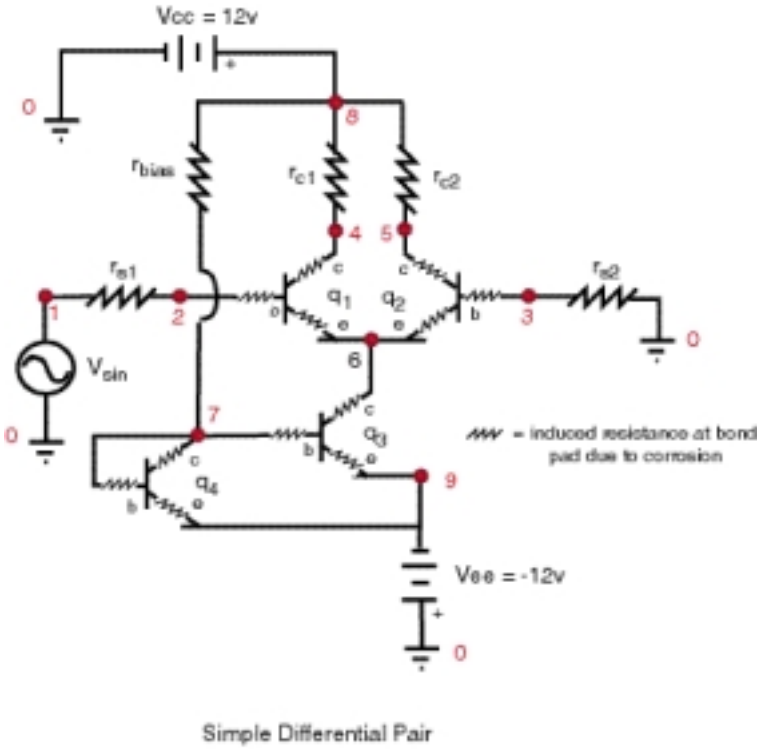

Figure 4-3. Schematic diagram of a simple voltage comparator device. Failure is determined through analysis of the entire electrical circuit.

Figure 4-4 shows how the performance of the differential pair circuit degrades with time. Each line represents the probability of the circuit performing within specifications over the 500ms operational requirement. As the system ages, the bondpads corrode, significantly impacting the performance of the circuit. After approximately 20 years, the circuit performance has degraded to the point where there is only a 90 percent chance that it will operate within the required specifications over the required operational time period. After 40 years the probability of success has dropped to approximately 85 percent. These data were replotted as a time-based reliability curve in Figure 4-5. For reference, data extracted from Figure 4-2 are also included that demonstrate that the reliability decreases with an increasing number of bondpads (assumption that the single-bondpad device fails when the resistance increases by 1%).

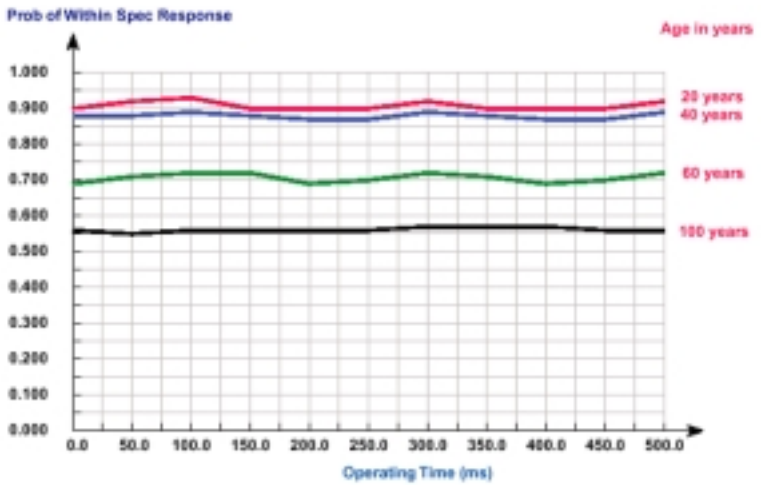

Figure 4-4. Comparator electrical system performance as a function of system age.

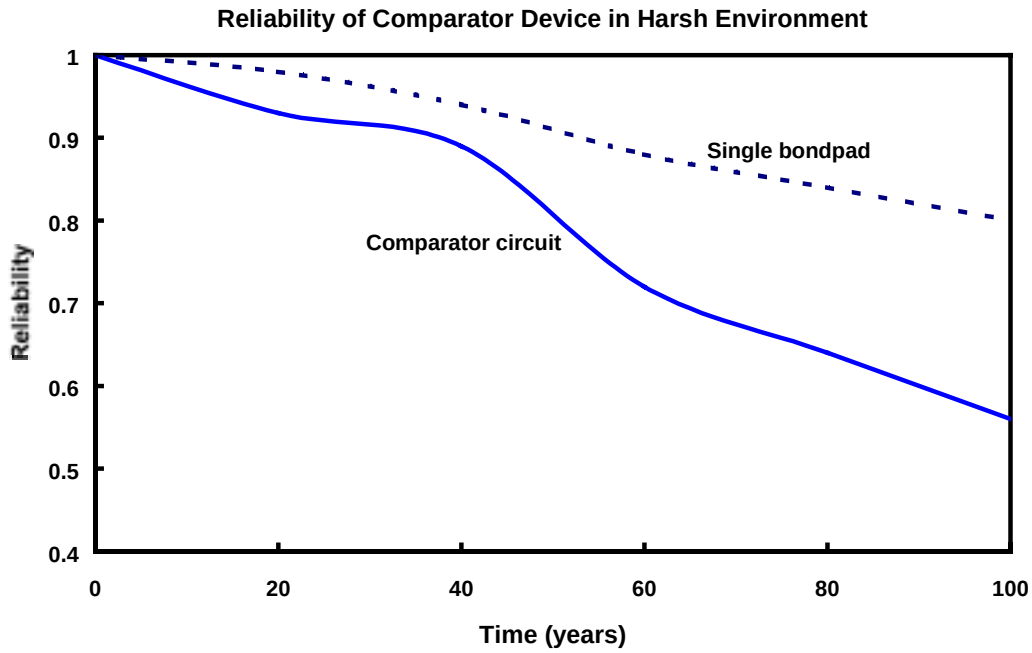

Figure 4-5. Predicted reliability of a comparator circuit and a hypothetical device with a single bondpad.

4.3 Voltage-Reference Device

A second simulation was performed to show how the storage environment can affect device reliability and how these techniques permit parametric sensitivity studies to be effectively performed. This aging simulation utilized a 3-lead LM185 voltage reference device (Figure 4-6). In this case, the bondpad failure criterion was conservatively chosen using a SPICE simulation of the LM185 device function to occur

when any of the wirebonds increased in resistance by 2%. For reference, the SPICE simulation of this very robust device determined that the resistance of the most sensitive lead must actually increase by about 1 kΩ to cause device failure. The three environments described at the beginning of this section were used. The only contaminant was chlorine gas, whose concentration was again fixed at 0.01 ppb.

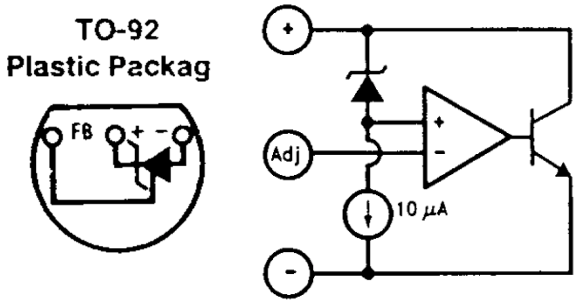

Figure 4-6. Device and schematic diagram of LM185 voltage reference device used in the second simulation.

The effect of the environment differences on device reliability is shown in the Figure 4-7a. The Gulf Coast clearly provides the most aggressive environment of the three considered. This is likely due to the relatively constant and high humidity and temperature encountered. Comparing the other two locations, an arctic exposure has a lower average temperature, but a higher relative humidity, while the desert has a higher temperature and lower humidity. The two effects countered each other and gave similar corrosion rates. One real conclusion that can already be drawn based on the time scale required to produce significant decreases is that the reliability of these devices should be quite high in any environment. In addition, informative parametric sensitivity studies were performed (Figure 4-7b) that showed how changes in environment and physical configuration can influence the calculated reliability.

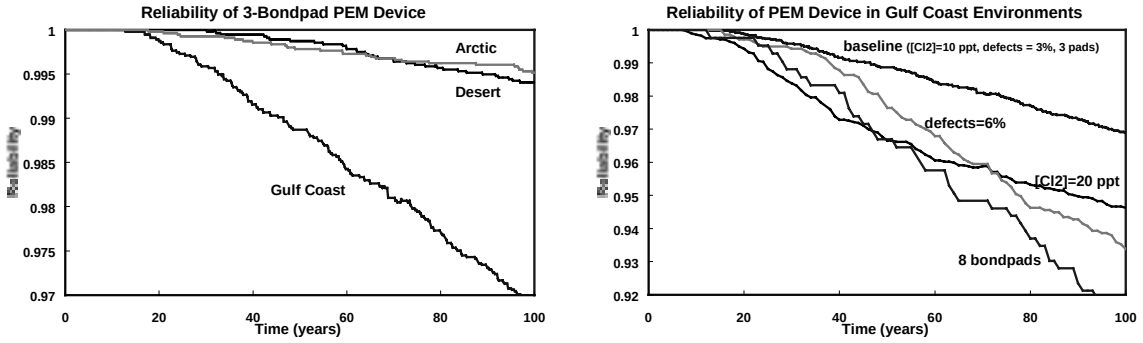

(a) (b)

Figure 4-7. Results from the aging simulation of an LM185 voltage-reference device. In (a), the effect of environment is presented, while (b) shows how variations in environmental and physical parameters can affect reliability.

5.0 SUMMARY / CONCLUSIONS

The significant technical advancements/findings that were made during this study can be summarized as follows:

1. A number of novel and effective experimental techniques were developed to quantify and characterize corrosion in microelectronic devices. These techniques are of interest and applicable to organizations both internal and external to Sandia.
2. Although aluminum corrosion in microelectronics is a very complex phenomenon involving numbers of coupled processes, we now know what factors and parameters are the most important relative to dormant storage (e.g., humidity, Al-Au intermetallics, galvanic couples, passivation and encapsulation defects). This information will be critical during the upcoming formulation of valid tests for qualifying and accepting PEM devices for use in high-consequence military systems.
3. Because of #2, development of a rigorous mathematical model to predict the expected service life for all devices under a wide range of environments and manufacturing conditions is a very difficult undertaking. Nevertheless, simplified phenomenological models, such as the one developed in this study, are still very useful tools for performing assessments of general behavior (e.g., PEM insertion) and as a basis for analyzing specific occurrences of corrosion (e.g., op amps sealed with a wide range of internal atmospheres).
4. Analytical capabilities that are truly predictive must integrate the following components: (a) mechanistic understanding of the corrosion degradation phenomena into a deterministic mathematical model, (b) uncertainty analysis to address stochastic nature of corrosion and environmental conditions, and (c) electrical system performance models.
5. The long-term reliability related to corrosion-induced failure of both PEM and CHP microelectronic parts manufactured with best-commercial practices is expected to be very good. The issue is identifying those that are not manufactured with BCP.

More specifically, a major thrust was devoted to characterizing the effect the intermetallic Au-Al compounds have on the corrosion process. This topic was identified earlier in the project as the probable cause of the apparent stochastic behavior of aluminum corrosion. Our new back-thinning/SEM technique allowed us to non-invasively examine and profile the Au-Al wirebond structure. The resulting SEM images showed a substantial variation in the quantity and type of intermetallic compounds formed that were significantly affected by various heat-treating processes. Focused ion-beam machining was then used to provide unambiguous cross-sectional and corrosion morphology information. Importantly, these data provided a qualitative correlation between the measured resistance change and the extent of corrosion. Furthermore, the stepped-resistance response suggested that parallel conductive paths existed through the wirebond. Three-dimensional intermetallic maps were formulated based on the SEM images. A 3-D electrical conductance model (based on Poisson's equation) was then

developed and used in conjunction with the maps. The modeling results predicted the stepped resistance, thus further refining our understanding of bondpad corrosion. We believe that this refinement will enable us to remove (describe) much of the observed stochastic nature of bondpad corrosion when this knowledge is incorporated into the corrosion model. Another relevant analysis was completed which showed that daily fluctuations in relative humidity are damped out by the presence of plastic encapsulant (temperature gradients are also not a factor). Finally, a numerical simulation was performed that integrated all the aspects of this project. In this analysis, the effect of corrosion on the reliability of a 4-device comparator circuit was calculated. Here, the corrosion model was directly coupled for the first time with the Chile-spice electrical system model. This integration permitted subsystem-level reliability to be directly calculated.

REFERENCES:

1. G. S. Frankel and J. W. Braithwaite, "Corrosion of Microelectronic and Magnetic Data-Storage Devices," Chapter 15 in *Corrosion Mechanisms in Theory and Practice*, 2nd edition, P. Marcus and J. Oudar, ed., Marcel Dekker, Inc., New York, 2000 (in publication).
2. M. G. Pecht, L. T. Nguyen, and E. B. Hakim, *Plastic-Encapsulated Microelectronics*, John Wiley and Sons, New York, 1995.
3. J. D. Sinclair, *J Electrochemical Soc*. Vol. 135, 1988. pp 89C.
4. G. G. Harman, *Wirebonding in Microelectronics*, McGraw Hill, New York, 1997.
5. W. H. Press, S. A. Teukolsky, W. T. Vetterling, and B.P. Flannery, *Numerical Recipes in C*, 2nd ed., Cambridge 1992.
6. C. G. Shirley, "THB Reliability Models and Life Prediction for Intermittently-Powered Non-Hermetic Components," IEEE/IRPS, 1994, pp. 72-78
7. C. G. Shirley and C. Hong, "Optimal Acceleration of Cyclic THB Tests for Plastic-Packaged Devices," in Proc. 29th Ann. Int'l Reliability Physics Symposium, pp.12-21 (1991).

ACKNOWLEDGMENTS

This work was supported by a Sandia Laboratory Directed Research and Development (LDRD) project. The direct participation and suggestions of Bonnie McKenzie with the performance of the SEM analyses and Michael Stricizh (Analytical Solutions Inc.) in the development and use of the PEM back-thinning technique is gratefully acknowledged. Sandia is operated by the United States Department of Energy under Contract DE-AC04-94AL85000. Sandia is a multi-program laboratory operated by Sandia Corporation, a Lockheed Martin Company, for the United States Department of Energy.

APPENDIX A: Description of Experiment Configuration, Specific Exposure and Analysis Procedures, and Test Device

A1. Matrix of Corrosion Characterization Experiments

During the course of this study, a wide range of experiments was performed to measure corrosion kinetics using the ATC02.6 test device (refer to Section A3 for more information on this device). The primary variables that were studied included contaminant (gaseous and solid), relative humidity, temperature, heat-treatment (extent of intermetallics), and presence of encapsulant. A summary of the test matrix is shown in Table A1. In this table, the "heat-treatment time" is the time at which each device was held at 175^{o}C in an inert atmosphere (to simulate encapsulant cure cycle), the "number failed" indicates how many of the bondpads were open circuit at the end of the exposure (with total number of measurable bondpads given second), the first "linear rate" is the averaged slope of the initial linear portion of the resistance-rise response (usually taken to a maximum of 10%), and the latter "linear rate" is the standard deviation of the rate values.

These experiments were performed sequentially in several series. Each series had either a major modification of the previous procedures or a different objective:

A. General procedure development for solid-phase contamination (applicable to contamination during manufacture - results not used or shown in Table A1)
B. Procedure development for gaseous contamination (results not used or shown in Table A1 because ATC devices were fabricated with poor quality wirebonds
C. First investigation of environmental parameter space using gaseous contamination and without heat-treatment being considered (periodic resistance measurements performed)
D. Repeat of Series C except heat-treatment considered (periodic resistance measurements performed)
E. Subset of Series D with a glob-encapsulant being applied into the ATC cavity under two cleaning conditions (periodic resistance measurement)
F. Repeat of Series D with a new procedure implemented to continuously monitor resistance changes
G. First characterization of the effect of manufacturing contamination
H. First characterization of the effect of atmospheric particulate contamination.

As noted in the previous list, an important procedural change was implemented about halfway through the project. Initially, the ATC test devices were exposed to the environmental conditions in a well-stirred atmospheric chamber. Periodically (nominally weekly), the devices were removed and the resistance of each bondpad set measured using an external automated apparatus. Motivated by the increased variability of the results obtained during Series D when the heat-treatment conditioning process was

implemented and ongoing corrosion of the ATC leads, a new procedure was developed that allowed continuous exposure of just the bondpad area and frequent measurement of resistance (for more information on these procedures, refer to Section A3).

A2. Atmospheric Exposure and Data Acquisition

A2.1. Contamination environments – gas and solid

Three techniques were used to simulate the types of contaminants to which PEM IC dies can be exposed. The first procedure, applicable to industrial environments, consisted of exposing test structures to a humidified, constant flow of air containing a small level of a relevant gas-phase contaminant (e.g., Cl_2, Br_2, chlorotoluene). The majority of the characterizations that were performed in this project used a Cl_2 gas contaminant. The source of the gas was a permeation tube that produced the contaminant at a constant rate. Air flowing above the permeation tube picked up the contaminant and was mixed with dry and water saturated air streams to provide ppb to ppm levels of the contaminant. This system allowed us to independently control the humidity and contaminant concentration.

In the second procedure, which simulated contamination during manufacture, NaCl was dissolved in methanol and uniformly sprayed across the die surface. The alcohol evaporated quickly, leaving a layer of solid NaCl on the surface. Aging was then performed in a constant humidity/temperature chamber. A third technique used to reproduce the effects of atmospheric particulate contamination involved depositing simulated dust particles directly on the surface. Compounds typically found in airborne dust particles (i.e., NH_4HSO_4, $NaHCO_3$, KCl, $(NH_4)_2SO_4$) were ground in a mortar and pestle.[A1] To accurately represent reality, the dust should contain particles that are less than 1 μm in diameter. After grinding, the dust was deposited using a air brush to "sand blast" the surface with the dust. Figure A1 shows the distribution of particles obtained through this technique. Two arbitrary levels were applied in Series-H exposures.

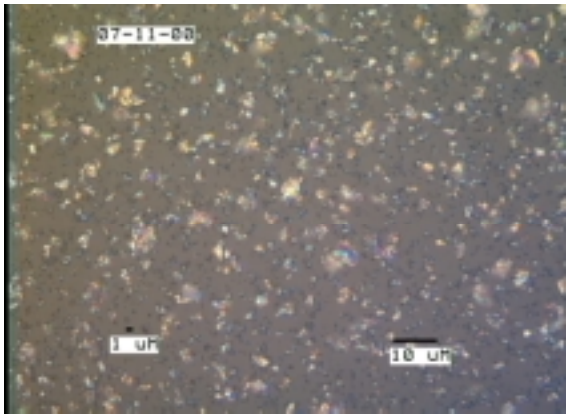

Figure A1. Photomicrograph of dust particles deposited on a glass slide.

Table A1. Compilation of the experimental corrosion-testing matrix, including some selected results.

Series	PEM #	Contaminant species	Contaminant level (ppb)	RH (%)	Temp (°C)	Heat treatment time (hrs)	Test duration (days)	# Failed	Linear rate (ave - %/day)	Linear rate (std dev)
SERIES C: initial gaseous contamination and periodic measurement (no HT)										
	206	Cl_2	10	70	32	0	92	0/8	0.111	0.049
	248	Cl_2	500	16	40	"	15	0/8	0.503	0.195
	249	Cl_2	2000	16	40	"	15	8/8	0.732	0.347
	250	Cl_2	2000	16	25	"	34	8/8	0.868	0.274
	251	"	"	16	"	"	34	4/8	0.897	0.466
	252	Cl_2	500	16	25	"	25	7/8	1.167	0.659
	253	"	"	16	"	"	25	7/8	2.164	1.46
	254	Cl_2	2000	5.5	25	"	25	3/8	0.176	0.105
	255	"	"	5.5	"	"	25	2/8	0.176	0.061
SERIES D: gaseous contamination and periodic measurement										
	Controls - Stored in nitrogen dessicator									
	266	na	na	na	Na	3	33	0/8	na	na
	274	"	"	"	"	"	"	0/8	"	"
	Baseline Conditions									
	259	Cl_2	200	85	40	3	13	3/8	0.44	0.21
	260	"	"	"	"	"	13	6/8	0.46	0.50
	Low humidity									
	261	Cl_2	200	30	40	3	81	0/7	0.02	0.01
	267	"	"	"	"	"	61	6/8	0.04	0.02
	High [Cl_2]									
	262	Cl_2	800	85	40	3	6	8/8	9.13	8.76
	263	"	"	"	"	"	6	8	17.4	8.60
	Low [Cl_2]									
	268	Cl_2	20	85	40	3	29	2/8	0.14	0.08
	269	"	"	"	"	"	47	6/8	0.11	0.06
	Heat Treatment									
	270	Cl_2	200	85	40	3	6	5/8	0.26	0.29
	275	"	"	"	"	none	27	5/8	0.11	0.09
	276	"	"	"	"	"	6	6/8	1.40	1.28
	277	"	"	"	"	24	6	6/8	3.97	1.66
	278	"	"	"	"	"	9	2/8	0.24	0.36

Table A1 (continued)

Series	PEM #	Contaminant species	Contaminant level (ppb)	RH (%)	Temp (°C)	Heat treatment time (hrs)	Test duration (days)	# Failed	Linear rate (ave - %/day)	Linear rate (std dev)
SERIES D (continued)										
	Baseline [Cl_2] - Std HT									
	271	Cl_2	200	85	40	3	20	8/8	—	—
	280	"	"	"	"	"	33	8/8	—	—
	Lower [Cl_2] - Std HT – replication									
	272	Cl_2	100	85	40	3	26	8/8	—	—
	283		"	"	"	24	20	8/8	—	—
	273		"	"	"	3	33	7/8	—	—
	284		"	"	"	24	15	6/8	—	—
	Lower [Cl_2] - no HT									
	281	Cl_2	100	85	40	none	15	1/8	—	—
	282		"	"	"	none	15	4/8	—	—
SERIES F: gaseous contamination and continuous measurement										
	Baseline Conditions									
	326	Cl_2	100	70	24	3	2	0/8	1.81	2.00
	333		"	"	"	"	8	7/8	3.46	1.43
	334		"	"	"	"	4	0/8	2.17	0.53
	50% RH									
	336	Cl_2	100	50	24	3	21	7/8	0.68	0.38
	339		"	"	"	"	21	8/8	1.80	0.75
	30% RH									
	335	Cl_2	100	30	24	3	11	0/8	0.46	0.46
	337		"	"	"	"	11	0/8	0.04	0.04
	Mid [Cl_2]									
	340	Cl_2	50	70	24	3	16	5/5	3.38	0.84
	341		"	"	"	"	17	5/7	1.24	0.75
	Low [Cl_2]									
	324	Cl_2	10	70	24	3	21	2/8	0.04	0.02
	325		"	"	"	"	21	0/7	0.08	0.05
	60% RH									
	342	Cl_2	50	60	24	3	16	5/8	0.52	0.33
	343		"	"	"	"	16	3/8	0.20	0.07

Table A1 (continued)

Series	PEM #	Contaminant species	Contaminant level (ppb)	RH (%)	Temp (°C)	Heat treatment time (hrs)	Test duration (days)	# Failed	Linear rate (ave - %/day)	Linear rate (std dev)
SERIES F (continued)										
	no HT									
	345	Cl_2	100	70	24	none	1	0/7	11.15	6.88
	346	"	"	"	"	"	7	1/7	3.28	2.16
	347	"	"	"	"	"	14	6/6	12.6	3.4
	high HT									
	330	Cl_2	100	70	24	24	7	4/6	7.95	3.35
	348	"	"	"	"	"	13	7/7	5.10	2.50
	alternate gaseous contamination									
	355	Br_2	50	70	24	3	7	6/6	—	—
	357	Br_2	10	"	"	"	21	6/6	—	—
	358	Br_2	3	"	"	"	7	1/8	—	—
	359	Br_2	“	30	"	"	38	7/8	—	—
	356	Chloro-toluene	50	70	"	"	24	0/8	—	—
SERIES E: glob epoxy encapsulation										
	encapsulated as received									
	291	Cl_2	20	85	40	3	41	0	—	—
	292	"	200	"	"	"	61	?	—	—
	cleaned prior to encapsulation									
	286	Cl_2	200	85	40	3	61	?	—	—
	287	"	20	"	"	"	41	0	—	—
SERIES G: solid contamination with continuous monitoring										
	manufacturing									
	351	NaCl	0.1 M	70	24	3	3	8/8	—	—
	352	"	"	"	"	"	3	8/8	—	—
	353	NaCl	0.01 M	70	24	3	28	1/8	—	—
	354	"	"	"	"	"	28	1/8	—	—
	atmospheric particulate									
	393	mixed salt	“heavy”	80	24	3	34	0/8	—	—
	396	"	"	50	"	"	33	0/8	—	—
	395	"	“light”	80	24	3	34	0/8	—	—
	394	"	"	50	"	"	33	0/8	—	—

A2.2. Gas exposure system and data acquisition

To help ensure a constant contaminant level in the adsorbed water layer ($[Cl_2] \cong k_H P_{Cl2}$), the majority of the characterization tests performed in this project used the gas-phase contaminant option. During Series B through E, the subject ATC devices were placed in a well-stirred lidded jar and exposed to the contaminant-containing atmosphere. As noted in Section A1, the exposures were periodically interrupted and the devices removed from the chamber to allow off-line automated resistance measurements. Starting with Series F, a new procedure was developed and implemented primarily to permit uninterrupted exposure, faster measurement frequency, and isolation of the 40-pin dip package from the environment. Much of the hardware used in this procedure is shown in Figure A2. The environmental cell (Figure A2(c)) that was attached to the top-side of the test devices allowed only the center die portion to be exposed. Thus, the package leads and mating sockets were not exposed to the corrosive gas. Resistance measurements were frequently made (~ every 10 minutes) throughout the test. A ribbon cable was used to connect the printed wiring board to a scanner and micro-ohm meter. The meter was wired to utilize the 4-point resistance measurements fabricated into the ATC devices.

A3. Microelectronic corrosion-test device

The ATC02.6 test chip was developed under a previous Sandia LDRD project entitled “High Reliability Plastic Packaging for Microelectronics”.[A2] Experiments with the ATC02.6 are described in a report by Johnson et. al and in a recent paper by Tracy et. al.[A3,A4] This test chip was designed for use in experiments in which corrosion of metal conductors on an integrated circuit (IC) might occur as a result of environmental conditions at the die surface. The chip is passive in that it contains no active transistor elements, only Al and polysilicon (poly-Si) conductors and oxide insulators. A micrograph of the ATC02.6 is shown in Figure A3.

The triple-track corrosion structures are interdigitated or serpentine Al metal tracks that can be electrically biased to any level suitable for an experiment. In this way, very large electric fields may be established to accelerate electrochemical corrosion. A schematic diagram of a triple track structure is shown in Figure A4. Typically, the outer and inner tracks are biased positively with respect to the center track. All electric fields are internal to the track structure, preventing interaction with other nearby structures.

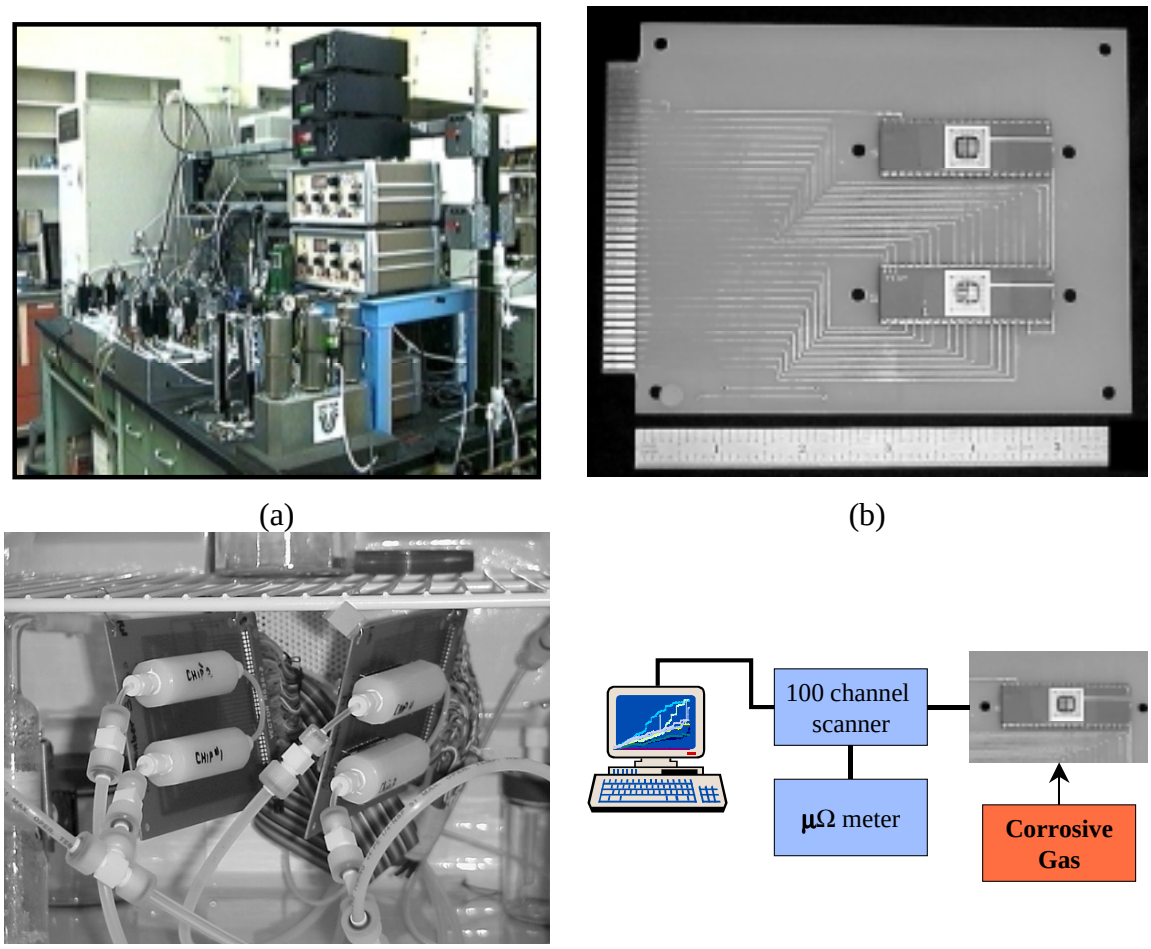

Figure A2. System and techniques used to expose ATC test devices to corrosive atmospheres and monitor resulting changes in resistance: (a) computer-controlled gas handling apparatus to produce humid mixed flowing gas, (b) mounting of test devices to printed wiring board, (c) the environmental-flow chamber attached with a hermetic seal to the top of each device (4 total in this picture), and (d) schematic diagram of hardware used to measure resistance.

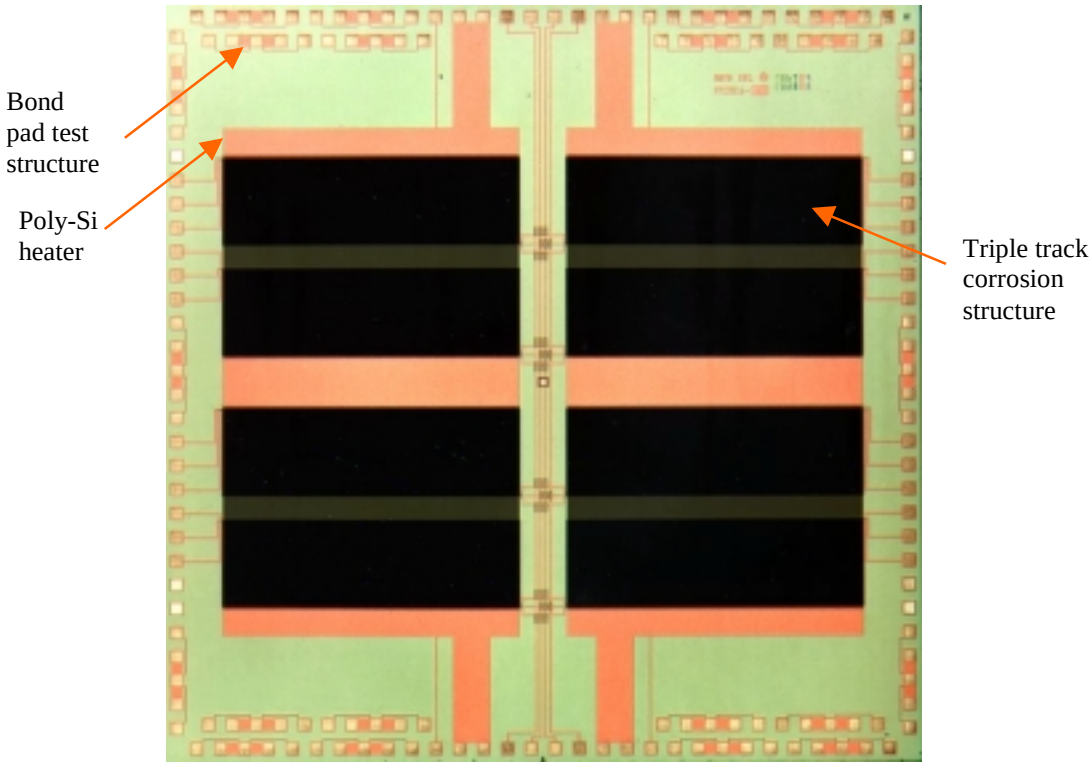

Figure A3. Photomicrograph of the ATC02.6. The various features on the die are indicated.

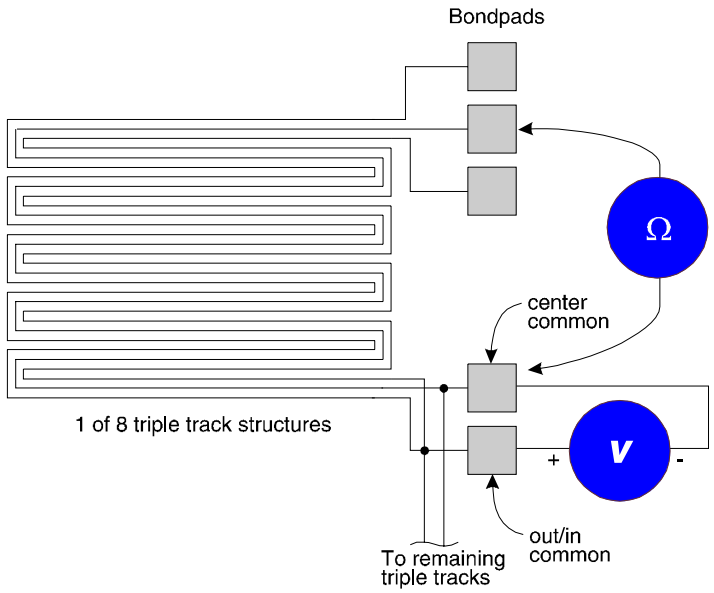

Figure A4. Schematic diagram of triple track structure consisting of three interdigitated tracks, with the outer tracks typically biased anodically with respect to the center (cathodic) track. Track corrosion is detected by measurement of the track resistances, normally with the bias removed.

Corrosion can occur either in the track field or at the wire bond on the bond pad. The track field is covered with a passivation coating, usually SiN, with possibly a CVD glass underlayer. The bond pad region is not passivated in order to facilitate the wire bond operation. In either case, track or bond pad corrosion, a measurable change in resistance cannot be observed until very near the failure point at which a track opens. Hence, the track structure is not too well suited for studies of the kinetic nature of the corrosion process.

In the work reported in this study, most of the emphasis was placed on corrosion of the Au wire to Al bond pad joint, because this was the main corrosion related failure mode observed in early experiments and more modern PEM devices (primarily because of the effectiveness of the passivation layers). The studies described made use of the bond pad test structure indicated in Figure A3.

A schematic drawing of an Au wire bond to an Al pad on an IC is shown in Figure A5. The ball bond on the die bond pad is formed by application of heat, pressure, and sometimes ultrasonic scrubbing. A reaction zone forms at the bond interface and this zone can grow under the influence of high temperature and high moisture levels. As the bond ages under the joint influence of high temperature and humidity, the reaction zone grows along with the growth of potential void regions.

Ideally, it would be desirable to measure the resistance of just the reaction zone shown in Figure A5. However, in an actual measurement there is extraneous series resistance from the wire and the pad that makes it difficult to determine the small change in resistance due to reaction zone formation. This change may be only a few mΩ, while the series resistance is in the range ≈ 100-500 mΩ. Blish and Parbek described a method of making an approximate measurement.[A5] They used a chip with a sheet of Al metal and connections that required multiple bonds to leadframe contact fingers. They determined that a resistance change ~ 20 mΩ corresponded to significant losses of both pull and shear strength. Although their design appears to have worked well, we desired to have a test structure which could be conventionally bonded so that wire bond assembly could be performed just as it is in actual practice, with one wire per leadframe finger.

Instead of measuring the resistance to current flow through the bond under study, as shown in Figure A5, we decided to measure the resistance to current flow through the bond region in a lateral sense or direction. Such a circuit is shown conceptually in Figure A6. With no bond present, current flows uniformly through the pad, as shown by the top left diagram. After bonding, current shunts through the Au ball, resulting in a resistance decrease from the bare pad condition (top left diagram and bottom right diagrams). After reaction zone formation, the resistance will increase as the current shunting through the Au ball is inhibited by the presence of a high resistivity reaction zone (bottom right diagram).

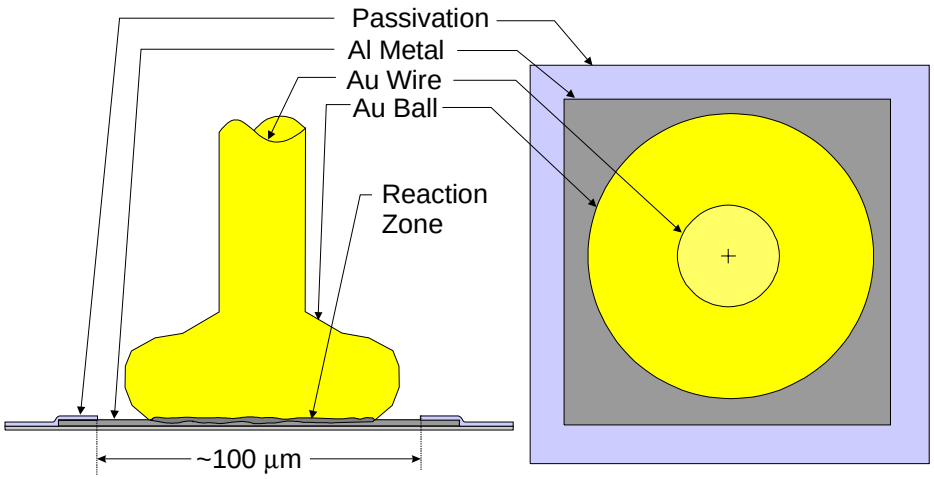

Figure A5. Au wire bond on an Al bond pad showing a conceptual picture of a reaction zone under the bond. A reaction zone can form under the influence of temperature alone or under the joint influences of temperature and moisture (humidity).

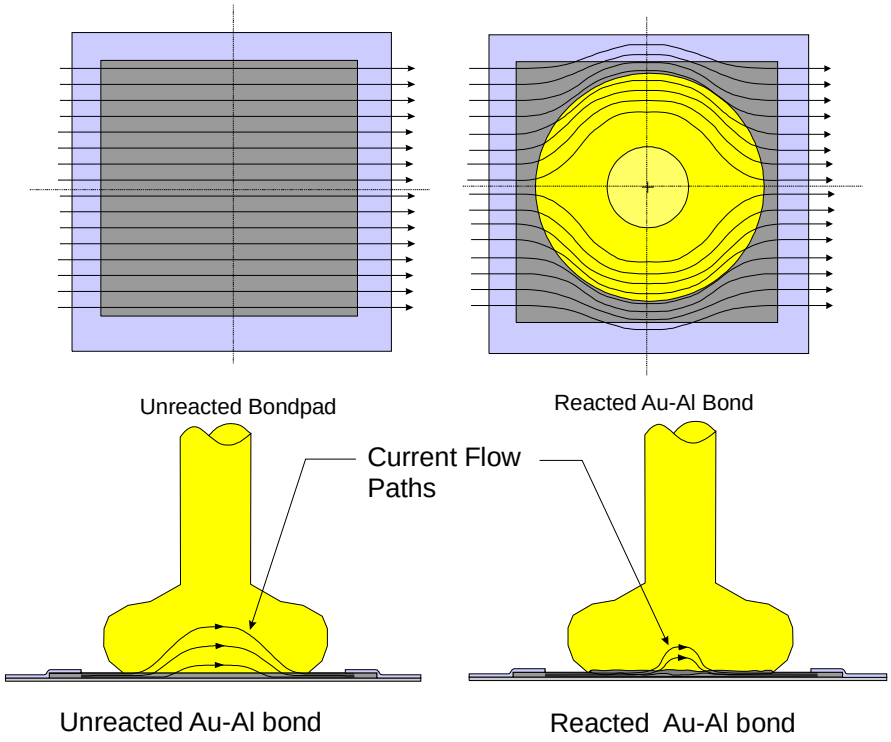

Figure A6. Conceptual transverse bond resistance structure. Prior to bonding (unreacted bond pad), the current flows uniformly through the Al bond pad sheet. After bonding, some of the current is shunted through the Au ball, resulting in a lowering of the transverse resistance. If a high resistance reaction zone forms, the resistance then increases as current is shunted away from the high resistance reaction zone region.

A schematic diagram of a bond pad resistance test structure is shown in Figure A7. In the diagram on the left, we show the instrumentation for measurement of the transverse resistance. A known current is passed transversely through the bond pad by a current source connected to the two pads adjacent to the bond under test (BUT, central bond). The voltage drop across the pad is measured with a voltmeter connected across the outer set of bonds. This resistance is calculated as the voltage drop divided by the current. In this way, none of the wire or package to socket resistances affect the measurement of the transverse resistance.

The circuit on the right can be used to measure the resistance to current flow through the bond in the usual direction. However, this resistance includes the resistance of the wire to the BUT and also the external package to socket connection to the associated package pin. This geometry was not used in the measurements described in this report.

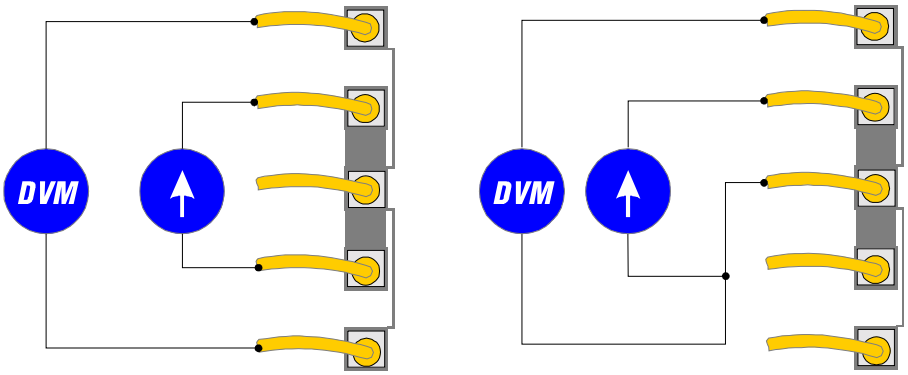

Figure A7. One of 22 bond pad resistance structures showing typical measurement connection for 4-point interfacial resistance of the center bond wire/bond pad (left) and 3-point measurement of the center bond wire continuity (right).

The major question in this type of measurement is how the measured change in transverse resistance ΔR_t relates to a change in bond strength because this strength is the critical factor in determining whether a bond could fail in a thermal cycling or thermal shock environment. A result reported in Ref. A2 and Ref. A3 is shown in Figure A. In the experiment summarized by this graph, The transverse resistance was measured for 572 bond resistance structures on ATC02.6 die packaged in plastic quad flat packs (PQFP). Periodically during the test, some PQFP parts were removed the test and the encapsulant was removed from these parts by an etching process. After encapsulant removal, the bond strength was measured either by a pull or a shear test. The graph in Figure A shows that the increase in transverse resistance ΔR_t correlates well with a decrease in bond strength as measured by either the pull or shear technique. The initial transverse resistance was $\approx 20\ m\Omega$ and in this test it increased to $> 40\ m\Omega$. The standard deviation associated with the resistance measurement is very small relative to the average so it is not shown.

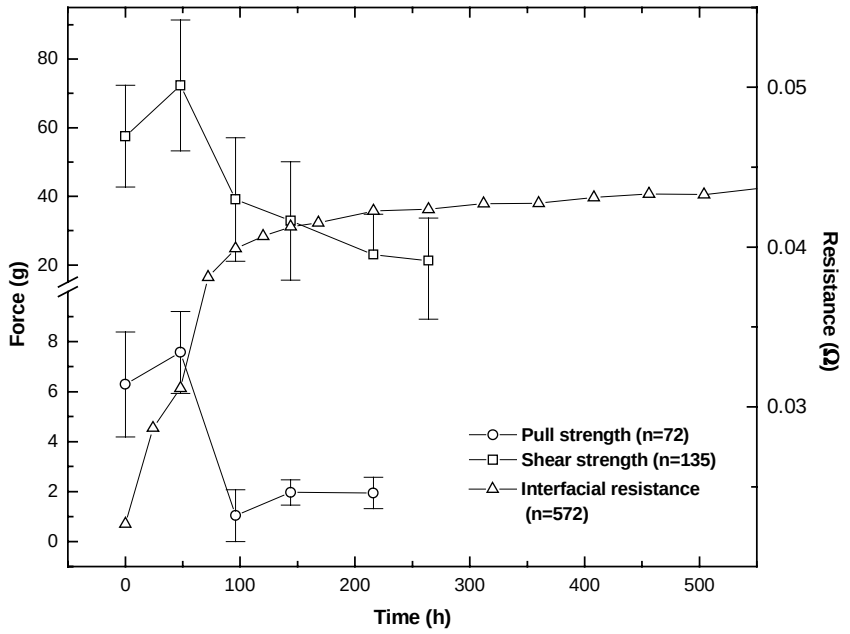

Figure A8. ATC2.6 average interfacial bond resistance (triangle, right ordinate) as a function of time during 200°C aging for test structures assembled in 160 lead PQFP packages using Sumitomo 6300HJ epoxy novolac molding compound. First 500 h of 1152 h experiment are shown. Overlaid are average bond shear strength (square) and pull strength (circle) data in grams on left ordinate vs. time. Error bars represent one sigma standard deviation.

The ATC02.6 transverse resistance measurement can be used to show the effect of temperature and humidity on the bond reaction zone growth. High temperature storage (HTS) experiments are typically performed under low humidity conditions at temperatures in the range 150-200 °C. In contrast, temperature humidity bias (THB) tests are performed at lower temperatures, typically in the range 85-140 °C, and at 85% relative humidity. In the HTS case, only Au-Al intermetallic formation occurs, while in the THB case, corrosion products can form as well.

Results from three tests with plastic packaged parts under different conditions are shown in Figure A9. The 175 and 200°C tests were performed under dry conditions and are typical of HTS test conditions. The 140°C test was performed in an 85% relative humidity environment. In the 200°C case, a large number of failures had occurred by 100 h so the test was terminated at that point. These data show how the presence of moisture can significantly increase the rate of bond degradation.

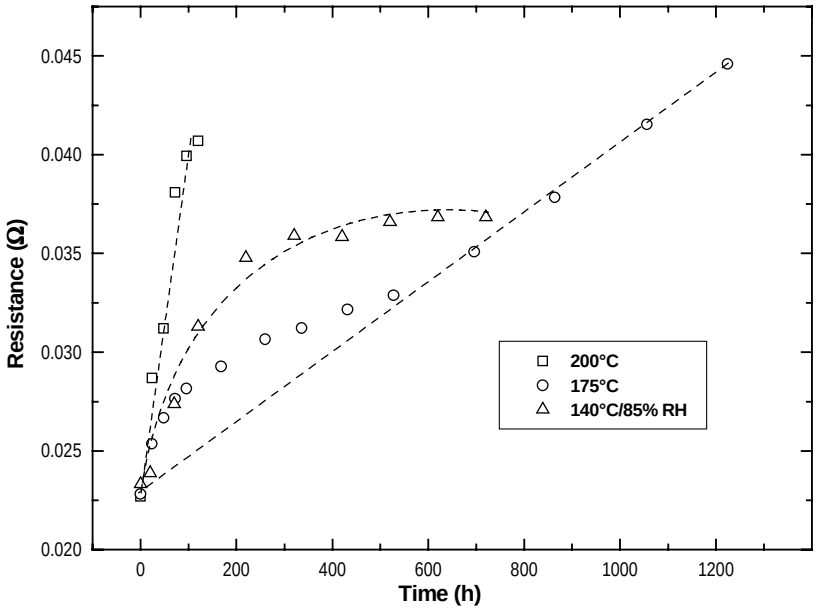

Figure A9. Transverse bond resistance averages as a function of time and accelerated temperature/humidity conditions of ATC2.6 test chips packaged in 160 lead PQFPs using Sumitomo 6300HJ molding compound. The 175 and 200°C tests were performed under dry conditions.

A4. Techniques to directly observe corrosion behavior in microelectronic test device

A4.1. Backthinning procedure to expose bondpad

Due to the presence of the wirebond, it is difficult if not impossible to image the bond microstructure from the top side of the Al metallization. A technique was then developed that consists of a non-invasive process (relative to the Al metallization layer) to remove the die sub-structure from the backside of the bondpad. If the die is not encapsulated (as with the ATC device) the package cavity is filled with 0.3-micron glass beads and the entire package assembly is then potted with low shrinkage epoxy. The die portion is sectioned out and majority of the die structure is mechanically removed by lapping to a thickness of approximately 25 microns. A final mechanical polish removes lapping striations from the backside of the die, and produces a flat, uniform surface. At this point, the surface consists of a layer of silicon on top of SiO_2 with the metal traces below the SiO_2 layer. The final removal of the silicon is accomplished using a dry plasma etch (CF_4) process, which required up to 10 hours of etch time. This process removes only the Si, leaving the SiO_2 untouched. After complete removal of the silicon substrate, a wet buffered oxide etch is used to remove the SiO_2 layer and directly expose the metal traces. The buffered oxide etch is designed to attack the oxide (SiO_2), leaving the Al

metal. At this point, the surface of the sample is the bottom of the Al traces, making it possible to directly view the bondpad.

A4.2. Depth-sensitive profiling using SEM analysis

Once the backside of the bondpads was exposed, the SEM was used to characterize the microstructure of the wire bonds. The electron penetration depth is a function of the microscope accelerating voltage. Higher energy electrons penetrate more deeply into a sample. Thus, higher accelerating voltages will result in images that contain information from regions further below the sample surface. The penetration depth also decreases with increasing atomic number of the sample. Thus for a given accelerating voltage, the image will contain information from further below the surface in Al than it will for Au. At 1 kV the information depth for Al is about 0.01 μm and for Au the information depth is 0.002 μm. At 30 kV the information depths increase to 2.5 μm for Al and 0.5 μm for Au. A series of images at a wide range of accelerating voltages were collected from the exposed bond pads. These images permit the three dimensional structure of the wirebond to be better understood.

Electron backscattering diffraction (EBSD) has become a standard technique for the identification of crystalline phases in the SEM. EBSD was used to determine the identification of the AU/Al intermetallic that was in direct contact with the Al in the bond pad. The backthinned samples were ideal for this determination.

A4.3. Focussed-ion beam (FIB) sectioning

The disadvantage of plan view SEM imaging of the bond pads is that it is difficult to accurately measure the depth of a given feature below the sample surface. Cross sections of the bond pads must be prepared in order to obtain accurate depth information from the bondpads. Mechanical polishing techniques were tried, but were unsuccessful due to the small size of the features and the relative softness of the bond pads that lead to smearing of the sample during polishing. The smearing of the sample obscures the details of the bond pad microstructure. The FIB milling provides a way to avoid mechanical polishing and still produce cross sections that contain the microstructural details of interest. The FIB instrument uses a beam of 30 kV Ga^+ ions. The ions are focussed into a small spot that is then rastered over the sample. The Ga^+ ions can sputter or remove material from the sample. Using an appropriate scanning pattern, deep trenches may be milled into the surface of the sample. The resulting trench can then be imaged at a high tilt in a standard SEM and the cross section of the bondpad and wire bond examined. In the examples shown here a two step procedure was used. First, a ramp or stairstep was cut into the sample so that the cross section could be viewed when the sample was tilted. Following the stair step, the face of the cross section was polished with a smaller lower current ion beam. This technique produced excellent cross sections of the sample.

Ions may also be used to produce images in a similar manner to forming images in the SEM. Ions can produce images in which the contrast is a function of the crystallographic orientation of various regions in the sample. This contrast mechanism

can be exploited when polycrystalline samples are imaged. The main disadvantage of this technique is that the Ga^+ ions are continually modifying the surface of the sample while the images are collected due to sputtering of the surface.

References – Appendix A

A1. J. D. Sinclair, "Indoor Atmospheres," *ASTM Manual 20: Corrosion Tests and Standards Manual, R Baboian, ed*, ASTM, 1995, pp. 295-306.

A2. J. N. Sweet, D. W. Peterson, A. H. Hsia, M. Tuck, "High Reliability Packaging for Microelectronics", Sandia National Laboratories Report, SAND97-1721, July 1997.

A3. D. R. Johnson, D. W. Palmer, D. W. Peterson, D. S. Shen, J. N. Sweet, J. T. Hanlon, K. A. Peterson, "Microelectronics Plastic Molded Packaging", Sandia National Laboratories Report, SAND97-0162, May 1997.

A4. D. Tracy, L. Nguyen, R. Giberti, A. Gallo, C. Bischof, J. N. Sweet, A. Hsia, "Reliability of Aluminum-Nitride Filled Mold Compound, *Proc. 47th Electronics Component and Technology Conf.*, IEEE, 1997, pp. 72-77.

A5. R. C. Blish II, L. Parobek, "Wire Bond Integrity Test Chip", *Proceedings of the 21st Annual Reliability Physics Symposium*, IEEE, 1983, pp. 142-147.

APPENDIX B: Mathematical Analysis of Thermal and Moisture Transport through Plastic Encapsulant

This appendix provides a description of the mathematical analysis that was performed to determine the importance of heat and moisture transport through the plastic encapsulant. A summary of the findings from this analysis is contained in the body of report (Section 3.2). This study identifies the relationship of heat and mass transfer to the moisture exposure of a die covered by a thin layer of molding compound that is exposed to periodic variations in the ambient temperature T_{amb} and relative humidity H_{amb}. For purposes of illustration, the periodic variations in relative humidity are assumed such that the moisture concentration in the molding compound at the free surface sinusoidally varies (consistent with normal daily and annual variations). The analyses follow the approach of previous authors[B1,B2] who have treated moisture transport in plastic packaged devices as one-dimensional diffusion. Heat transfer in the molding compound is considered first, then moisture transport is examined.

B1. Heat Transfer

One-dimensional heat transfer in the molding compound is described by the heat conduction equation

$$\frac{\partial T}{\partial t} = \alpha \frac{\partial^2 T}{\partial x^2} \tag{1}$$

where T denotes the temperature in the molding compound; t denotes time; x is the spatial coordinate, and the thermal diffusivity α is given by

$$\alpha = \frac{k}{\rho c} \tag{2}$$

where k is the thermal conductivity; ρ is the mass density, and c is the specific heat of the molding compound. Let the ambient temperature T_{amb} vary sinusoidally with time t. Denote the maximum temperature by T_{max}, and the minimum temperature by T_{min}. Let

$$T_{amb} = T_{ave} + \tilde{T}_{amb} \tag{3}$$

where $\tilde{T}$ is the sinusoidal variation in temperature about the average temperature T_{ave}. Let

$$\tilde{T}_{amb} = \tilde{T}_{max} \sin\left(\omega t + \varepsilon\right) \tag{4}$$

where

$$\tilde{T}_{max} = T_{max} - T_{ave} = T_{ave} - T_{min} \tag{5}$$

$$T_{ave} = \frac{T_{max} + T_{min}}{2} \tag{6}$$

$$\omega = \frac{2\pi}{t_c} \tag{7}$$

and t_c is the time for one sinusoidal cycle in temperature. Let the molding compound form a thin sheet of thickness 2*l*, which is on the order of 0.10 to 0.13 cm. Let $x = \pm l$ denote the surfaces of the molding compound adjacent to the ambient atmosphere and die. For purposes of examining the effects of periodic variations in the ambient temperature, assume that the same periodic variation occurs at each surface of the molding compound, or

$$T(l,t) = \tilde{T}_{max} \sin(\omega t + \varepsilon) = T(-l,t) \tag{8}$$

Assume that the initial temperature in the molding compound is uniform and given by

$$T(x,0) = T_{ave} \tag{9}$$

Also, assume that the thermal properties of the molding compound have values between those typical for an epoxy polymer and those for silicon dioxide, values for which are given in the Table B-1 below for temperatures on the order of 25° C.

Table B-1. Thermal Properties for Various Compounds

Constituent	Density ρ (g/cm^3)	Specific Heat c (cal/g °C)	Thermal Cond. *k* (cal/s cm °C))	Thermal diff. α (cm^2/s)
Silicon Dioxide[B3]	2.65	0.18 – 0.20	3.0 – 3.3x10^{-3}	~5.6 – 6.9x10^{-3}
Epoxy Polymer[B4]	---	---	---	~1.0 – 1.3x10^{-3}

The cycle times of interest are either a daily (one-day) cycle or a yearly (365-day) cycle of. Because the characteristic thermal diffusion time given by

$$t_\alpha = \frac{l^2}{\alpha} \tag{10}$$

is very small (on the order of 5x10^{-5} day or less) relative to a cycle time of one day, the temperature of the molding compound should be essentially uniform and equal to the ambient temperature. This can be shown in more detail by considering the solution to the heat conduction equation subject to the boundary and initial conditions given by Eqs. 8 and 9. If the thermal properties of the molding compound do not vary appreciably over the temperature ranges of interest, then the temperature distribution in the molding compound is given by[B5]

$$\frac{\tilde{T}}{\tilde{T}_{max}} = A\sin(\omega t + \varepsilon + \phi) + 4\pi\alpha \sum_{n=0}^{\infty} \frac{(-1)^n (2n+1)\left[4l^2\omega\cos\varepsilon - \alpha(2n+1)^2\pi^2\sin\varepsilon\right]}{16l^4\omega^2 + \alpha^2\pi^4(2n+1)^4} e^{-\alpha\frac{(2n+1)^2\pi^2 t}{4l^2}} \cos\frac{(2n+1)\pi x}{2l} \tag{11}$$

where

$$\beta = \left(\frac{\omega}{2\alpha} \right)^{\frac{1}{2}} \tag{12}$$

$$A = \frac{\cosh \beta x (1+i)}{\cosh \beta l (1+i)} = \left(\frac{\cosh 2\beta x + \cos 2\beta x}{\cosh 2\beta l + \cos 2\beta l} \right)^{\frac{1}{2}} \tag{13}$$

and

$$\begin{aligned} \phi &= \arg \left[\frac{\cosh \beta x (1+i)}{\cosh \beta l (1+i)} \right] \\ &= \tan^{-1} \left[\frac{\sinh(\beta x) \sin(\beta x)}{\cosh(\beta x) \cos(\beta x)} \right]^{\frac{1}{2}} - \tan^{-1} \left[\frac{\sinh(\beta l) \sin(\beta l)}{\cosh(\beta l) \cos(\beta l)} \right]^{\frac{1}{2}} \end{aligned} \tag{14}$$

The first term on the right side of Eq. 11 is the steady-state part of the solution, and the second term is the transient part, which becomes negligible as *t* becomes sufficiently large. The term *A* is the amplitude of the steady-state temperature variation at position *x*, and ϕ is the phase shift in the variation. Values of *A* and ϕ as a function of βl and *x/l* are given in graphical form by Carslaw and Jaeger.[B5]

Because the characteristic thermal diffusion time $t_\alpha = l^2/\alpha$ is on the order of 5×10^{-5} days or less, the exponential terms in the transient part of the solution are essentially zero except for very small values of time (t << 1day). Furthermore, the value of *l* is on the order of 0.2 cm^{-1} or less, and the dimensionless terms βl and βx are on the order of 0.02 or less, in which case $A \approx 1$, and $\phi \approx 0$. Therefore, the temperature variations everywhere in the molding compound are essentially equal to the variations in the ambient temperature.

B2. Mass Transfer of Moisture

Consider moisture transport through a molding compound that is in intimate contact with the die (no flaws exist between the molding compound and the die). Assume that diffusion of water through the molding material can be described by Fick's law with a temperature-dependent diffusion coefficient $D(T)$. Let *C* denote the molar water concentration in the molding compound having thickness 2*l*. The material balance for water in the molding compound is given by

$$\frac{\partial C}{\partial t} = D\left[T(t) \right] \frac{\partial^2 C}{\partial x^2} \tag{15}$$

In the case of moisture transport, let $x = 0$ denote the interface between the die and the molding material, and let $x = 2l = l'$ denote the interface between the molding compound and the ambient atmosphere having relative humidity H_{amb}. The ambient relative

humidity and the water concentration $C(l',t)$ at the surface of the molding compound are related by the expression

$$C(l',t) = H_{amb} P_{sat}(T) S(T) \tag{16}$$

where P_{sat} is the saturation vapor pressure of water in air at temperature T, and S is the sorption distribution coefficient for water in equilibrium with the ambient air and the molding compound at temperature *T*. Expressions for $D(T)$, $P_{sat}(T)$, and $S(T)$ were obtained from work by Shirley[B1],

$$D(T) = D_0 e^{-\frac{Q_D}{RT}} \tag{17}$$

where D_0 = 0.47 cm^2/s, Q_D= 11,500 cal/mole, and R = 1.99 cal/mole K;

$$P_{sat}(T) = P_0 e^{-\frac{Q_V}{RT}} \tag{18}$$

where P_0 = 4.7x10^5 atm, and Q_V = 9700 cal/mole, and

$$S(T) = S_0 e^{-\frac{Q_S}{RT}} \tag{19}$$

where S_0 = 2.8x10^{-9} mole/atm cm^3, and Q_S = 9200 cal/mole. Values for $D(T)$ calculated from Eq. 17 are given in the Table B-2 below for selected temperatures in the range of interest.

Table B-2. Calculated Values of Diffusion Coefficient

Temperature (^oC)	*Temperature* (^oK)	$D(T)$ x10^9 (cm^2/s)	$D(T)$ x10^4 (cm^2/day)
-40	233	0.0080	0.0069
-30	243	0.022	0.019
-20	253	0.057	0.049
-10	263	0.13	0.11
0	273	0.30	0.26
10	283	0.64	0.55
20	293	1.3	1.1
30	303	2.4	2.1
40	313	4.5	3.9

Let the ambient relative humidity vary periodically such that the water concentration $C(l',t)$ at the surface of the molding compound varies sinusoidally with time *t*. Denote the maximum concentration by C_{max} and the minimum concentration by C_{min}. Let

$$C(l',t) = C_{ave} + \tilde{C} \tag{20}$$

where $\tilde{C}$ is the sinusoidal variation in the water concentration about the average concentration C_{ave}. Let

$$\tilde{C} = \tilde{C}_{\max} \sin\left(\omega t + \varepsilon\right) \tag{21}$$

where

$$\tilde{C}_{max} = C_{max} - C_{ave} = C_{ave} - C_{min} \tag{22}$$

$$C_{ave} = \frac{C_{max} + C_{min}}{2} \tag{23}$$

$$\omega = \frac{2\pi}{t_c} \tag{24}$$

and t_c is the time for one sinusoidal cycle.
For an impermeable interface at $x = 0$

$$\frac{\partial C\left(0,t\right)}{\partial x} = 0 \tag{25}$$

and for the purpose of examining the effects of periodic variations in the water concentration at $x = l'$ that are caused by periodic variations in the ambient relative humidity, let the initial water concentration in the sheet of molding compound be uniform and equal to C_{ave}

$$C\left(x,o\right) = C_{ave} \tag{26}$$

Again the cycle times of interest are daily and yearly. However, unlike heat transfer, the characteristic diffusion time

$$t_D = \frac{l'^2}{D} \tag{27}$$

for water transport is very large (varying from ~20 to ~10^4 days as the temperature varies from 40 to –40^o C) relative to a cycle time of 1 day. Furthermore, t_D is on the order of a yearly cycle time of 365 days. Also, the diffusion coefficient varies during each cycle as the temperature varies sinusoidally with time.

Let

$$\tau = \int_0^t D\left[T\left(t'\right)\right] dt' \tag{28}$$

Then the preceding diffusion equation can be transformed to

$$\frac{\partial C}{\partial \tau} = \frac{\partial^2 C}{\partial x^2} \tag{29}$$

Now, let $t = nt_c + \tilde{t}$, where $0 < \tilde{t} < t_c$, and n denotes an integer number of cycles. Then

$$\begin{aligned} \tau &= \int_0^{nt_c + \tilde{t}_c} D\left[T\left(t'\right)\right] dt' \\ &= \int_0^{nt_c} D\left[T\left(t'\right)\right] dt' + \int_{nt_c}^{nt_c + \tilde{t}_c} D\left[T\left(t'\right)\right] dt' = n\int_0^{t_c} D\left[T\left(t'\right)\right] dt' + \int_0^{\tilde{t}_c} D\left[T\left(t'\right)\right] dt' \end{aligned} \tag{30}$$

because

$$\int_0^{t_c} D\left[T(t')\right]\,dt' = \int_{t_c}^{2t_c} D\left[T(t')\right]\,dt' = \int_{2t_c}^{3t_c} D\left[T(t')\right]\,dt' = \cdots\cdots \tag{31}$$

Let

$$D_{ave} = \frac{\int_0^{t_c} D\left[T(t')\right]dt'}{t_c} \tag{32}$$

Then, τ can be written as

$$\tau = D_{ave}(nt_c) + \int_0^{\tilde{t}_c} D\left[T(t')\right]\,dt' \tag{33}$$

and as the number of cycles *n* increases, $nt_c \to t$, and

$$\tau \to D_{ave}t \tag{34}$$

Let $C(x,\tau)$ denote the solution to Eq. 29 for a constant concentration at $x = l'$, zero flux at $x = 0$, and uniform initial condition. Then, after several cycles

$$C(x,\tau) \to C(x, D_{ave}t) \tag{35}$$

where $C(x, D_{ave}t)$ is the solution that would be obtained for

$$\frac{\partial C}{\partial t} = D_{ave}\frac{\partial^2 C}{\partial x^2} \tag{36}$$

with the same boundary and initial conditions. Using Duhamel's theorem,[B5] the solution to Eq. 36 for the boundary and initial conditions given by Eqs. 20, 25, and 26 is obtained from $C(x, D_{ave}t)$. The result is given by Eqs. 11 – 14, in which $\tilde{T}/\tilde{T}_{max}$, l, α, and β are replaced by $\tilde{C}/\tilde{C}_{max}$, l', D_{ave}, and β', respectively, where

$$\beta' = \left(\frac{\omega}{2D_{ave}}\right)^{\frac{1}{2}} \tag{37}$$

Now consider daily variations in the ambient relative humidity that result in daily sinusoidal variations in $C(l',t)$. Equation 11 can be written as

$$\begin{aligned}\frac{\tilde{C}}{\tilde{C}_{max}} &= A\sin(\omega t + \varepsilon + \phi) \\ &+ \sum_0^{\infty} \frac{(-1)^n}{(\pi/4)(2n+1)}\left[\frac{\omega\cos\varepsilon - \gamma_n\sin\varepsilon}{\omega^2 + \gamma_n^{\,2}}\ \gamma_n e^{-\gamma_n t}\cos\frac{(2n+1)\pi x}{2l}\right.\end{aligned} \tag{38}$$

where

$$\gamma_n = \frac{D_{ave}(2n+1)^2\pi^2}{4l^2} \tag{39}$$

In Eq. 38, the terms in the summation expression are dominated by the term $\gamma_n e^{-\gamma_n t}$. For D_{ave} on the order of $1\text{x}10^{-4}$ cm^2/day and *l* on the order of 0.1cm, γ_n is on the order of $0.02(2n+1)^2$. The first term, corresponding to *n* = 0, in the alternating summation is on

the order of γ_n = 0.003, or less, because t_c = 1 day and ω = 2π day^{-1}. For *t* on the order of 5t_c, or greater, the term $e^{-\gamma_n t}$ will decrease much more rapidly as *n* increases than γ_n will increase. The terms in the sum will be small and will alternate in sign, so that the value of the sum will be on the order of the value for first term, and after several cycles will contribute little to the right side of Eq. 38. Therefore,

$$\frac{\tilde{C}}{\tilde{C}_{max}} \approx A\sin\left(\omega t + \varepsilon + \phi\right) \tag{40}$$

The value of $\beta' l'$ is on the order of 18. The amplitude *A* of the steady-state portion of the solution is obtained from Eq. 13 by substituting $\beta' l'$ for βl. At $x = l'$, the amplitude $A = 1$, and the phase angle $\phi = 0$. However, at $x = 0$, the amplitude $A \approx 0$, although the phase angle ϕ is nonzero. The net effect at the surface of the die is as follows. Because the characteristic diffusion time

$$t_D = \frac{l'^2}{D_{ave}} \tag{41}$$

is large relative to the cycle time, the periodic variations that occur at the surface of the molding compound dampen out before they reach the surface of the die. The response at the interface with the die corresponds to that produced by the average of the daily periodic variations in the water concentration at the surface of the molding compound.

Now, consider a yearly sinusoidal variation in the average value of the daily variation in $C\left(l', t\right)$. In this case, t_c = 365 day, and ω = (2π/365) day^{-1}. Again, for D_{ave} on the order of 1x10^{-4} cm^2/day, and *l* on the order of 0.1cm, γ_n is on the order of 0.02(2*n*+1)^2. For *t* on the order of 5t_c or greater, the terms involving $\gamma_n e^{-\gamma_n t}$ will be negligible, and the yearly variation in water concentration is again given by the steady-state portion of the solution (Eq. 40). However, for a yearly cycle, $\beta' l'$ is on the order of 0.9. Again, at $x = l'$, the amplitude $A = 1$, and the phase angle $\phi = 0$. But at $x = 0$, the amplitude $A \approx 0.84$, and the phase angle $\phi \approx$ -0.76 radians or –44 degrees. The net effect at the interface with the die is as follows. Because the characteristic diffusion time t_D is now similar in magnitude to the yearly cycle time, the periodic variations that occur at the surface of the molding compound cause periodic variations in the water concentration at the interface with the die. The amplitude of the variation and the phase shift will depend on the thickness of the molding compound, temperature history and corresponding average diffusion coefficient.

The relative humidity H_{die} at the interface with the die is given by

$$H_{die} = \frac{C\left(0, t\right)}{P_{sat}\left(T\right)S\left(T\right)} \tag{42}$$

and depends on the properties of the molding compound and the temperature-humidity conditions of interest. The value of D_{ave} will vary substantially with the temperature history, and the parameter values given by Eqs. 17 and 19 involve nontrivial uncertainty.

Therefore, values of the amplitude A on the order of unity, and phase shifts ϕ between 0 and 2π radians are reasonable for some scenarios. The number of possible scenarios is large. Therefore, only some limiting cases are considered briefly to illustrate the range of the effects that can result from a phase shift ϕ in the periodic variation in water concentration.

First, consider the case in which the yearly variations in ambient temperature and humidity are in phase; the maximum temperature and maximum humidity occur at the same time. At the interface with the die, let the amplitude A = 1. If the phase shift $\phi = 0$ or $\pm 2m\pi$ radians, where m is an integer, then the temperature and relative humidity variations occurring at the interface with the die are also in phase and are the same as those occurring at the surface of the molding compound. The maximum temperature and maximum humidity occur at the same time. However, if the phase shift $\phi = (2m-1)\pi$, where m is an integer, then the temperature and relative humidity variations occurring at the interface with the die are an odd multiple of π radians out of phase with those occurring at the surface of the molding compound. The minimum humidity will occur at the maximum temperature, and conversely, which is exactly opposite to the conditions at the surface of the molding compound.

Next, consider the case in which the yearly variations in ambient temperature and humidity are out of phase; the minimum humidity occurs at the maximum temperature, and conversely. Again, at the interface with the die, let the amplitude A = 1. If the phase shift $\phi = 0$ or $\pm 2m\pi$ radians, then the temperature and relative humidity variations occurring at the interface with the die are also out of phase and are the same as those occurring at the surface of the molding compound. The minimum humidity and maximum temperature occur at the same time. However, if the phase shift $\phi = (2m-1)\pi$, then the temperature and relative humidity variations occurring at the interface with the die are a odd multiple of π radians out of phase with those occurring at the surface of the molding compound. The maximum humidity will occur at the maximum temperature, and conversely, which is exactly opposite to the conditions at the surface of the molding compound. This situation could be of concern if the maximum humidity was on the order of the critical humidity, which would then occur at the die at higher temperatures than at the surface of the molding compound.

Now consider daily variations about the yearly response at the die. Over a period of a few daily cycles, the water concentration $C(0,t)$ at the interface with the die will change very little. However, the temperature may vary by 10 to 20^{o} C. In principal, the relative humidity H_{die} corresponding to $C(0,t)$ should vary with the temperature, as indicated by Eq. 42. However, the increase in H_{die} that would result from a decrease in P_{sat} due to a decrease in temperature from T_{max} to T_{min} is almost exactly compensated for by an opposite change in the sorption coefficient S, which increases as the temperature decreases. In particular,

$$\frac{H_{die}(T_{max})}{H_{die}(T_{min})} = \frac{\dfrac{C(0,t)}{P_{sat}(T_{max})S(T_{max})}}{\dfrac{C(0,t)}{P_{sat}(T_{min})S(T_{min})}} = e^{-\frac{500}{RT}\left(\frac{1}{T_{max}}-\frac{1}{T_{min}}\right)} \approx 1 \qquad (43)$$

because the term $\left(\frac{1}{T_{max}}-\frac{1}{T_{min}}\right.$ is on the order of $3\text{x}10^{-4}$ K^{-1} for temperatures of interest.

Finally, if a flaw exists between the molding compound and the die, water vapor in equilibrium with $C(0,t)$ could accumulate in the flaw. As the temperature changes, the relative humidity in the flaw could change. However, unless the characteristic thickness of the flaw is a significant fraction of the thickness of the molding compound, the relaxation time for diffusion of excess water vapor into the molding compound will be small relative to a daily cycle time.[B6] Any increase in H_{die} that would result from an decrease in P_{sat} due to a decrease in temperature again will be rapidly compensated for by an opposite change in the sorption coefficient S.

References – Appendix B

B1. C. G. Shirley, "THB Reliability Models and Life Prediction for Intermittently-Powered Non-Hermetic Components," IEEE/IRPS, 1994, pp. 72-78

B2. C. G. Shirley and C. Hong, "Optimal Acceleration of Cyclic THB Tests for Plastic-Packaged Devices," in Proc. 29th Ann. Int'l Reliability Physics Symposium, pp.12-21 (1991).

B3. Y. S. Touloukian, ed., Thermophysical Properties of High Temperature Solid Materials, vol. 4, The Macmillian Company, New York, 1967, pp. 353-360.

B4. Y. S. Touloukian, ed., Thermophysical Properties of High Temperature Solid Materials, vol. 6, The Macmillian Company, New York, 1967, pp. 1082 and 1220.

B5. H. S. Carslaw and J. C. Jaeger, Conduction of Heat in Solids, 2nd ed., Clarendon Press, Oxford, 1959, pp. 102-107.

B6. J. Crank, The Mathematics of Diffusion, 2nd ed., Clarendon Press, Oxford, 1975, pp. 56 – 60.

APPENDIX C: CRAX/CASSANDRA Reliability Analysis Software

This appendix provides some reference information on the Sandia-developed software package that was used to include uncertainty in the bondpad corrosion model. This package also served as the integrator (CRAX) between the deterministic equation described in Section 3.1 and the uncertainty analysis engine (CASSANDRA). The sections specifically address the motivation and objectives for its development, its computational elements, and its application to real problems. Of note, although this software was not developed as part of this project, it forms the computational core of the integrated corrosion model.

C1. Background

Over the past few years, Sandia National Laboratories has been moving toward an increased dependence on model- or physics-based analyses as a means to assess the impact of long-term storage on the nuclear weapons stockpile. These deterministic models have also been used to evaluate replacements for aging systems, often involving commercial off-the-shelf (COTS) components. In addition, the models have been used to assess the performance of replacement components manufactured via unique, small-lot production runs. In either case, the limited amount of available test data dictates that the only logical course of action to characterize the reliability of these components is to specifically consider the uncertainties in material properties, operating environment, etc. within the physics-based (deterministic) model. This not only provides the ability to statistically characterize the expected performance of the component or system, but also provides direction regarding the benefits of additional testing on specific components within the system.

Traditional reliability methods depend on the collection of a large number of samples or observations to characterize the existing condition of the weapons stockpile. These tests provide a snapshot of the existing reliability characteristics of the system. A major objective of recent research is to develop mathematical techniques and computer analysis tools to anticipate stockpile problems before they become critical issues. For example (see Figure C1), based on average properties, one might predict that failure would occur later in life than the point at which unacceptable risk is reached.

The assessment of new materials and manufacturing techniques has, in the past, depended on ‘average’ characterization using deterministic modeling tools. Recent research, however, has focused on developing mathematical methods for incorporating uncertainty in traditional deterministic modeling, in particular, the advanced phenomenological modeling and simulation techniques used to characterize the physics of the underlying failure processes (such as that described in the body of this report).

Of particular concern was the development of an analysis capability that would be applicable over the entire life cycle of the system. An essential element was the ability to incorporate both test data and engineering judgement into the reliability characterization of the material or component being evaluated. Finally, it was important that the method address the sensitivity of the system performance to the uncertainties in the various internal and external model parameters.

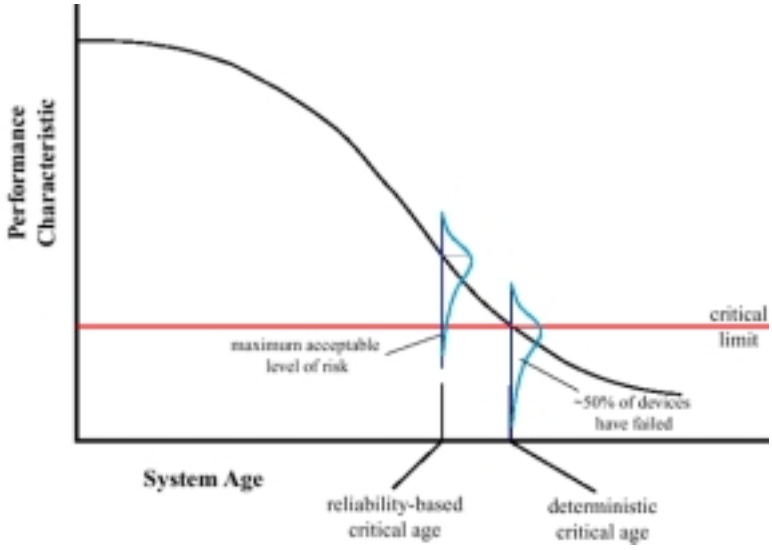

Figure C1. Reliability-based vs. deterministic performance analysis

An effort was therefore undertaken to evaluate the capabilities of existing probabilistic methods and, if required, to develop new analysis methods to support the inclusion of uncertainty in the classical design tools used by analysts and design engineers at Sandia. The primary result of this effort is the CRAX (Cassandra Exoskeleton) reliability analysis software.

C2. Software Elements

There are three major elements to CRAX: 1) the uncertainty analysis engine – Cassandra, 2) the user interface – also called CRAX, and 3) the physical model. The relationship between these three elements is depicted in Figure C2.

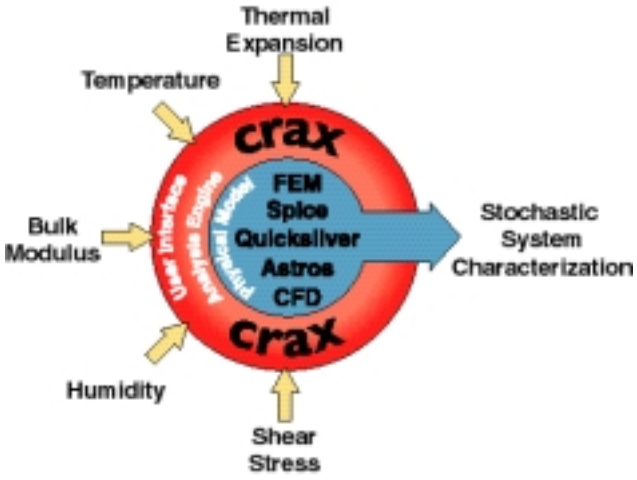

Figure C2. Diagram showing the relationship between software elements

The heart of the CRAX software is the Cassandra uncertainty analysis engine. This engine consists of a number of software routines that permit the user to select a variety of methods for including uncertainty in their analyses. A number of first and second order techniques, max-likelihood and a variety of other analytical methods are available for application. In addition, there are options for using a number of pseudo- and quasi-Monte Carlo methods. Specific methods are constantly being updated and improved. One of the more recent additions is the option to use quasi-Monte Carlo sampling methods rather than traditional pseudo-Monte Carlo techniques. The end part of Section C4 below contains a specific example of the application of these techniques. Importantly, Cassandra is written completely in C/C++ making the engine very portable.

CRAX/Cassandra has been used with Win95, WinNT, Power Macintosh, Sun, Silicon Graphics and DEC operating systems. In addition, the software has been ported to one of the large tera-flop computers at Sandia.

Access to the Cassandra uncertainty analysis engine is gained via the CRAX interface. The CRAX graphical user interface (GUI) is based entirely on the Tool Command Language (Tcl) and associated Tool Kit (Tk). The use of Tcl and Tk permits the software to be hosted on any platform and provides a great deal of flexibility in accessing the Cassandra uncertainty engine. Rather than trying to develop a complicated GUI for the user that could handle any situation, the use of Tcl/Tk permits the very quick construction of unique interfaces specific to the problem being analyzed (a basic/generic interface is available for simple analyses).

The last element in the CRAX family is the physical model. It was decided early in the development of CRAX to not include any physical modeling tools directly in the software. Rather than develop a modeling tool (e.g. a finite element bondpad corrosion package) unique to CRAX, it was decided to let the engineer rely on the existing and emerging tools that they were comfortable with and had confidence in. While not the ideal situation in terms of analysis speed, it was felt that for the engineers to become comfortable with incorporating uncertainty into their deterministic models, it was critical

to not stretch their belief system too far. The CRAX GUI effectively ‘wraps Cassandra around’ the existing analysis software; hence the reference to CRAX as an exoskeleton.

C3. Software Accessibility

The exchange of information between the CRAX GUI, Cassandra, and the physical model can take many forms. Within CRAX is the capability to either recompile the existing software into the Cassandra engine, thereby significantly increasing computational efficiency, or rely on 'hand-shaking' between the CRAX GUI, the Cassandra engine and the existing software (the former approach was adopted in the corrosion work described in Section 4). The Tcl/Tk interface can be modified to handle either of these situations very easily. In addition, Cassandra is platform independent and complies with the Common Object Request Broker Architecture (CORBA) permitting easy interface with many of the new engineering design and analysis software packages (Figure C3). A large number of the commercial software vendors have adopted the CORBA interface standards, e.g. Hewlett-Packard.

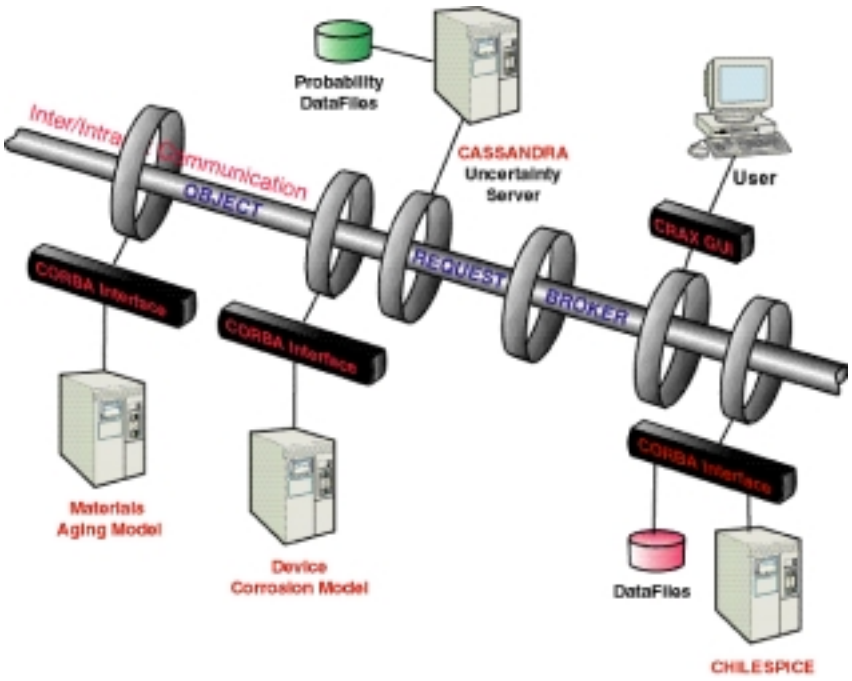

Figure C3. Diagram depicting the network accessibility of the Cassandra uncertainty engine

C4. Chilespice Electrical System Model and Interface with CRAX

As noted in Section 4.1, the ChileSPICE software program being developed at Sandia was used to assess the effect of corrosion on a voltage comparator device. This section includes some background information on this code. Its base is a code named SPICE that is a general-purpose circuit simulation program for nonlinear dc, nonlinear

transient, and linear ac analyses. Circuits may contain resistors, capacitors, inductors, mutual inductors, independent voltage and current sources, four types of dependent sources, lossless and lossy transmission lines (two separate implementations), switches, uniform distributed RC lines, and the five most common semiconductor devices: diodes, BJTs, JFETs, MESFETs, and MOSFETs. Version 1.0 of ChileSPICE is the initial release of parallel-circuit simulation software from Sandia National Laboratory. The code is based on the UC Berkeley version Spice3f5. Some major enhancements have been included in ChileSPICE including:

- Parallel circuit load
- Parallel Aztec iterative solver
- Restart capability
- Extensive numerical diagnostics

These capabilities are accessed through a combination of compile time options (for parallel load & solve) and new commands (for restart and diagnostics).

The ChileSPICE program and the CRAX/Cassandra uncertainty analysis software were easily linked (see Figure C3) to permit the age-aware system analysis described in Section 4.1 to be accomplished. A number of uncertainty analysis techniques were investigated to determine which one yielded the most computationally efficient solutions. Latin Hypercube sampling (LHS), quasi-Monte Carlo (qMC), advanced mean value with fast probability integration (AMV/FPI), and a new method referred to as the Field Analysis Method (FAM). Figure C4 depicts the number of function evaluations required to achieve acceptable results for each of these methods. For this particular problem, the new Field Analysis Method worked extremely well.

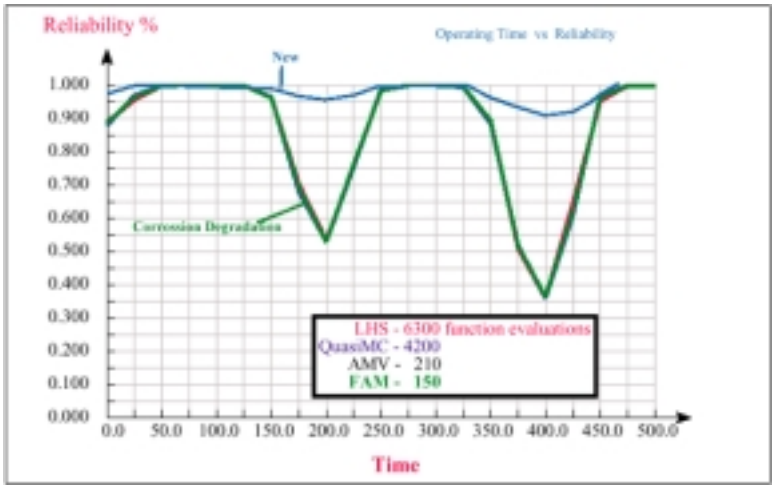

Figure C4. Comparison of results from a number of uncertainty analysis techniques contained within the CRAX/Cassandra software package. The application is the real-time operation of the voltage comparator circuit shown in Figure 4-3. Time is in milliseconds.

C5. Status

The CRAX/Cassandra reliability analysis software is constantly being updated as additional existing reliability analysis methods are incorporated into Cassandra and new analysis techniques are developed. For example, CRAX is currently being integrated with a major finite-element continuum code at Sandia (GOMA) that will permit more robust analyses of the effects of corrosion on electrical devices to be performed. Each new design problem brings with it a unique set of input, output and computational requirements. The flexibility of the CRAX interface and the extensibility of the Cassandra uncertainty engine permits the reliability issues to be addressed quickly and efficiently whatever the computational requirements might be. The software continues to provide new insights into issues related to high-consequence systems that were not possible before.

DISTRIBUTION

Analytical Solutions Inc.
Attn: Michael P. Strizich (3)
10401 Research SE
Albuquerque, NM 87123

Sandia:

1	MS 1415	J. C. Barbour, 1112
1	MS 0525	P. V. Plunkett, 1734
1	MS 1738	D. W. Peterson, 1738
1	MS 1081	J. M. Soden, 1739
1	MS 1745	J. N. Sweet, 1745
1	MS 1081	F. W. Sexton, 1762
1	MS 0886	R. P. Goehner, 1822
1	MS 0886	B. McKenzie, 1822
2	MS 0886	J. R. Michael, 1822
15	MS 0888	N. R. Sorensen, 1832
10	MS 0888	J. W. Braithwaite, 1832
2	***MS 0888***	***S. J. Lucero, 1832***
1	MS 1411	S. M. Foiles, 1834
1	MS 1411	C. C. Battaile, 1834
1	MS 0501	J. R. Fellerhoff, 2330
1	MS 6413	D. G. Robinson, 6413
1	MS 0834	K. L. Erickson, 9112
1	MS 0834	J. E. Johannes, 9114
1	MS9018	Central Technical Files, 8945-1
2	MS0899	Technical Library, 9616
2	MS0612	Review and Approval Desk, 9612 for DOE/OSTI